Remote sensing data as a tool to monitor and mitigate natural catastrophes resulting from anthropogenic activities: Case studies over land and water

Dissertation der Fakultät für Biologie

der Ludwig-Maximilian-Universität München

vorgelegt von

Elizabeth C. Atwood,

M.Sc. Quantitative Ecology & Resource Management

München, 6. März 2018

EIDESSTATTLICHE VERSICHERUNG UND ERKLÄRUNG

Ich versichere hiermit an Eides statt, dass meine Dissertation selbständig und ohne unerlaubte Hilfsmittel angefertigt worden ist.

Die vorliegende Dissertation wurde weder ganz, noch teilweise bei einer anderen Prüfungskommission vorgelegt.

Ich habe noch zu keinem früheren Zeitpunkt versucht, eine Dissertation einzureichen oder an einer Doktorprüfung teilzunehmen.

München, den 2. November 2018   …………………………………...

(Elizabeth C. Atwood)

ACKNOWLEDGEMENTS

ABSTRACT

This thesis demonstrates how remotely sensed satellite acquisitions can be used to addresses some of the natural catastrophes resulting from anthropogenic activities. Examples from both land and water systems are used to illustrate the breath of this toolbox. The effects of global climate change on biological systems and the wellbeing of everyday people are becoming less easy to ignore. In addition, our oceans are facing multiple large-scale stressors, including microplastics as a recently recognized threat, which place at risk the resources which a large percentage of the world's population depends on for their livelihood. The cause of many of these changes stem from anthropogenic activities, but lacking understanding of complex ecosystems limits our ability to make definite conclusions as to cause and effect. The difficulty to collect on-the-ground data sufficient enough to capture processes working over scales of hundred of kilometers up to the entire globe is often a limitation to research. Remote sensing systems help ameliorate this issue through providing tools to better monitor environmental changes over large areas. The examples provided in this thesis focus on (Section I) tropical peatland fire characteristics and burning in Southeast Asia as a significant contributor to greenhouse gas emissions and (Section II) spread of river-based plastic pollution in coastal ocean systems.

Section I specifically focuses on fires within Indonesia, which holds more than half of all known peatlands in the tropical zone and are estimated to represent a carbon pool of 82–92 gigatons. A brief description of recent development activities within Indonesia is presented in Section I of the Introduction, followed by meteorological processes responsible for extended drought periods in the region, and the situation of current fire control within the country. Chapter 1 presents an example of the large improvement in fire detection, as well as measurement of fire front characteristics, provided by a state-of-the-art thermal remote sensing. Chapter 2 goes into detail describing how an active satellite sensor system is able to provide much quicker and more accurate estimates of burned area for the tropics than other existing methods dependent on passive satellite sensor systems. Both these methods provide powerful tools for development of an improved system to monitor fire over Indonesia. The goal of such a monitoring system would be to reduce fire emissions from this large country, which according to global climate models play an important role in global climate change.

Section II focuses on aquatic plastic pollution flowing from a freshwater system into the coastal oceans. A background of the issue of plastic pollution along with the current status of plastic debris in both oceans and inland river systems is presented in Section II of the Introduction. Chapter 3 describes development and comparison of two different modelling efforts to display how plastic particles being emitted from a major river are accumulating along the nearby coastline. The goal of this work is to present how remote sensing data could be used to in conjunction with ocean current modelling to create a comprehensive particle tracking monitoring system.

ZUSAMMENFASSUNG

Diese Arbeit zeigt, wie aus der Ferne wahrgenommene Satellitenaufnahmen dazu verwendet werden können, sich einigen Naturkatastrophen, die aus anthropogenen Aktivitäten resultieren, zu widmen. Anhand von Beispielen aus Land- und Wassersystemen wird der Umfang dieses technischen Werkzeugkastens dargestellt. Die Auswirkungen des globalen Klimawandels auf biologische Systeme und das Wohlbefinden des Menschen lassen sich nicht mehr ignorieren. Darüber hinaus sind unsere Ozeane mehreren großen Stressfaktoren ausgesetzt, einschließlich Mikroplastik als eine seit kurzem anerkennte Bedrohung, welche die Ressourcen gefährden, von denen der Lebensunterhalt eines großen Teils der Weltbevölkerung abhängt. Die Ursache vieler dieser Veränderungen liegt in anthropogenen Aktivitäten, aber mangelndes Verständnis für komplexe Ökosysteme begrenzt unsere Fähigkeit, eindeutige Rückschlüsse auf Ursache und Wirkung zu treffen. Die Schwierigkeit, Daten vor Ort zu sammeln, die ausreichen, um Prozesse zu erfassen, die über Hunderte von Kilometern bis hin zum gesamten Globus arbeiten, ist oft eine Einschränkung der Forschung. Fernerkundungssysteme tragen dazu bei, dieses Problem zu beheben, indem sie Werkzeuge zur besseren Überwachung von Umweltveränderungen in großen Gebieten bereitstellen. Die Beispiele in dieser Arbeit konzentrieren sich auf („Section I") Feuermerkmale und Brandflächen der tropischen Torfgebiete in Südostasien als signifikanter Beitrag zu Treibhausgasemissionen und („Section II") Ausbreitung von Fluss-basiertem Plastikmüll in küstennahen Meeressystemen.

Section I konzentriert sich speziell auf die Brände in Indonesien, welches mehr als die Hälfte aller bekannten Torfgebiete in der tropischen Zone besitzt und auf einen Kohlenstoffpool von 82-92 Gigatonnen geschätzt wird. Eine kurze Beschreibung der jüngsten Entwicklungstätigkeiten in Indonesien wird in Section I der Einleitung vorgestellt, gefolgt von meteorologischen Prozessen, die für ausgedehnte Dürreperioden in der Region verantwortlich sind, und der Situation der aktuellen Feuerkontrolle innerhalb des Landes. Chapter 1 zeigt ein Beispiel für die große Verbesserung der Branddetektion sowie die Messung der Brandfronteigenschaften, die durch eine moderne thermische Fernerkundung erreicht werden können. In Chapter 2 wird ausführlich beschrieben, wie ein aktives Satellitensensorsystem in der Lage ist, schnellere und genauere Schätzungen der verbrannten Fläche für die Tropen zu liefern als andere existierende Methoden, die von passiven Satellitensensorsystemen abhängen. Beide Methoden bieten leistungsstarke Werkzeuge für die Entwicklung eines verbesserten Systems zur Brandüberwachung von Indonesien. Ziel eines solchen Überwachungssystems wäre es, Brandemissionen aus diesem großen Land zu reduzieren, das nach globalen Klimamodellen eine wichtige Rolle im globalen Klimawandel spielt.

Section II konzentriert sich auf die Verschmutzung von Wasserplastik, die von einem Süßwassersystem in die Küstenmeere fließt. Ein Hintergrund des Problems der Plastikverschmutzung zusammen mit dem gegenwärtigen Status von Plastiktrümmern sowohl in Ozeanen als auch Binnenflusssystemen wird in Section II der Einleitung dargestellt. Chapter 3 beschreibt die Entwicklung und den Vergleich von zwei verschiedenen Modellierungsbemühungen, um zu zeigen, wie sich Kunststoffpartikel, die von einem großen Fluss emittiert werden, entlang der nahen Küstenlinie ansammeln. Das Ziel dieser Arbeit ist zu zeigen, wie Fernerkundungsdaten in Verbindung mit Meeresströmungsmodellierung verwendet werden können, um ein umfassendes Teilchenverfolgungsüberwachungssystem zu schaffen.

iv

LIST OF ORIGINAL ARTICLES

Section I: Fire, peat and forest biomass

CHAPTER 1
Atwood EC, Englhart S, Lorenz E, Halle W, Wiedemann W, Siegert F. (2016) Detection and characterization of low temperature peat fires during the 2015 fire catastrophe in Indonesia using a new high-sensitivity fire monitoring satellite sensor (FireBird). *PLOS ONE* 11(8): e0159410.

CHAPTER 2
Lohberger S, Stängel M, **Atwood EC**, Siegert F. (2017) Spatial evaluation of Indonesia's 2015 fire-affected area and estimated carbon emissions using Sentinel-1. *Global Change Biology* 24(2): 644–654.

Section II: Plastic in waterways and the oceans

CHAPTER 3
Atwood EC, Falcieri FM, Piehl S, Bochow M, Matthies M, Franke J, Carniel S, Sclavo M, Laforsch C, Sieger F. (in progress) Coastal accumulation of microplastic particles emitted from the Po River, Northern Italy: Comparing remote sensing and ocean current modelling with *in situ* sample collections. *Marine Pollution Bulletin*.

CONTRIBUTION OF THE AUTHORS

CHAPTER 1

Elizabeth C. Atwood planned the study, developed the methodology for image processing and fire characteristic measurements, completed the processing steps and wrote the paper. Dr. Sandra Lohberger (née Englhart) helped in study planning and analysis of the data, contributed tools for data processing and aided in writing the paper. Dr. Eckehard Lorenz and Dr. Winfried Halle organized the acquisition of TET-1 and provided technical support in image processing. Werner Wiedemann contributed to study planning and development of the image processing methodology. Prof. Dr. Florian Siegert contributed to the conception and design of the study, and revised the manuscript.

CHAPTER 2

Dr. Sandra Lohberger planned the study, collaborated in the development of the image processing methodology, and aided in writing the paper. Mathias Stängel played a central role in development and execution of the SAR-image processing methodology, and provided input for writing the manuscript. Elizabeth C. Atwood aided in planning of the study as well as interpretation of the SAR-image results, and wrote the manuscript. Prof. Dr. Florian Siegert helped conceive of the study and provided revisions to the manuscript.

CHAPTER 3

Elizabeth C. Atwood, Sarah Piehl and Mathias Bochow helped design the study and conduct the field sampling. Elizabeth C. Atwood developed the near-range spectral measurement cal/val methodology, completed the processing of the satellite image time series and wrote the paper. Dr. Fracesco M. Falcieri was responsible for the hydrodynamic and Lagrangian modelling as well as interpretation of the results. Sarah Piehl completed the water and sediment microplastic sample processing and particle identification. Dr. Mathias Bochow developed and completed the SWIR microplastic particle identification. Prof. Dr. Michael Matthies helped in study design and development of the hydrodynamic model. Dr. Jonas Franke is responsible for conception of the study, as well as help in study design and provided revisions of the manuscript. Dr. Sandro Carniel and Dr. Mauro Sclavo both organized development of the hydrodynamic model, Dr. Sandro Carniel also provided revisions of the manuscript. Prof. Dr. Christian Laforsch and Prof. Dr. Florian Siegert conceived of the project, provided input to study design, helped with interpretation of the results and provided revisions to the manuscript.

I hereby confirm the above statements.

Munich, November 2, 2018

………………………………   …………………………………
Elizabeth C. Atwood   Prof. Dr. Florian Siegert

LIST OF ACRONYMS

A	small-plot agriculture
ABS	acrylonitrile butadiene styrene
AGB	aboveground biomass
AOI	area of interest
Arpae-ER	Emilia Romagna Regional Agency for Prevention, Environment and Energy (Italian: "Agenzia regionale per la prevenzione, l´ambiente e l´energia – Emilia-Romagna")
ASEAN	Association of Southeast Asian Nations
ATR FT-IR	Attenuated Total Reflectance FT-IR spectroscopy
BIRD	Bi-spectral Infrared Remote Detection
BIROS	Berlin InfraRed Optical System
BPA	bisphenol A
C	carbon
C/U	composite particles or unknown plastic types
cDOM	colored dissolved organic matter (also Gelbstoff or gilvin)
CH_4	methane
Chl-A	chlorophyll-A
CNR-ISMAR	National Research Council (Italian: "Consiglio Nazionale delle Ricerche") – Istituto di Scienze Marine
CO	carbon monoxide
CO_2	carbon dioxide
CO2-eq	carbon dioxide equivalents
COAWST	Coupled-Ocean-Atmosphere-Wave-Sediment Transport model
DLR	German Aerospace Center (German: "Deutsches Zentrum für Luft- und Raumfahrt")
DW kg	dry weight kilogram
E_{down}	downwelling irradiance
ENSO	El Niño-Southern Oscillation
EOS	Earth Observing System
EQSOI	Equatorial Southern Oscillation Index
ESA	European Space Agency
ETM+	Enhanced Thematic Mapper Plus
EU	European Union
EV^2	group of EVOH and EVA plastic types
EVA	ethylene vinyl acetate
EVOH	ethylene vinyl alcohol
f-gases	fluorinated gases
FAO	Food and Agriculture Organization
FIRMS	Fire Information for Resource Management System
FPA	Focal Plane Array
FT-IR	Fourier Transform Infrared spectroscopy
GDP	gross domestic product
GESAMP	Group of Experts on the Scientific Aspects of Marine Environmental Protection

GFED	Global Fire Emissions Database
GFZ	German Research Centre for Geosciences, Helmholtz Centre Potsdam (German: "GeoForschungsZentrum")
GIZ	German Corporation for International Cooperation (German: "Gesellschaft für Internationale Zusammenarbeit")
GPS	Global Positioning System
GRD	ground range detected
GSD	ground sampling distance
Gt	gigatonnes (metric tons)
HD_{norm}	hydrodynamic model normalized values
HGU	right to cultivate license (Indonesian: "Hak Guna Usaha")
HTE	high-temperature events
IPCC	Intergovernmental Panel on Climate Change
IR	infrared
ISPRA	National Institute for Environmental Protection and Research (Italian: "Istituto Superiore per la Protezione e la Ricerca Ambientale")
L8	Landsat-8
LEO	low Earth orbit
LiDAR	light detection and ranging
LOOCV	leave-one-out cross-validation
L_{up}	above water (upwelling) radiance
L_{sky}	sky radiance
MERIS	Medium Resolution Imaging Spectrometer
MF	mangrove forest
MODIS	Moderate Resolution Imaging Spectroradiometer
MoEF	Indonesian Ministry of Environment and Forestry
Mt	megatonnes (metric tons)
MWIR	mid-wave infrared
N_2O	nitrous oxide
NAFTA	North American Free Trade Agreement
NASA	National Aeronautics and Space Administration
NIR	near-infrared
NP	nonylphenols
OBIA	object-based image analysis
OLI	Operational Land Imager
P	plantation
PA	polyamide
PA6	polyamide/nylon 6
PBDE	polybrominated diphenyl ethers
PDLF	primary dry land forest
PE	polyethylene
PEST	polyester
PET	polyethylene terephthalate
Pg C	petagrams carbon
POP	persistent organic pollutant

x

PP	polypropylene
PS	polystyrene
PSF	primary swamp forest
PUR	polyurethane
PVAL	polyvinyl alcohol
PVC	polyvinyl chloride
REDD+	Reducing Emissions from Deforestation and Forest Degradation
RMSE	root-mean-square error
ROMS	Regional Ocean Modelling System
R_{RS}	remote sensing reflectance
RS_{norm}	remote sensing model normalized values
r_{wa}	rho water (proportion directly back-reflected skylight at the air-water interface)
S	scrubland
S2	Sentinel-2
S&S	savannah and swamp
SAN	styrene acrylonitrile
SAR	synthetic aperture radar
SBR	styrene butadiene rubber
SDLF	secondary dry land forest
SIMC	Servizio Idro-Meteo-Clima (division of Arpae)
SNAP	Sentinel Application Platform
SNR	signal-to-noise ratio
SOI	Southern Oscillation Index
SPM	suspended particulate matter
SRF	spectral response function
SSF	secondary swamp forest
SSS	sea surface salinity
SST	sea surface temperature
SWAN	Simulating WAves Nearshore model
SWIR	short-wave infrared
TET-1	Technologieerprobungsträger-1
TIR	thermal infrared
UNEP	United Nations Environment Programme
UNFCCC	United Nations Framework Convention on Climate Change
UNIVPM	Università Politecnica delle Marche
USD	United States Dollar
USGS	United States Geological Survey
VNIR	visible and near-infrared
VH	vertical-horizontal polarization
VMP	virtual microplastic particle
VV	vertical-vertical polarization
WAC	Western Adriatic Current
WHOI	Woods Hole Oceanographic Institution
WWF	World Wildlife Foundation
yr	year

TABLE OF CONTENTS

Introduction

Environmental changes are increasing rapidly around the globe. In some areas, these changes manifest themselves as increased fire susceptibility due in part to prolonged droughts, or in other areas as polluted fish harvests. Anthropogenic activities are hypothesized to be a root cause of many of these changes, but our still lacking understanding of complex ecosystem function and interconnections limits our ability as ecologists to make definite conclusions as to cause and effect. Often these limitations are due to spatially restricted observations of processes occurring over very large areas. This thesis aspires to provide tools to better monitor results of anthropogenic activities, specifically tropical peatland burning in Southeast Asia as a significant contributor to greenhouse gas emissions and spread of river-based plastic pollution in coastal ocean systems.

Climate change

Climate change poses one of the largest potential threats to our current existence on this planet (IPCC, 2014). By destabilizing the global weather system, changes are being forced concurrently on multiple ecosystems across the planet (Hulme, 2005). Changes in precipitation rates, relative humidity, solar radiation, wind speed and evapotranspiration are expected to regionally play a dominant role in addition to changes in surface temperatures (Hulme, 2005). Shifts due to climate change in the geographic range of many terrestrial and marine species have been well documented (IPCC, 2014). Furthermore, it is projected that the majority of coral reef systems worldwide will be severely threatened by frequent thermal stress events that result in bleaching events and reef die-off (Donner, 2009). Whether these ecosystems are resilient enough to adapt to rapid changes remains a topic of intense study, and with the continued course that mankind is following, we are performing the experiments rather dangerously on the very system that we depend upon. Large fluctuation cycles in the global climate have occurred an estimated seven times over the last 650,000 years. The end of the last ice age occurred over 11,000 years ago, marking the beginning of the relatively stable modern global climate and concurrent to when human civilizations began to flourish. Historical global climate fluctuation cycles are hypothesized to be primarily due to processes such as slight shifts in the Earth's rotation around the Sun or the separation of the equatorial ocean current through the formation of Central America.

Current climate change however is accepted as extremely likely (95–100% confidence interval) to be driven in large part by anthropogenic emissions, notably carbon dioxide, methane, nitrous oxide and fluorinated gases (IPCC, 2014). Based on the Fifth Assessment Report of the IPCC (IPCC, 2014), global greenhouse gas emissions in 2010 amounted to a total of 49 Gt CO2-eq (gigatonnes of carbon dioxide equivalents), which consisted of 76% CO_2, 16% CH_4, 6% N_2O and 2% f-gases. A little over one seventh of CO_2 emissions (or about one tenth of total emissions) are estimated to come from human-induced forestry and land use changes, which includes deforestation, land clearing for agriculture, and degradation of soils. Agriculture, forestry and other land use is estimated to account for 25% of total emissions, which incorporates emissions from forest and peat fires as well as peat degradation (IPCC, 2014). Vegetation burning releases CO_2, CH_4, N_2O to the atmosphere as well as aerosols such as black carbon (IPCC, 2014). FAO estimates (FAO, 2013; IPCC, 2014) of annual emissions from forestry and land use between the years of 2001 to 2010 were 3.2 Gt CO2-eq/yr, of which 0.3 Gt CO2-eq/yr is attributed to biomass fires (including peatland fires) and 0.9 Gt CO2-eq/yr to degradation of peatlands through primarily drainage. The fires which swept across Indonesia in 2015 are estimated to have alone released 1.75 Gt CO2-eq into the atmosphere (World Bank, 2015). Peat fires in particular can produce very high levels of carbon emissions (Gaveau et al., 2014; Muraleedharan et al., 2000; Page and Hooijer, 2016) and are the focus of Section I.

Oceans

The world's oceans, as well as the estimated 10-12% of the globe's population dependent on ocean resources for their livelihood (FAO, 2014), face severe issues. Climate change is regarded as a driving factor in many changes to the oceans. Studies based on coastal tide gauge records over the past century together with satellite altimetry measurements since the 1990's reveal that the oceans are currently rising at an average rate of 2.8-3.2 mm/yr (Church and White, 2011). This is hypothesized to be due to factors such as rising heat content of ocean water together with melting of land glaciers and ice caps as well as the major ice sheets in Antarctica and Greenland. Changes in ocean heat budgets together with the introduction of massive amounts of freshwater have a direct effect on large ocean current systems. These currents are dependent on forcing through the transport of dense, cold water into the deep oceans. This in turn has numerous effects on global wind and weather systems tied to heat exchange processes with the ocean.

2

Furthermore, increased atmospheric CO_2 levels also enact a chemical change within the oceans. Similar to any gas-air interface, the ocean and atmosphere are continually in a state of maintaining equilibrium. Increased CO_2 levels in the oceans, commonly known as ocean acidification, results in reductions of available carbonate levels that many hard-shelled marine species depend upon for growth of shell and other calcified structures. One of the most striking examples of the effects of ocean acidification together with warming water temperatures is from massive coral bleaching events in places such as the Great Barrier Reef. Coral reefs are further threatened by abandoned fishing gear, popularly given the name of "ghost nets", which become entangled in reefs and continue to kill reef animals (Donohue et al., 2001). Small plastic particles have been found in some areas of the oceans to be as numerous as planktonic food item (Di Mauro et al., 2017), which get ingested by these animals (Cole et al., 2015) and can eventually led to food that lands on our dinner plates (Karami et al., 2018). Among the litany of increasing issues facing our oceans, plastic debris has been a recognized threat since the 1970's that only recently has begun to gain the attention of international legislation bodies. A deeper analysis of the history and current status of plastic pollution within the oceans is presented in Section II.

Section I: Fire, peat and forest biomass

I.1. Developing world

Having only recently achieved the status of a newly industrialized country, Indonesia continues to make a large portion of its national product by selling raw materials, such as timber and agricultural goods. High demand supports excessive production practices, especially in agricultural sectors, which often comes at accompanying high environmental prices. Asian countries in particular are often criticized for their lack of care for the environment with respect to their industrial production goals.

Indonesia has experienced difficult political upheavals over the past century, beginning hopeful enough with its independence in 1945 from Dutch colonial rule following Japanese military occupation. Political unrest following independence led to the New Order regime under Suharto, which spanned five presidential terms from 1966 to 1998. A focus of the regime was economic growth through intense foreign investment, supported by the US, with little regard to curbing corruption and allowance of political opposition. One project undertaken towards the end of the New Order, in 1996, was the

Mega Rice Project in Kalimantan, the southern region of Indonesian Borneo. The project aimed to convert unproductive peat swamp forest into fertile agricultural areas for rice production. This came in answer to Indonesia's increasing interest in food self-sufficiency for a growing population and transmigration policies aimed to enhance development of less populated islands (Goldstein, 2016). Over two years, the Ministries of Public Works and of Transmigration, Forestry and Agriculture coordinated to excavate thousands of kilometers of drainage canals and clear vegetation from one million hectares of peat swamp forest. Circa 40,000 farmers from Java and Bali were moved and granted a small plot of cleared land on which to cultivate rice, but Javanese rice cultivation practices proved non-functional in the acidic peat soil environment (Goldstein, 2016). The canals served very well to drain the water table of the peatlands, exposing carbon stores built up over millennia to oxidative microbial activity and desiccation (WWF-Indonesia Sebangau Project, 2012). These waterways also served to open up new forest regions to both industrialized logging and illegal tree harvesting activities through providing easier transport of timber from remote areas to processing and shipping locations (Barber and Schweithelm, 2000; WWF-Indonesia Sebangau Project, 2012). Some of the highest nationwide deforestation rates between 2000 and 2012 were observed over peatlands in Kalimantan (Margono et al., 2014). Palm oil production is an important part of the Indonesian economy (33.5 million tonnes produced in 2014, or $627 million USD of annual export earnings), and many of the drained and cleared peatlands have been converted to agricultural concession.

I.2. El Niño-Southern Oscillation

El Niño-Southern Oscillation (ENSO) refers to the irregular periodic fluctuation of sea surface temperatures over the Eastern and Central Tropical Pacific Ocean (termed El Niño/La Niña) together with the oscillation of air pressure systems over the eastern and western Tropical Pacific (termed Southern Oscillation). The neutral ENSO phase is characterized by a low-pressure air system in the West Pacific over Indonesia and a high-pressure air system in the East Pacific offshore of South America (Figure 1). These pressure systems represent the two outer edges of the atmospheric Walker Cell usually positioned over the Equatorial Pacific, with warm, humid air rising up into the troposphere over Southeast Asia (thus the low air pressure system) and cool, dry air falling onto the equatorial Eastern Pacific offshore of the American continents (thus the

4

high air pressure system). This pressure gradient provides for surface winds traveling westward along the equator, strengthening the North and South Equatorial Currents and supporting upwelling of cool, deep ocean water along the South American coastline, especially in front of Peru. This upwelled cool water extends westward across the equatorial Pacific. The atmospheric pressure systems provide for wet, rainy conditions over much of Southeast Asia and dry conditions along the coastline of Peru and Ecuador (Trenberth, 2002).
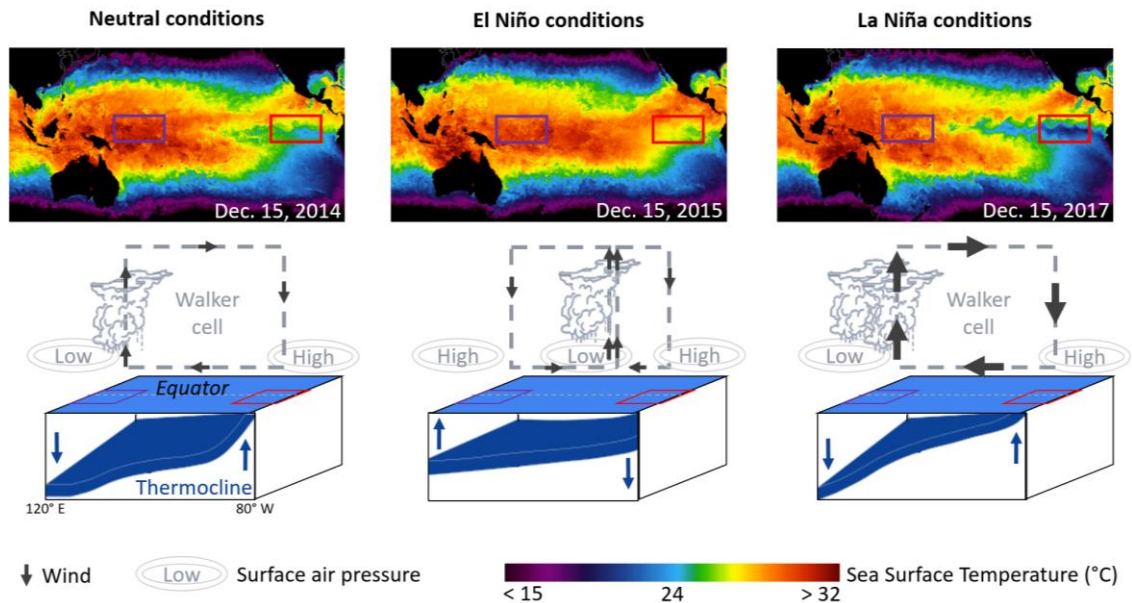
Figure 1: Overview of meteorological and sea surface conditions over the Pacific Ocean during neutral conditions years as well as during El Niño and La Niña events. Sea surface temperature, from the GHRSST Level 4 G1SST dataset that combine both *in situ* and remote sensing measurements from eight satellite systems, over the Pacific Ocean is displayed along the top, ranging from dark purple for temperatures 15 °C and below to deep red for temperatures in excess of 32 °C. A strengthened warm pool through equatorial waters during the strong 2015/16 El Niño can be observed extending to the coast of Central and South America. Increased cold water upwelling along the South American coastline and an extended cold-water tongue can be observed during the most recent La Niña event. Purple and red boxes correspond to those in the graphic below, which depicts changes in air pressure system along the equatorial axis (gray arrows and dashed lines) and in thermocline position (dark blue band). Positions of low and high-pressure systems at the Earth's surface are also indicated.

Semi-periodically the Walker Circulation weakens through eastward movement of the Southeast Asian low-pressure system along the Tropical Pacific, which results in slowed or even reversed winds along the equator (Tomczak and Godfrey, 1994). This produces what is called a warm ENSO phase, also known as El Niño (Figure 1), and is characterized by both weakening of equatorial currents as well as the western Tropical Pacific warm water pool extending further east along the equator (out to 120°W). El Niño events are also termed negative ENSO phases in reference to the Southern Oscillation Index (SOI), a comparison of the relative air pressure between Darwin in northern

Australia and Tahiti in the mid-Pacific Ocean, both of which have been measured since the 1800s (Halpert and Ropelewski, 1992). The Equatorial Southern Oscillation Index (EQSOI) has been implemented in modern times, which is more appropriately based on air pressures over Indonesia and the Equatorial Pacific offshore of South America. The term Southern Oscillation was first introduced by Gilbert Walker (for whom the Walker Cell is named) in 1924 (Walker, 1924), who together with other researchers such as Jacob Bjerknes (Bjerknes, 1969, 1966) is credited with identifying the relationship of sea surface temperatures in the Equatorial Pacific with air pressure system oscillations.

La Niña (also termed either cold or positive ENSO phase) can be considered the opposite of an El Niño, in that the low-pressure system over Indonesia and the high-pressure system offshore of South America both intensify (Figure 1). This leads to stronger winds blowing eastward along the equator, which strengthens the equatorial currents, induces stronger upwelling of cool, nutrient-rich deep water off the South American coastline, and pushes the West Pacific warm water pool closer to Southeast Asia. Both ENSO phases are responsible for global changes in temperature, as well as anomalous weather patterns, in particular variations in rainfall amounts (Ropelewski and Halpert, 1987; Trenberth, 2002). One of the strongest El Niño events recorded in recent history occurred in 1982/83, causing an estimated $10 billion to $13 billion USD in weather-related damage across the globe and up to 2,000 deaths (FAO, 1997; WHOI, 1986). This together with a massive coral reef bleaching event (estimated 16% worldwide) in conjunction with the 1998/99 El Niño (Normile, 2016) has greatly increased interest from both the scientific and global economic community to understand ENSO mechanisms and its effects on global climate.

Based on historical reanalysis of the last century, the strongest El Niño events occurred 1982/83, 1997/98 and 2015/16 (Huang et al., 2016). Links between recent variations in ENSO events and global climate change have been hypothesized, with an increase of up to 60% in the amplitude in ENSO variability over the last 50 years after detrending for other meteorological events (Zhang et al., 2008). The complete mechanisms responsible for variation in the Walker Cell circulation are not yet well understood, thus connection between ENSO with global climate change remains primarily speculation dependent on correlation studies. El Niño events are associated with below average rainfall over Indonesia and parts of Australia (Halpert and Ropelewski, 1992; Trenberth, 2002). For Indonesia, this translates to an extended dry season before onset of the monsoon rains (Ropelewski and Halpert, 1987), which creates

drier than usual conditions and thus increasing the risk of large fire events (Siegert et al., 2001). An El Niño event temporarily reduces the GDP of Indonesia (Cashin et al., 2015). Given that current climate models predict that ENSO events will occur more often and with increased severity in the decades to come, both fire risk assessment and improved fire management should be a priority for the Indonesian government.

I.3. Current fire control in Indonesia

Burning remains the easiest and cheapest method to clear land for planting in Indonesia (Simorangkir, 2006), and fires often burn uncontrolled into neighboring forest and drained peatland areas. An in-depth discussion of fire control history in Indonesia and associated global greenhouse emissions is presented in both chapters 1 and 2. The most recent large fire event in 2015 cost the country over $16 billion USD or 1.9% of their GDP (World Bank, 2015). The emissions released through these fires, over a mere three weeks, gained Indonesia the title of fifth largest carbon-emitting country worldwide. International pressure has long been mounting on Indonesia to implement better fire management practices, as exemplified by the ASEAN (Association of Southeast Asian Nations) Agreement on Transboundary Haze Pollution and the UNFCCC (United Nations Framework Convention on Climate Change) initiative to reduce emissions from deforestation and forest degradation, increase the role of conservation and sustainable management of forests, and enhance forest carbon stocks in developing countries (coined the name REDD+). Indonesia's current presidential administration under Joko Widodo responded in 2011 by introducing legislation which placed a moratorium on new palm oil concession licenses. Despite this, new concessions not listed in the Indonesian Ministry of Environment and Forestry's Right to Cultivate (Hak Guna Usaha, HGU) license registry are easily identified from satellite images. Furthermore, this did little to hinder the catastrophic air pollution resulting from the 2015 fires. Marlier et al. (2015) list direct suggestions to help protect regional public health, including limiting the use of fire by timber and oil palm industries through improving monitoring systems and strengthening infrastructure of local-level management as well as enforcement of existing fire bans. A likely limiting factor for improved fire management practices could be the funds that the government can allocate for this activity. If this is indeed the case, it underlines the importance of developing a low-cost system that still allows for very efficient and accurate monitoring of fire and emission estimates over the entire country.

Remote sensing can cover very large areas for low costs relative to those needed for on the ground monitoring of the same area. There are multiple satellite missions which provide their data for free, offering the benefit that a large portion of the costs are being shouldered by entities such as the European Space Agency (ESA) and the National Aeronautics and Space Administration (NASA).

I.4. Remote sensing systems to improve fire control and provide rapid burned area estimates

Section I of this thesis presents two examples of remote sensing systems for monitoring fires and burned area in Indonesia, which are both built upon freely available satellite data. Chapter 1 is based upon passive sensor data, a type of sensor system that is characterized by measuring sunlight reflected by the Earth's surface or other types of emissions such as thermal radiation from fires (Figure 2). Chapter 2 introduces the benefits of an active sensor system, that of synthetic aperture radar (commonly known as SAR), characterized by the sensor producing a radio wave signal whose echo is then recorded after bouncing off the Earth's surface. Echo is here defined to include the effects of signal reflection, refraction and scattering upon encountering a surface. How the microwave signal is echoed provides information on surface properties such as roughness and moisture content.
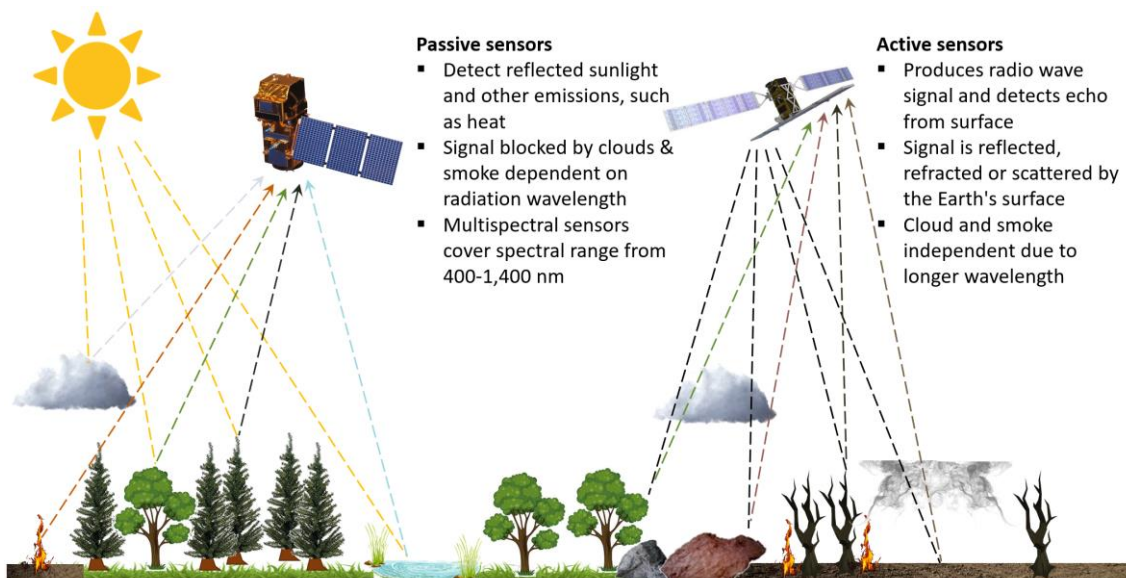
Figure 2: Comparison of passive and active satellite sensor systems used in land and water remote sensing. A passive sensor detects reflected sunlight off various surfaces and other emitted radiation (such as thermal infrared from fires), the signal of which can be blocked by clouds and smoke dependent on light wavelength. Active sensors produce a radio wave signal that echoes off the Earth's surface, independent of cloud/smoke cover, and provides information such as surface roughness or moisture. Light/microwave paths are demonstrated with hatched lines, note that processes such as atmospheric reflection and scattering are purposely not displayed to retain a simple overview.

Passive satellite systems include the Landsat, Sentinel-2 and FireBird satellite missions (Table 1). They are all in low Earth orbit (referred to as LEO), meaning that they are flying at an altitude between 160-2,000 km. Landsat presents the longest continuous global imaging data available to the public, offering images from 1972 until present. Both Landsat-8 and -7 are multispectral sensors, meaning that they measure light using a small number of spectral bands (multispectral refers to number of available bands being on the order of 3 to 30). The concurrent operational constellation provides a revisit time of 8 days, although Landsat-7 data quality is reduced due to a scan line correction failure. ESA's Sentinel-2 mission provides finer pixel ground spatial resolution, down to 10 m, and covers a greater number of spectral band ranges in the VNIR (visible and near-infrared) as compared to the Landsat satellites. With the current two satellite constellation, acquisition revisit time has been lowered to 5 days. The satellites in the FireBird mission from the German Aerospace Center (in German "Deutsches Zentrum für Luft- und Raumfahrt" or DLR) are specifically designed for very accurate and precise detection of high temperature events, such as fires or volcanos. The bi-spectral infrared (IR) sensor onboard allows for much finer pixel ground resolution detection, which is discussed further in chapter 1.

Table 1: Overview of relevant satellite system parameters. Abbreviations are as follows: DLR German Aerospace Center, USGS US Geological Survey, NASA National Aeronautics and Space Administration, ESA European Space Agency, IR infrared, VNIR visible and near-infrared, MWIR mid-wave infrared, TIR thermal infrared, SWIR short-wave infrared.

Mission (agency)	Currently orbiting satellites	Sensor system	Launch date	Spectral bands (central wavelength)	Ground spatial resolution	Orbit altitude
Landsat (USGS/ NASA)	Landsat-8	OLI/TIRS	February 2013	VNIR: 5 bands (0.44,0.48,0.56,0.65,0.87μm) SWIR: 3 bands (1.37, 1.61, 2.20 μm) TIR: 2 bands (10.90, 12.00 μm) Panchromatic band (0.59 μm)	VNIR/SWIR 30 m, TIR 100 m, Pan 15 m	705 km
	Landsat-7	ETM+	April 1999	VNIR: 4 bands (0.49, 0.56, 0.66, 0.84 μm) SWIR: 2 bands (1.65, 2.22 μm) TIR: 1 band (11.45 μm) Panchromatic band (0.71 μm)	VNIR/SWIR 30 m, TIR 60 m, Pan 15 m	705 km
Sentinel-2 (ESA)	S2A, S2B	MSI	June 2015, March 2017	VNIR: 10 bands (0.44, 0.49, 0.56, 0.67, 0.71, 0.74,0.78,0.84,0.87,0.95μm) SWIR: 3 bands (1.38, 1.61, 2.12 μm)	10, 20, 60 m	786 km
FireBird (DLR)	TET-1, BIROS	bi-spectral IR, VNIR	July 2012, June 2016	VNIR: 3 bands (0.51, 0.64, 0.86 μm) MWIR: 1 band (3.8 μm) TIR: 1 band (8.9 μm)	160 m	500 km
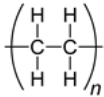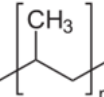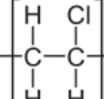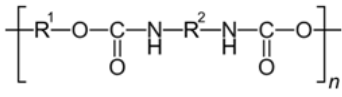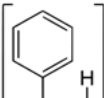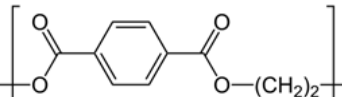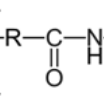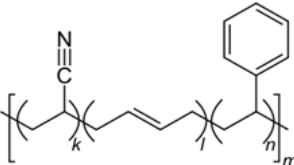
Sentinel-1, the system utilized in chapter 2, is an active SAR sensor (Figure 1). Emitted microwaves (specifically C-band in the case of the Sentinel-1 satellites, defined as wavelengths between 7.5 – 3.75 cm) move unhindered through thick cloud and smoke cover, clearly demonstrating the promise of such a technology for being able to detect burned area concurrent to when fires are actively producing heavy emissions. Sentinel-1A was launched April 2014 and was followed two years later by Sentinel-1B. By comparing before and after acquisitions, change in signal strength can be translated into estimates of lost biomass.

Section II: Plastic in waterways and the oceans

II.1. Plastic production and waste

Plastic mass production began in the 1940s and 50s, when polymers such as polystyrene (PS), polyvinyl chloride (PVC), polyethylene (PE), polypropylene (PP) and polyethylene terephthalate (PET) where developed enough to allow creation of commercial products. Since this time, global production has increased exponentially to reach 332 megatonnes (Mt) in 2015 (PlasticsEurope, 2016), of which about half comes from Asia and circa 20% from NAFTA and EU each (Andrady, 2017). Controlling for population growth reveals that per capita plastic consumption has increased non-linearly within the last years (Andrady, 2017), expanding from 100 kg in 2007 to 140 kg in 2015 for North America and Western Europe (Lebreton et al., 2012). It is estimated that more than one third of plastic production goes into the creation of disposable packaging (Derraik, 2002; Galgani et al., 2017; Thompson et al., 2009), as can also be observed in the common uses listed in Table 1. This packaging is usually discarded within one year of production, accounting for a large portion of the 11.5 Mt of plastic dumped into landfills in 2006 (Jambeck et al., 2015; Lebreton et al., 2012).

Table 2: Overview of primary plastic types, listing their common abbreviated name (Abbr.), the monomer atomic structure, some of its common uses, and market demand in megatonnes (Mt; PlasticsEurope, 2014) as well as percentage of global plastic production (Geyer et al., 2017).

Type	Abbr.	Atomic structure	Used in	Demand (Mt, %)
Polyethylene	PE		Packaging: plastic bags & films, membranes, containers, bottles	13.7 (36%)
Polypropylene	PP		Packaging and labeling, textiles, lab equipment, banknotes	8.8 (21%)
Polyvinyl-chloride	PVC		Construction, packaging, insulation, imitation leather	4.8 (12%)
Polyurethane	PUR		Foam seating, insulation, seals, gaskets, adhesives, surface coatings	3.4 (< 10%)
Polystyrene	PS		Packaging, food containers, lids, cups and bottles, trays, tumblers, disposable cutlery	3.3 (< 10%)
Polyethylene terephthalate	PET		Synthetic fibers, thermoforming applications, beverage and food packaging	3.2 (< 10%)
Polyamide/ Nylon 6	PA6		Thread, ropes, filaments, nets, garments, surgical sutures	0.9 (< 5%)
Acrylonitrile butadiene styrene	ABS		Auto components, electronics, protective carrying cases, appliances, toys, sports equipment	0.7 (< 5%)

Within the EU, landfills have been banned from eleven countries but remain the top waste management practice for more than half of the remaining countries (PlasticsEurope, 2016). Worldwide, plastics make up 10-15% of municipal waste by weight (Andrady, 2017). Of the estimated 8,300 Mt of plastic to have been produced between 1950 and 2015, 6,300 Mt have become plastic waste (Geyer et al., 2017).

Worldwide, only 9% of this waste was recycled, 12% was incinerated or pyrolyzed and the remaining 79% has accumulated in landfills and the natural environment. In many developing countries, proper waste management infrastructure is lacking (Geyer et al., 2017; Jambeck et al., 2015), leaving individuals with the choice to either burn their waste, often with lacking emission filters and the accompanying high health risks, or to discard it in impromptu landfills and nearby waterways. What is even recognized as waste can vary widely, exemplified with anthropogenic debris objects less than 5 mm long not being recognized by the state of California as waste.

Plastic waste can be categorized based on object diameter, with particles <5 mm being termed microplastics and objects larger as macroplastics (Galgani et al., 2013). Microplastics especially have been a focus in recent legislation initiatives (G7 Germany, 2015; GESAMP, 2016; UNEP, 2016). Primary microplastics are introduced to the environment through sources such as hygiene products (facial scrubs, toothpaste, cosmetics), surface abrasion (through replacement of sand in sand blasting) and production pellets (also known as nurdles). Secondary microplastics are the product of macroplastic degration within the environment due to processes such as solar radiation, wind and abrasion. A third recognized source of microplastics to the environment comes from synthetic textiles, especially during washing. Up to 0.1 mg micrometer plastic fibers are released per gram of washed textile during each machine wash (Hernandez et al., 2017). Waste water treatment plants, including in developed countries, are often not sufficiently equipped with facilities to capture microplastics out of effluents.

II.2. Plastic debris in the oceans

It is estimated that each year between 10 and 20 Mt of plastic debris enter the ocean (UNEP, 2014), of which 5 – 13 Mt are thought to stem from land-based sources (Jambeck et al., 2015). Plastic products are prized in industry and consumer goods for their lightness and durability, but it is exactly these characteristics which pose a problem once plastics are introduced as debris into marine systems. Global sampling efforts for marine plastic focus primarily upon the surface, either through visual surveys of macroplastic or net-trawl sampling for microplastic. The most commonly found plastics from these surveys are PE, PP and PS (Zhang, 2017), reflecting relative production numbers (Table 1) and their buoyancy, with virgin plastic densities being less than that of seawater. Estimates of the amount of plastic pollution currently floating in the oceans are wide

ranging. The most recent global estimate of floating microplastic debris within the oceans stands at 236 thousand tonnes (van Sebille et al., 2015), greatly exceeding previous estimates of Cózar et al. (2014; 7 to 35 thousand tonnes) and Eriksen et al. (2014; 36 thousand tonnes). All estimates of plastic load within the oceans are at least two orders of magnitude less than the estimates mentioned above of the amount of plastic entering the ocean each year (van Sebille et al., 2015). These estimates are based on collective *in situ* surface water trawl samples over multiple expeditions throughout the world's oceans. In a recent study, Kooi et al. (2016) determined that buoyant surface microplastic particles have a much more complex vertical distribution than before perceived, being able to be mix down to 5 m dependent on wind conditions, which can pose the potential for underestimating concentrations by up to 2.5 times when solely relying on surface trawls. Plastic particles in the environment furthermore change their buoyancy characteristics with time through biofouling, leaching, flocculation and accumulation, all of which to date have proven difficult to study in realistic field conditions. Given the large sources of uncertainty in collecting accurate and precise field samples of plastic concentrations, it is not surprising that global estimates of plastic load within the oceans have proven to be quite difficult.

The environmental and health issues posed by plastic, in particular microplastic debris, in the ocean and inland waterways are discussed in more detail in Chapter 3. Marine macroplastic are further estimated to incur costs up to $13 billion USD in environmental damage (UNEP, 2014). Especially derelict fishing gear, such as the above mentioned ghost nets, were early identified as a hazard which required monitoring by any means possible. These ghost nets continue to catch and kill marine life long after any fisherman could glean a benefit therefrom (Sheavly and Register, 2007). Ghost nets can be large, a tangle of ropes and meshes up to many meters in diameter, and are able to jam a propeller or clog a ship's motor if inadvertently taken into the coolant system uptake. This poses a safety hazard and financial problem for both industry, private and military shipping activities. Infrequent monitoring activities began with ship-based or aerial visual surveys, but have since grown to include ocean current modelling efforts (such as van Sebille et al., 2015) or remote sensing methodologies. Pichel et al. (2007) were one of the first to demonstrate that remotely sensed water parameters could be implemented together with a good mechanistic understanding of regional hydrological processes to assess likelihood of macroplastic debris accumulation along a North Pacific convergent front. This methodology has proven difficult to implement in other regions

of the ocean, a potential clarification being the relationship between the utilized water parameters and hydrological features is regionally unique.

II.3. Rivers are a significant source

Rivers have been identified as one of the main sources of plastics to the ocean. Jambeck et al. (2015) estimated that between 4.8 and 12.7 Mt of plastic were discharged from rivers into the ocean in 2010 alone. Lebreton et al. (2017) offer a more conservative estimate of annual riverine discharge of plastic ranging from 1.2 to 2.4 Mt. The Lebreton et al. estimates are based on a global river hydrologic model that also accounts for population along the river, waste management practices within the country and seasonal fluctuations in river discharge. Based on their modelling, the top 20 polluting rivers account for two thirds of the global riverine plastic input and are mostly located in Asia. Freshwater systems have historically received less attention as compared to marine studies, with very few studies having focused on large river systems despite their apparent importance in the question of marine plastic monitoring (Lechner et al., 2014; Mani et al., 2015). Rivers have been identified in as important source pathway and as such, should be the focus of remediation activities to avoid the continued release of microplastics into the ocean (GESAMP, 2016).

II.4. How remote sensing data can help

Sampling *in situ* from a boat remains the surest method of obtaining ground truth points for measuring plastic concentrations at a particular location in an inland waterway or the ocean. This collection method is both highly costly and inherently limited to characterizing the relatively small area along a transect line. The movement of plastic in limnological and marine systems is highly variable in both space and time. It is thus of notable interest to determine a method in which point sampling on the ground can be upscaled to cover a much larger area. Pichel et al. (2007) demonstrated that water parameters, which have an established history of remote sensing, together with understanding of the underlying hydrological mechanisms can successfully be used to model plastic accumulation in the aquatic environment. Water parameters can be used to identify a specific body of water and track how it moves through time. River plume water is most often less dense than coastal ocean waters and can be observed to remain as a separate water body long after having left the river mouth. With knowledge of plastic

concentration within river water as it flows into the ocean, it stands to reason that this plastic can be then tracked by using the river plume as a proxy. Chapter 3 of this thesis examines the microplastic being emitted by the largest river in Italy, the Po, and utilizes two different modelling tools to track how that microplastic debris is spreading and accumulating along the coastline. The goal of such a methodology would be to develop the basis for a monitoring system for environmental groups and government agencies responsible for either clean-up or source reduction activities.

Aims of the thesis

The goal of this thesis is to demonstrate how remote sensing systems can be used as a tool to gain large scale coverage information of natural catastrophes resulting from anthropogenic activities. While the research areas of fire in Southeast Asia and plastic in aquatic environments are disparate issues, common aspects exist in the difficulties confronting development of functioning monitoring systems, especially the problem of geographical scale and available financing. Regular on the ground or *in situ* monitoring measurements are costly, as well as at times dangerous, and are often unfeasible to cover the entire effected area. In the case of fire monitoring in Indonesia, proper infrastructure is lacking in many remote regions of this massive nation and the funds for providing large-scale measurements of fire characteristics and greenhouse gas emissions are lacking. Chapter 1 of this thesis deals with presenting a new fire monitoring system that allows for much improved identification of fire sources and burning characteristics, such as propagation speed. Chapter 2 presents a new state of the art remote sensing methodology for more quickly assessing burned area through being able to function independent of smoke or cloud-cover during and post fire events. The Indonesian government has already taken concrete legislation steps to limit logging and oil palm plantation expansion, but enforcement evidently remains difficult in remote areas. Remote sensing offers a method for cutting the financial costs of regularly controlling these activities over the entire country.

In the case of aquatic plastic debris monitoring, *in situ* monitoring points are very costly to acquire and are representative only for a particular location at a specific time. Aquatic systems are constantly in flux, making the spatial-temporal relationship of plastic transportation and accumulation complex and difficult to capture based on measurements made from a single boat over time scales from weeks to months. Remote sensing techniques to upscale point measurements to large-area regions offer an

opportunity to at least partially overcome this issue. Chapter 3 explores implementation of a remote sensing methodology to monitor accumulation of river-sourced microplastic debris along a coastline and compares the results to a more accepted form of microplastic tracking, namely that of ocean current modelling. These chapters serve to demonstrate how remote sensing data can be used as a monitoring tool in systems where collection of large-area representative *in situ* samples is for various reasons unfeasible. The monitoring systems presented here are of importance for contributing understanding of our impact on globally ecosystems that we depend on as a species for our continued well-being.

Results

Section I: Fire, peat and forest biomass

Chapter 1. Detection and characterization of low temperature peat fires during the 2015 fire catastrophe in Indonesia using a new high-sensitivity fire monitoring satellite sensor (FireBird)

Atwood EC, Englhart S, Lorenz E, Halle W, Wiedemann W, Siegert F (2016) Detection and characterization of low temperature peat fires during the 2015 fire catastrophe in Indonesia using a new high-sensitivity fire monitoring satellite sensor (FireBird). PLOS ONE 11(8): e0159410.

RESEARCH ARTICLE

Detection and Characterization of Low Temperature Peat Fires during the 2015 Fire Catastrophe in Indonesia Using a New High-Sensitivity Fire Monitoring Satellite Sensor (FireBird)

Elizabeth C. Atwood[1,2]*, Sandra Englhart[2], Eckehard Lorenz[3], Winfried Halle[3], Werner Wiedemann[2], Florian Siegert[1,2]

1 GeoBio Center, Department of Biology II, Ludwig-Maximilians-Universität Munich, Planegg-Martinsried, Germany, 2 RSS Remote Sensing Solutions GmbH, Baierbrunn, Germany, 3 Institute of Optical Sensor Systems, German Aerospace Center (DLR e.V.), Berlin-Adlershof, Germany

* atwood@rssgmbh.de

Abstract

Vast and disastrous fires occurred on Borneo during the 2015 dry season, pushing Indonesia into the top five carbon emitting countries. The region was affected by a very strong El Niño-Southern Oscillation (ENSO) climate phenomenon, on par with the last severe event in 1997/98. Fire dynamics in Central Kalimantan were investigated using an innovative sensor offering higher sensitivity to a wider range of fire intensities at a finer spatial resolution (160 m) than heretofore available. The sensor is onboard the TET-1 satellite, part of the German Aerospace Center (DLR) FireBird mission. TET-1 images (acquired every 2–3 days) from the middle infrared were used to detect fires continuously burning for almost three weeks in the protected peatlands of Sebangau National Park as well as surrounding areas with active logging and oil palm concessions. TET-1 detection capabilities were compared with MODIS active fire detection and Landsat burned area algorithms. Fire dynamics, including fire front propagation speed and area burned, were investigated. We show that TET-1 has improved detection capabilities over MODIS in monitoring low-intensity peatland fire fronts through thick smoke and haze. Analysis of fire dynamics revealed that the largest burned areas resulted from fire front lines started from multiple locations, and the highest propagation speeds were in excess of 500 m/day (all over peat > 2m deep). Fires were found to occur most often in concessions that contained drainage infrastructure but were not cleared prior to the fire season. Benefits of implementing this sensor system to improve current fire management techniques are discussed. Near real-time fire detection together with enhanced fire behavior monitoring capabilities would not only improve firefighting efforts, but also benefit analysis of fire impact on tropical peatlands, greenhouse gas emission estimations as well as mitigation measures to reduce severe fire events in the future.

23

Introduction

The fires that swept across Indonesia during the latter half of 2015 were catastrophic on many levels. Costs incurred from the fires to the Indonesian government are estimated to be in excess of USD 16 billion [1], signifying 1.9% of the national gross domestic product. Greatly reduced air quality in Southeast Asia is a consequence of major forest fires [2–4], and the resulting smoke cloud, coined the 2015 Southeast Asian Haze, spread across several countries, including Brunei, Indonesia, Malaysia, Singapore, Southern Thailand, Vietnam, Cambodia and the Philippines. The islands of Sumatra and Borneo were especially heavily impacted, with poor air quality causing a state of emergency to be declared in six Indonesian provinces. On Borneo, the province of Central Kalimantan was severely affected with Pollutant Standards Index (PSI) of fine particulate matter ($PM_{2.5}$) hitting recorded highs in excess of 1,500, far exceeding levels deemed hazardous for human health [5–7]. Borneo contains many tropical peatlands [8], and burning of peat swamp forests has been found to damage biodiversity [9], ecosystem structure [10] and local livelihood opportunities [11]. Initial emission estimates from the 2015 peat fires amount to 1.75 billion metric tons of CO_2 equivalents [1], placing Indonesia as the world's fifth highest carbon dioxide emitting country above other nations such as Japan and Germany [12,13].

Worldwide, tropical peatlands are estimated to cover an area ranging from 39–66 million hectares (ha), representing between 10–16% of global peatland resources [14,15]. Indonesia contains more than half of all known peatlands in the tropical zone, with an area ranging from 16–27 million ha [8,16] and translating to a peat carbon pool of 82–92 gigatons (GT) [14]. For millennia, Borneo has been primarily covered with tropical peatlands [8,16]. In recent decades, peat swamp forests in this region have been degraded through both industrial and illegal logging [6,17], industrial plantation activities [18,19] and infrastructure from failed development projects such as the Mega Rice Project [20,21]. Peatlands naturally have a high water table, lying at or just below the forest-covered surface [16]. Drainage infrastructure, such as canals, can contribute to lowering the water table [21–23], which is then compounded by drought periods coinciding with climatological events such as El Niño-Southern Oscillation (ENSO) [6,24–26]. The reduced water table allows drying of the peat layer, often for the first time in centuries [16], and thus becoming more susceptible to catching fire [21,22]. Fire is often utilized as a cheap, effective method to clear and maintain land for both agricultural and plantation development [27]. On Borneo, slash-and-burn techniques often result in fires spreading into surrounding un-slashed peat swamp forests [22]. Peatland fires are characterized by low intensity burning, which can spread into peat deposits up to 0.5 m below the surface [21,28], and can burn for long periods of time, often being very difficult to extinguish [22]. Smoldering peatland fires produce large amounts of particulate matter, CO and other gas compounds [22,29]. Peatland and forest fires in Indonesia during the 1997/98 ENSO event are estimated to have released 0.2–0.4 Pg C, accounting for at least 10% of the global total carbon emissions due to forest fires [30]. Conservation efforts have included the creation of national parks to slow the peatland degradation process, including the Sebangau National Park established in 2004 through a combined effort of the World Wildlife Foundation (WWF) and the Indonesian Ministry of Environment and Forestry (MoEF). Fires occurred both within the park and in neighboring regions from September-October 2015, although the extent of damage incurred remains to be clarified.

Many questions remain regarding better fire management practices to help avoid catastrophic fire events in Indonesia such as those in 1982/83, 1997/98 and recently in 2015. Remote sensing systems have been utilized for over three decades to support monitoring efforts [31–33]. Techniques using spectral bands in the visible and near infrared (VNIR) and the shortwave infrared (SWIR) are limited by smoke and haze coverage while fires are burning

24

[34], and thus the field has focused on sensors in the midwave and thermal infrared (MWIR & TIR) to detect active fires. The latter class of sensors include NOAA-AVHRR [35–37], GOES-VAS [38], ERS-ATSR [39,40], TRMM-VIIRS [41], and MODIS on the EOS Terra and Aqua satellites [42]. These sensors offer a pixel resolution from 1 km down to 375 m, and most saturate at a relatively low brightness temperature of ca. 300–340 K, with the exception of a single MODIS band (channel 21, 3.9 μm low-gain) which saturates at 500 K. Low sensor saturation inhibits proper detection of very large fire events [43]. While MODIS is best able to overcome this limitation, the 1-km pixel resolution hinders detection of initial fire fronts or separation of multiple small fires.

The Technology Experiment Carrier (TET-1) is one of two experimental satellites in the German Aerospace Center (Deutsche Luft- und Raumfahrt, DLR) FireBird mission. The onboard sensor saturates at 900 K, improving its ability to successfully detect high-temperature events (HTE) ranging from smoldering low intensity fires to large-area high intensity fires [43]. This, together with the sensor's 160-m spatial resolution, may result in improved active fire monitoring and allow measurement of fire dynamic behavior previously not possible.

In this paper, we explore whether TET-1 can provide improved fire detection capabilities than hereto existing systems, thus providing the basis for an improved early-detection fire management system. Focus is paid to peat fire dynamics (propagation speed, area burned) over different ground and vegetation types, as well as fire occurrence in and around concession areas. Finally, we provide a first estimate of the damage incurred to the Sebangau National Park and surrounding regions during the 2015 wildfires derived from detection algorithms for both active fire (MODIS, TET-1) and burned area (Landsat).

Materials and Methods

Study area and available metadata

The Sebangau National Park and surrounding areas sit upon peat layers reaching at least 9 m deep [16]. The park is home to many endemic and endangered species, including the clouded leopard, sun bear and Orang-Utan (critically endangered). Botanic biodiversity within the park comprises 106 different known species, which encompasses many orchid as well as medicinally useful plants. Prior to establishment of the park, the area was systematically logged through both industrial and illegal activities [6,44]. Neighboring the eastern boundary of the park is the location of the former Mega Rice Project. This project was initiated by the Indonesian Government in 1995 but subsequently ended three years later when recognized as a failure [20]. During this period, over 4,000 canals were constructed with the primary goal to establish land for agriculture but also succeeded in providing transport infrastructure for logs out of the forest. Through accelerating waterflow from the peatlands, this infrastructure contributed to lowering the water table and resulted in serious degradation of an area more than 1 million hectares in size [21,45]. Recent conservation efforts by the World Wildlife Foundation (WWF) include reforestation as well as building dams, with the goal to encourage a return to historical water table levels, thus preventing drying out of the peat layer [45] and reducing risk of fire [21,22].

The study area (Fig 1) was selected to cover the Sebangau National Park as well as neighboring oil palm concessions and degraded areas, and extended over 2,430,390 ha. Datasets for peat depth, primary forest cover and known plantation concessions were accessed from Global Forest Watch [46]. Peat depth data, covering both Indonesia and Malaysia, were made available by the Indonesian Ministry of Agriculture. Based upon these data, we separated the study area into regions of thin peat coverage over sand and the available peat depth classes: 0–1 m, 1–2 m and more than 2 m.

25
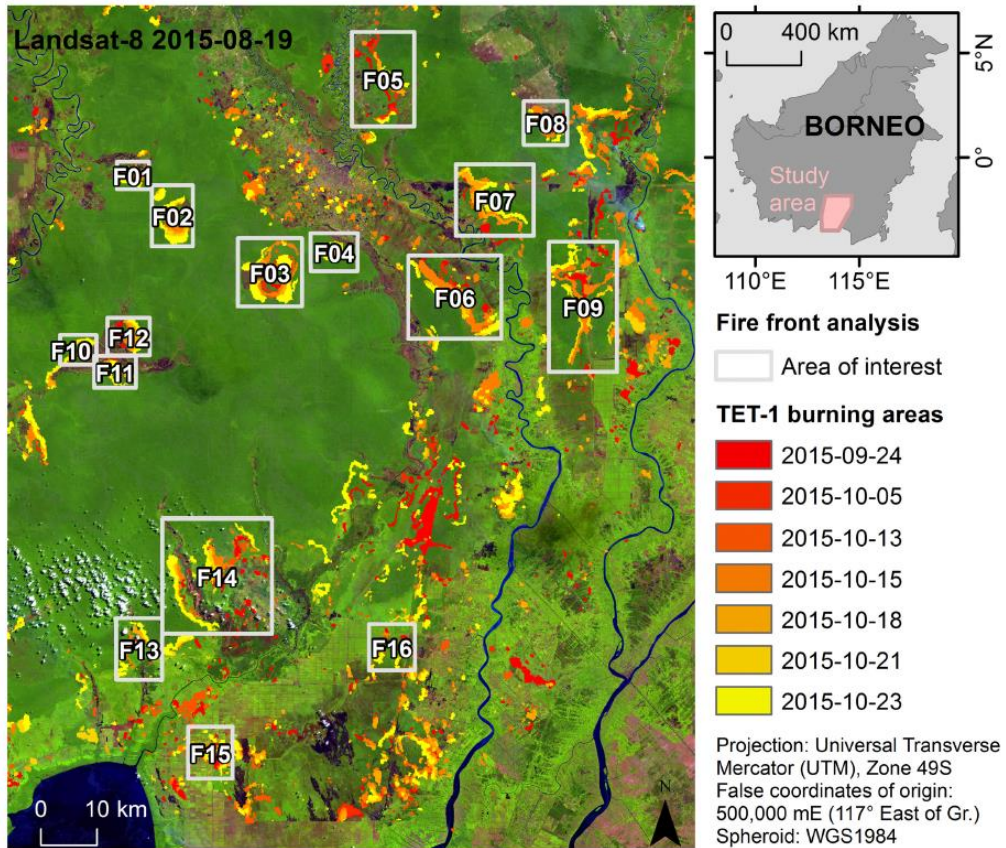
Fig 1. Study area and fire dynamic Areas of Interest (AOI) overview. Landsat-8 OLI image (false color: R, band 9 1.36–1.38 μm; G, band 5 0.85–0.88 μm; B, band 4 0.64–0.67 μm; source USGS/NASA) from Aug. 19th, 2015, overlain with TET-1 active fire classifications derived from seven acquisition dates (displayed in red to yellow). The AOI for each fire dynamic measurement area is indicated in light grey and study area location in Central Kalimantan, Borneo, is indicated in the inset.

doi:10.1371/journal.pone.0159410.g001

Unburned forest coverage, defined as having not burned within the last 30 years and created using a Landsat time series covering 2000–2012 [44], was used to make an initial separation of vegetation types. Additional land cover classification maps covering the time period 1990–2013 produced by MoEF were downloaded from Greenpeace [47]. The land cover data allowed further separation of previously burned areas into "swamp scrubland", covered by bushes and brush, and "swamp", covered primarily by grass and sedges. Unburned forest was termed "secondary swamp forest" to match the categories provided in the land cover dataset. Visual separation of unburned forest into mixed swamp, low pole and tall interior forest types was accomplished based on previous studies in the area [16], and analysis of Landsat-8 OLI imagery from August 2015 and Landsat-5 TM imagery from June 1991.

26
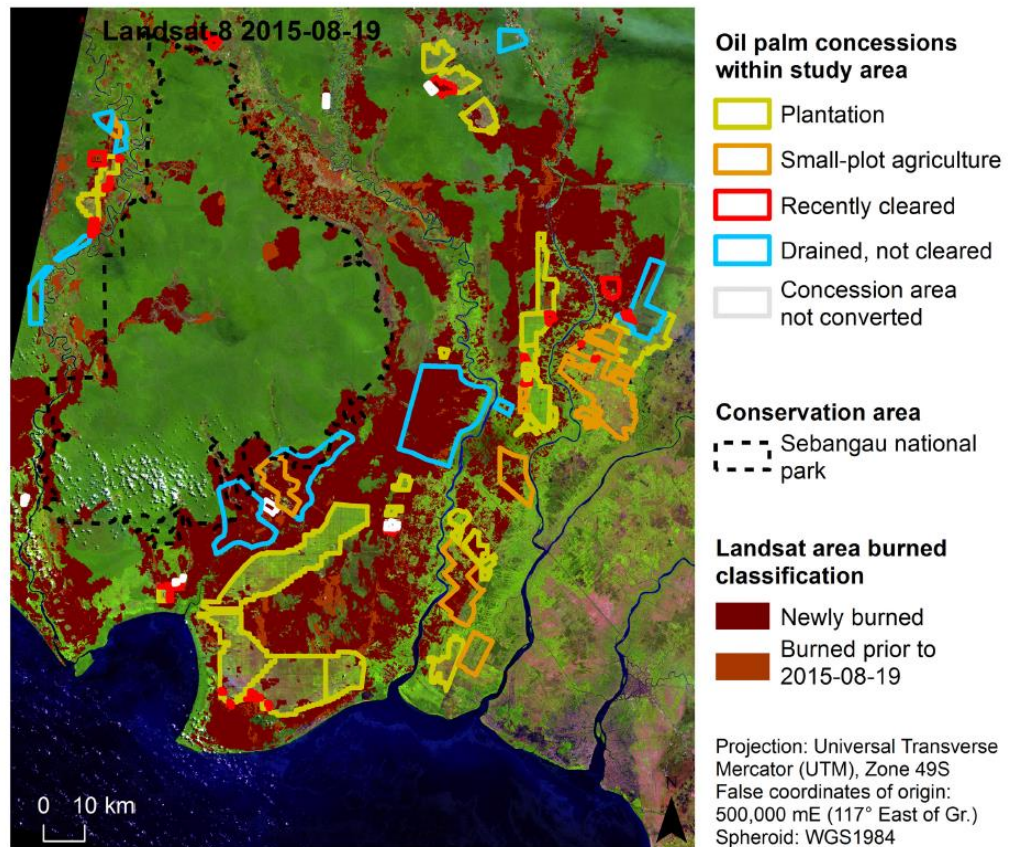
Fig 2. Oil palm plantation concessions and conservation areas. Landsat-8 OLI image (false color: R, band 9 1.36–1.38 µm; G, band 5 0.85–0.88 µm; B, band 4 0.64–0.67 µm; source USGS/NASA) from Aug. 19th, 2015, overlain with oil palm plantation concession classification, Sebangau national park boundary and Landsat burned area classification.

doi:10.1371/journal.pone.0159410.g002

Oil palm plantation concessions for the study area were made available by the MoEF and accessed from Global Forest Watch [46]. These data indicated which concessions either hold or are in the process of obtaining a Right to Cultivate license (Hak Guna Usaha, HGU). Further visual analysis of Landsat-8 OLI imagery revealed several new cultivation areas, which were incorporated into the current analysis (Fig 2). Plantations which were planted were grouped as "Plantation". Areas designated as a concession but being used for small-holder agriculture were grouped as "Small-plot agriculture". Concessions that showed a spectral signal of bare ground or recently burned, but not yet planted, were grouped as "Recently cleared", while those with indications of plantation infrastructure (such as drainage canals) but were still primarily covered with forest or scrubland were grouped as "Drained, not cleared". Lastly concessions that were provided in the MoEF dataset but, based on Landsat imagery, did not appear to have any oil palm plantation infrastructure were grouped as "Concession area not converted".

27

Remote sensing systems

TET-1 is based on an improved version of the BIRD (Bi-spectral Infrared Remote Detection) satellite structure and was launched July 2012, which together with the BIROS (Berlin InfraRed Optical System, launched June 2016) satellite will comprise the DLR FireBird mission. In addition to offering a testing platform for space technology through the DLR On-Orbit Verification program, TET-1 strives to provide better detection capabilities to quantitatively analyze HTEs such as active fires and volcanoes. TET-1 is a microsatellite, measuring 65 x 55 x 88 cm in size and weighing 120 kg, in a Low Earth Orbit (LEO) at circa 500 km altitude. Its orbit time is 90 minutes, translating to a revisit time of maximum 5 days at latitude 40° north, although given the satellite's off-nadir tilt and depending on location a target could be acquired on two consecutive days. The satellite is equipped with pushbroom sensors in the TIR (8.5–9.3 μm) and MWIR (3.4–4.2 μm), as well as three additional sensors in the VNIR (0.46–0.56 μm, 0.56–0.72 μm, 0.79–0.93 μm). Image swath width is 162 km for the TIR/MWIR bands and 202 km for the VNIR bands, and the ground sampling distance (GSD), or image pixel resolution, is on average 160 m. The onboard sensors not only enable the use of a bi-spectral method to provide subpixel fire radiative power estimates, the refined sensor sensitivity and a fine spatial resolution allow for improved detection and monitoring of a wider range of fires [43,48].

The MODIS (Moderate Resolution Imaging Spectroradiometer) instrument, onboard both the Terra and Aqua satellites, provides multispectral detection capabilities comprising 18 bands in the VNIR (0.41–1.38 μm), 10 bands in the SWIR/MWIR (1.64–7.32 μm) and 8 bands in the TIR (8.55–14.23 μm). The satellites are orbiting at 705 km, with Terra imaging at 10:30 am on its descending node and Aqua imaging at 1:30 pm on its ascending node. Each platform delivers daily coverage of the entire globe. Data are provided at spatial resolutions of 250 m (2 bands), 500 m (5 bands), and 1 km (29 bands). Since their launch in 1999 and 2002, both satellites have proved a valuable resource for monitoring the atmosphere [49], land cover [50,51], vegetation [52], snow coverage [53], sea ice [54,55], sea surface temperature [56,57], and ocean color [58–60]. The MODIS Active Fire Product [42] and Burned Area Product [61,62] have both been extensively used to monitor fire occurrence worldwide [12]. Most bands saturate at brightness temperatures of 330–400 K, with the exception of the 3.9 μm low-gain band (channel 21) which saturates at 500 K. Quantification of very large fire events is hindered by a low sensor saturation temperature [43], and while MODIS has until now offered the highest sensor saturation range, the 1 km pixel resolution still limits detection capabilities of small fires and fire dynamics. The Burned Area Product has known issues detecting fire activity in Central Kalimantan [63], resulting from the algorithm being based on a 16-day cloud-free mosaic which is difficult to obtain in the tropics [61]. The MODIS Burned Area Product was therefore not considered in this study. An initial comparison of the MODIS Active Fire Product (hotspots collection MCD14) and TET-1 imagery suggests that TET-1 can provide improved detection of small fire fronts (Fig 3a and 3b) as well as better signal detection through thick smoke and haze (Fig 3c and 3d).

The Landsat mission provides one of the longest continuous global imaging records available, covering from 1972 until present, and now delivers multispectral images in the VNIR, SWIR and TIR at a spatial resolution of 30 m. The current operational constellation consists of Landsat-7 ETM+ and Landsat-8 OLI, which when taken together provide a revisit time of 8 days. It should be noted that the Landsat-7 ETM+ dataset is reduced due to the Scan Line Corrector failure since 2003, which results in gaps of no data within images. Landsat satellite imagery has been used extensively for detecting area burned following a fire event, but such analyses can be hampered by heavy cloud and haze cover [34,64]. The recently launched European Space Agency (ESA) Sentinel-2A mission in June 2015 also provides fine resolution (down to

28
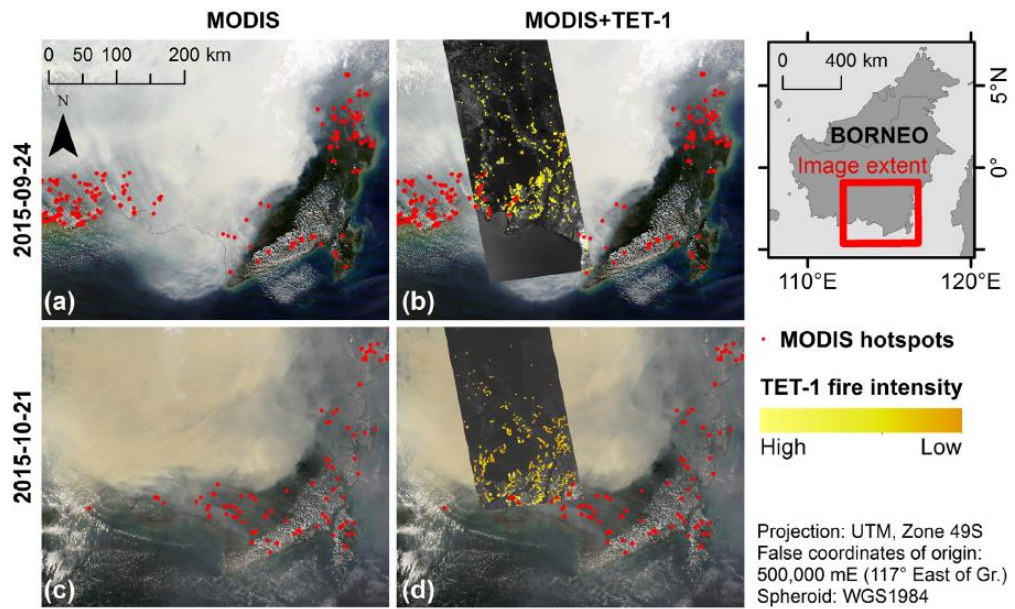
Fig 3. MODIS imagery and hotspot data compared with TET-1 imagery overlay. (a) MODIS Aqua true color (R, band 1 0.62–0.67 µm; G, band 4 0.55–0.57 µm; B, band 3 0.46–0.48 µm; source NASA) image from Sept. 24th, 2015, superimposed with same day MODIS hotspot data (red dots; source FIRMS collection MCD14). (b) The MODIS image overlaid with same day TET-1 gray-scale acquisition (source DLR FireBird Mission). MODIS hotspot data appear to under-detect low intensity fire fronts visible in TET-1 imagery (intensity of detected fire pixels indicated by yellow gradient). (c) MODIS imagery from Oct. 21st, 2015, superimposed with same day MODIS hotspot data. (d) The MODIS image overlaid with TET-1 imagery, which shows MODIS hotspot active fire detection being inhibited by thick smoke and haze.

doi:10.1371/journal.pone.0159410.g003

10 m), multispectral imagery in the VNIR and SWIR, and is expected to enable high quality analyses of land cover [65]. During the study period, Sentinel-2A provided a revisit time of 10 days over the study area. Both Landsat and Sentinel-2 images were considered to estimate change in burned area prior to and following the fire event. An overview of the all remote sensing datasets analyzed is provided in Table 1.

Satellite image processing

Taking into account both day and nighttime images, the TET-1 revisit time over the study area is between 2 and 3 days. At-sensor radiance images falling within the study area during the period of interest were supplied by the DLR Institute of Optical Sensor Systems in Berlin. Only the MWIR band was utilized in this study. Images did not always cover the full spatial extent of the study area. Further post-processing of images included image georeferencing to a Universal Transverse Mercator (UTM), zone 49 South, projection using ENVI 5.0 (Exelis Visual Information Solutions GmbH) and subsequent additional geocorrection in ArcMap 10.2.2 (ESRI Inc.).

MODIS hotspot data (MCD14) were accessed through the Fire Information for Resource Management System (FIRMS). To compare MODIS and FireBird sensor systems, hotspot data were post-processed to overlap temporally with the TET-1 imagery data, meaning data from

29

Table 1. Overview of Remote Sensing Image Data.

Sensor	Acquisition date	Image ID
TET-1	2015-09-24	FBI_TET1_20150924T051034_20150924T051134_L1B_C_EL
	2015-10-05	FBI_TET1_20151005T050624_20151005T050738_L1B_C_MH
	2015-10-13	FBI_TET1_20151013T051039_20151013T051153_L1B_C_EL
	2015-10-15	FBI_TET1_20151015T171847_20151015T171956_L1B_C_EL
	2015-10-18	FBI_TET1_20151018T170832_20151018T170941_L1B_C_EL
	2015-10-21	FBI_TET1_20151021T051425_20151021T051549_L1B_C_EL
	2015-10-23	FBI_TET1_20151023T172140_20151023T172259_L1B_C_EL
MODIS hotspots	2015-06-01 to 2015-12-31	MCD14
Landsat	2015-08-19	LC81180622015231LGN00
	2015-11-23	LC81180622015327LGN00
	2015-12-01	LE71180622015335EDC00
	2015-12-09	LC81180622015343LGN00
Sentinel-2A	2015-12-23	S2A_OPER_MSI_L1C_TL_SGS_20151223T061706
	2015-12-26	S2A_OPER_MSI_L1C_TL_SGS_20151226T094222

doi:10.1371/journal.pone.0159410.t001

days without TET-1 images were removed. Since on a given day TET-1 imagery did not always extend over the entire study area, the MODIS hotspot dataset was further clipped to ensure identical spatial coverage from both sensor datasets.

Relatively cloud and haze free ($<$ 60% cloud-coverage) Landsat images over the study area from the period June 2015 through January 2016 were accessed from the U.S. Geological Survey (USGS) GloVis server. Images from the Sentinel-2 mission were also considered, but only images with heavy cloud-coverage ($>$ 60%) over the study area from two months post fire event (November and December) were available and thus only used to qualitatively evaluate the Landsat burned area product. Both Landsat and Sentinel-2A images were atmospherically corrected using ATCOR-2/3 software (developed by Dr. Rudolf Richter, now licensed by ReSe Applications Schläpfer) [66].

Classification of active fires and burned areas

Hierarchical object-based image analysis (OBIA) is a recently developed technique that evaluates spectral band information combined with spatial context and pattern recognition algorithms [67]. This approach has been found to outperform traditional pixel-based classification methods when working with fine spatial resolution remote sensing imagery [68,69]. TET-1 and Landsat images were classified with eCognition software (Trimble Navigation Ltd.) using a hierarchical OBIA approach. To classify active fire pixels from TET-1 MWIR images, a ruleset was developed based on image-specific object values such as scene mean and standard deviation, mean difference to neighbors, abrupt boundary transition values and proximity to very bright objects. Water reflection pixels were removed based on a river+ocean mask produced from OpenStreetMaps (access date: Nov. 17th, 2015). An accuracy assessment was performed comparing the hierarchical OBIA results with a separate evaluation conducted by an independent analyzer. The assessment was based on a stratified random sampling scheme to control for the much lower coverage of fire pixels within an image, where 100 points were randomly assigned within each category (fire and non-fire, making a total of 200 assessment points per image), and an adjusted (weighted) error matrix was calculated based on area-normalized proportions [70,71].

Landsat images were used to classify recently burned areas both prior to and following the TET-1 imagery time series. A Landsat-8 OLI image from August 19th, 2015, with only 2%

30

cloud-coverage, was classified using an OBIA ruleset based on the Normalized Burn Ratio (NBR) and the product of a spectral unmixing analysis for recently burned areas, similar to methods developed by Hoscilo et al. [34] and Hoscilo et al. [72]. No clear images were available from November 2015 to January 2016 (46–58% cloud-coverage), and analysis was therefore limited to cloud and haze free areas within the image. Classification of recently burned areas from two separate Landsat-8 OLI images (Nov. 23rd and Dec. 9th, 2015) plus one Landsat-7 ETM+image (Dec. 1st, 2015) were combined to create a coverage estimate of recently burned areas. Areas of no data due to cloud coverage in all three images but clearly within a burn area, defined as being completely enclosed, were included in the post fire event classification. Despite these efforts, this method is likely underestimating the amount of recently burned area, spotlighting a limitation of Landsat imagery in capturing recently burned areas due to being dependent on cloud and haze free conditions.

Comparison of TET-1, MODIS hotspots and Landsat imagery

Active fire detection capabilities were compared between TET-1 imagery and MODIS hotspot data. Both datasets were spatially clipped to include the study area, and only hotspot data taken on days with TET-1 acquisitions were used. As mentioned, TET-1 imagery did not always completely cover the study area on a given day, which was controlled for in the MODIS hotspot data by subsetting both spatially and temporally.

The Landsat recently burned area classification was compared to a MODIS hotspot burned area estimate. Each MODIS hotspot was assumed to represent a square 1-km pixel. Downloaded MODIS hotspot data were reduced to overlap the same time period covering all Landsat images (2015-08-19 to 2015-12-09), then spatially clipped to the study area and dissolved to remove overlapping pixel areas.

AOI (Areas of Interest) selection and measuring fire front propagation speed

Fire AOI's were selected for further analysis dependent upon existence of a sufficient time series, defined as a series of active fire pixels from the TET-1 imagery covering at least three separate dates (see Fig 1). Areas were considered both within the Sebangau National Park as well as in neighboring degraded regions and oil palm plantation concessions. For each fire AOI, fire front propagation speed was measured by comparing the location of a fire front from one date to the next. Fire front propagation lines were placed so that they lay as perpendicular as possible to the advancing fire line and all notable fire propagation directions were being assessed. To obtain fire propagation speeds, the distance between fire fronts from one date to the next was divided by the number of intervening days.

Area burned within each fire AOI was quantified from the digitized TET-1 classification results as well as the Landsat classification results. When ground types were different within an AOI, the AOI was classified using the predominant ground (or vegetation) type covering the area. Within the AOI, each fire propagation line was classified based on the ground (or vegetation) type lying below the vector's middle point.

Results

TET-1 classification and comparison with other sensors

The accuracy assessment of the OBIA active fire analysis was found to have an adjusted overall accuracy of 93% or higher for each TET-1 image. In comparing active fire detection capabilities of TET-1 and MODIS (Table 2), the TET-1 data were clearly outperforming the hotspots data.

31

Table 2. Comparison MODIS and TET-1 Active Fire Detection.

Sensor	Revisit time (days)	Spatial resolution (m)	Detected active fire pixels	Estimated area (ha)	Percent study area
MODIS hotspots	0.5	1,000 x 1,000	1,090	109,000.00	4.5%
TET-1	2–3	160 x 160[a]	88,074	225,469.44	9.3%

[a]Ground resolution varied from 148 m to 169 m between images.

doi:10.1371/journal.pone.0159410.t002

Table 3. Comparison MODIS and Landsat Burned Area Detection Capabilities.

Sensor	Revisit time (days)	Spatial resolution (m)	Detected burned area pixels	Detected active fire pixels	Estimated burned area (ha)	Percent study area burned
MODIS hotspots[a]	0.5	1,000 x 1,000	N/A	13,225	496,124.68	20.4%
Landsat[b]	8	30 x 30	7,606,239	N/A	684,561.47	28.2%

N/A, detection method not applicable to the dataset.
[a]MODIS hotspot data cover the same period of time as the before and after Landsat images.
[b]Analysis based on comparison of detected burnt area from pre-fire (2015-08-19) to post-fire (2015-10-23, 12–01 and 12–09) images.

doi:10.1371/journal.pone.0159410.t003

During the time period of Sept. 24th to Oct. 23rd, the MODIS hotspot algorithm detected 1,090 active fire pixels when controlling for consistent spatial extent. This translates to an active fire area estimation of 109,000 ha. During the same time period, TET-1 detected 88,704 active fire pixels which translate to an active fire area estimation of 225,469.44 ha.

The Landsat recently burned area OBIA analysis, comparing changes from 2015-08-19 to 2015-12-09, resulted in a burned area estimate of 684,561.47 ha, while the MODIS hotspot algorithm, when controlling for concurrent spatial and temporal coverage, detected 13,225 active fire pixels and after being dissolved translated to an estimated burned area of 496,124.68 ha (Table 3). As mentioned previously, the Landsat images from November/December 2015 had between 40–60% cloud-coverage, which created areas of "No data due to cloud cover" within the final classification. Areas which were clearly enclosed by burned areas were included in the Landsat burned area estimate, amounting to 22,314.81 ha or 3.3% of the total estimate.

Fire front analysis and area burned within each AOI

Comparing TET-1 active fire pixels over successive dates revealed interesting differences in fire propagation dynamics. Ring fires were found to be either symmetric (Fig 4) or asymmetric (Fig 5). In both figures, the outer fire front from each TET-1 image within the time series is displayed as a colored fire isochrome with the respective image acquisition date indicated. Oftentimes fire ring propagation would begin by spreading symmetrically in all directions only to encounter areas where fire propagation would be either slowed or even remain stationary. Previous fire scars (pink/purplish areas) and changes in logging infrastructure (rails and canals) are evident from the Landsat imagery from 1991 and 2015 (Figs 4a, 4b and 5a, 5b). The TET-1 MWIR data from different points within the time series are also presented (Figs 4c–4f and 5c–5f). It is evident from both figures that fire propagation speed over previous fire scar areas is either greatly slowed or the fire becomes no longer detectable. Other reasons for reductions in fire propagation speeds, such as observed along the southern border of the Fig 4 fire or the eastern border of the Fig 5 fire, are likely due to differences in vegetation or ground type and are discussed in more detail below.

32
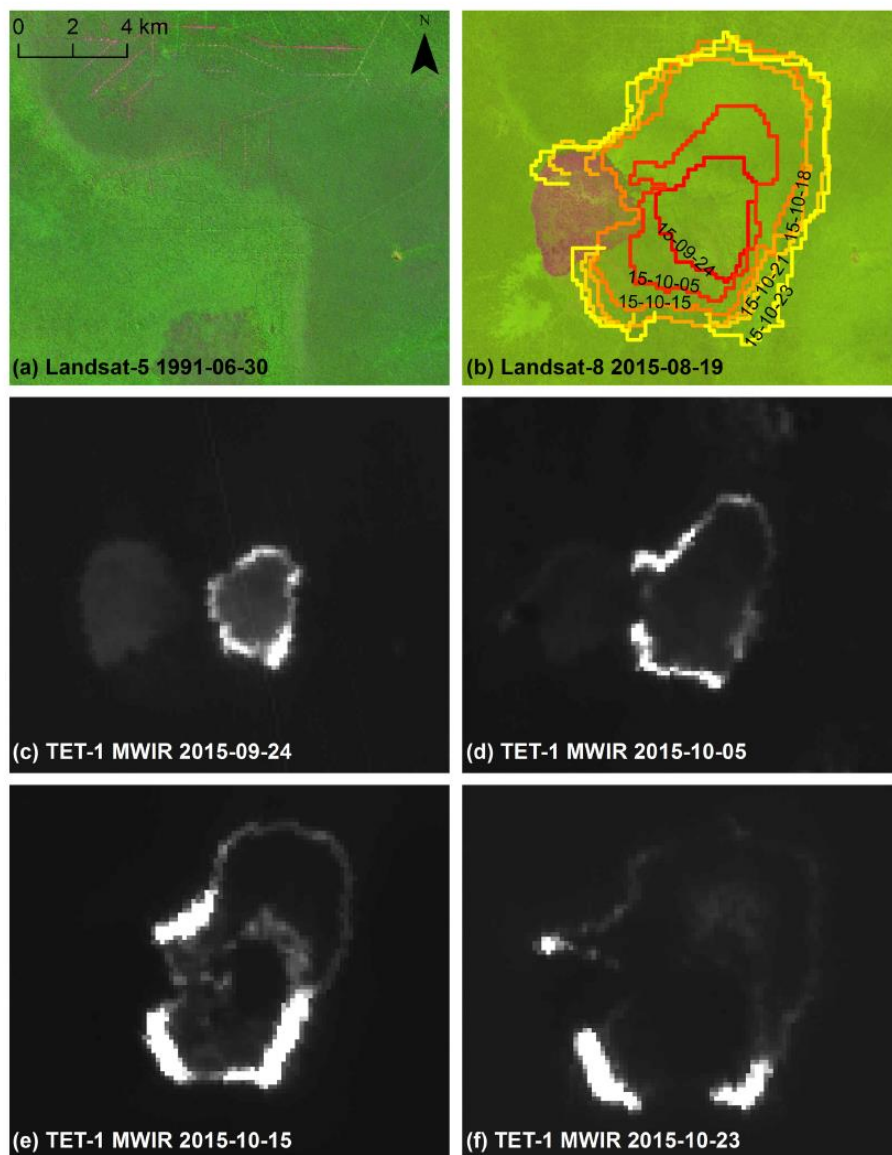
Fig 4. Symmetric ring fire front (F03) time series. (a) Landsat-5 TM imagery (false color: R, band 5 1.55–1.75 µm; B, band 4 0.76–0.90 µm; G, band 3 0.63–0.69 µm; source USGS/NASA) from June 30th, 1991, showing historical logging railway infrastructure and burn scars (purplish region) along southern image edge. (b) Landsat-8 OLI imagery (false color: R, band 9 1.36–1.38 µm; G, band 5 0.85–0.88 µm; B, band 4 0.64–0.67 µm; source USGS/NASA) from Aug. 19th, 2015, overlain with TET-1 detected fire front time series from six acquisition dates. Recently burned area prior to fire event is located along the western fire edge. Original TET-1 midwave infrared (MWIR; source DLR FireBird Mission) imagery is shown for (c) Sept. 24th, (d) Oct. 5th, (e) Oct. 15th, and (f) Oct. 23rd, 2015.

doi:10.1371/journal.pone.0159410.g004

33
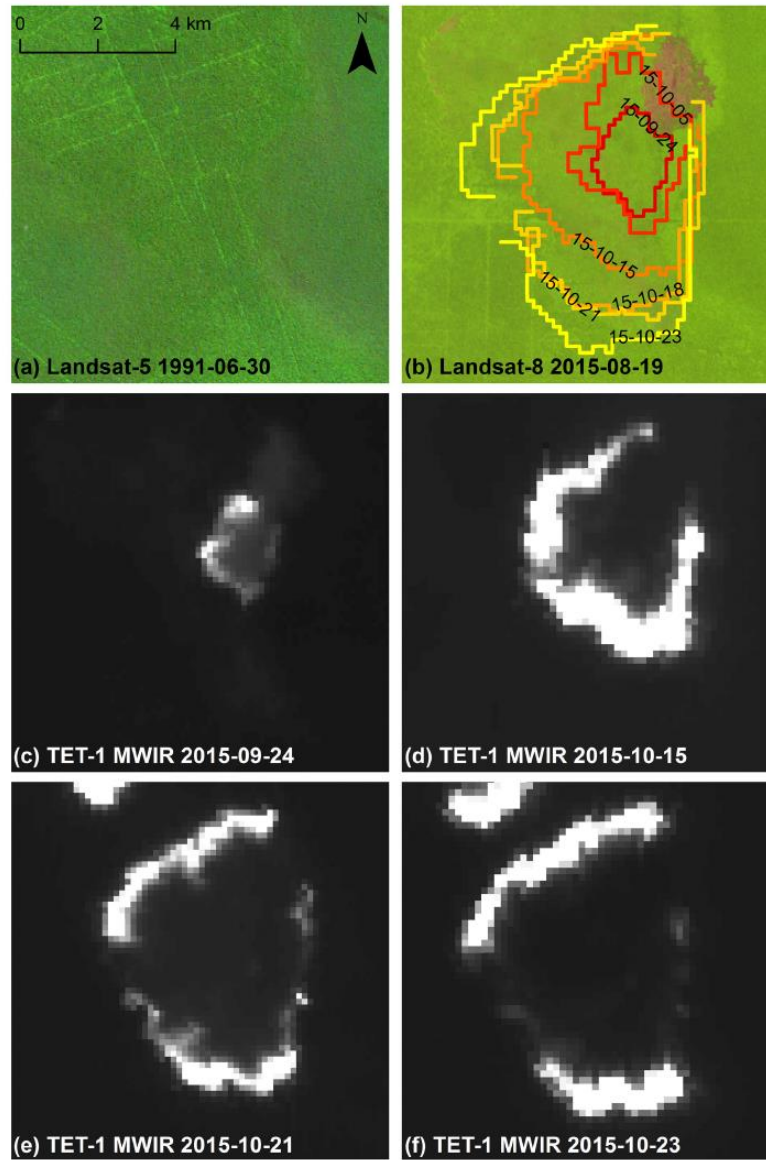
Fig 5. Asymmetric ring fire front (F02) time series. (a) Landsat-5 TM imagery (false color: R, band 5 1.55–1.75 µm; B, band 4 0.76–0.90 µm; G, band 3 0.63–0.69 µm; source USGS/NASA) from June 30th, 1991, showing historical logging railway infrastructure. (b) Landsat-8 OLI imagery (false color: R, band 9 1.36–1.38 µm; G, band 5 0.85–0.88 µm; B, band 4 0.64–0.67 µm; source USGS/NASA) from Aug. 19th, 2015, overlain with TET-1 detected fire front time series from six acquisition dates. Recently burned area prior to fire event is located along the northeastern fire edge. Original TET-1 midwave infrared (MWIR; source DLR FireBird Mission) imagery is shown for (c) Sept. 24th, (d) Oct. 15th, (e) Oct. 21st, and (f) Oct. 23rd, 2015.

doi:10.1371/journal.pone.0159410.g005

34

Table 4. Propagation Speed and Fire Dynamic Measurements.

Area ID	N	Fire form	Ground type	Vegetation type	Fire propagation speed (m/day)				TET-1 active fire area (ha)	Landsat burnt area (ha)
					Average	S.D.	Minimum	Maximum		
F01	3	Line P	peat 1–2 m	MS	141.17	122.86	4.09	442.67	860	1,305
F02	9	Ring AS	peat >2m	TI+LP	128.82	112.30	5.63	514.50	3,044	3,914
F03	12	Ring SY	peat >2m	TI+LP	166.35	141.03	26.91	765.50	5,093	6,415
F04	6	Ring SY	peat >2m	LP+MS	172.28	126.93	7.00	388.67	925	990
F05	7	Line M	peat+sand	LP+MS	128.96	134.23	4.62	490.00	3,309	9,308
F06	8	Line M	peat >2m	LP+MS	163.92	167.26	10.60	854.50	5,827	9,948
F07	8	Line M	peat >2m	LP+MS	223.16	327.32	35.89	1696.00	4,295	9,478
F08	5	Line P	peat+sand	LP+MS	141.79	125.03	29.62	488.50	1,632	3,447
F09	8	Line M	peat >2m	LP	191.85	257.57	16.52	1054.50	5,425	15,992
F10	4	Line P	peat 1–2 m	LP+MS	87.94	43.17	45.80	175.67	659	1,790
F11	4	Line P	peat 1–2 m	LP+MS	143.69	107.68	12.79	360.00	1,431	2,150
F12	4	Line P	peat+sand	LP+MS	204.81	229.67	17.33	978.50	2,027	2,931
F13	5	Line P	peat 1–2 m	LP+MS	191.64	178.20	38.63	533.00	1,738	5,611
F14	15	Line M	peat 1–2 m and >2m	LP+MS	207.50	330.64	8.14	1903.50	7,502	23,367
F15	4	Line M	peat >2m	C	139.59	166.14	5.21	503.50	1,961	4,070
F16	5	Line M	peat >2m	C	258.54	233.82	46.63	828.50	1,447	4,456

N, number of fire propagation time series lines measured per AOI; S.D., standard deviation; Line M, line fire front started from multiple sources; Line P, line fire front started from a point source; Ring SY, symmetrical ring fire form; Ring AS, asymmetrical ring fire form; MS, mixed swamp forest; LP, low pole forest; TI, tall interior forest; C, concession.

Fire propagation speed descriptive statistics for each AOI, along with active fire area estimates from TET-1 images and burned area estimates from Landsat images, are presented in Table 4. The highest fire propagation speeds measured were in excess of 500 m/day. One can see from the standard deviation and the spread between maximum to minimum measurements that fire propagation speed was highly variable over all areas. This variability is likely partially due to wind patterns and fuel load, both of which could not be integrated into this study. The most common fire form observed was a long fire line discerned to have started from either a single (6 AOIs in total) or multiple points (7 AOIs in total), the second most common form was a fire ring spreading from a central location (the remaining 3 AOIs). The predominant ground and vegetation type for each AOI is also indicated. The three highest averages (Area ID F07, F14, F16) as well as the three highest maximum fire propagation speeds (F07, F09, F14) were all measured over peat greater than 2 m deep. The three areas found to have burned the most (F06, F09, F14) all resulted from fire lines that appeared to have been started from multiple sources.

Fire propagation speed over different ground and vegetation types

Descriptive statistics showing the comparison of fire propagation speeds over different ground types is presented in Table 5. Differences in fire propagation speed between different ground types were not found to be statistically different (Mann-Whitney U-test or Wilcoxon Ranked-Sum Test, $p > 0.05$), although certain trends can be observed. The highest average and maximum fire propagation speeds occurred over peat greater than 2 m deep. Average fire propagation speed reduces successively as the peat layer depth decreases to a thin peat layer lying over sand.

35

Table 5. Fire Propagation Speeds over Peat and Sand Ground Types.

Ground type	Propagation speed (m/day)				
	N	Average	S.D.	Minimum	Maximum
peat+sand (depth unknown)	14	97.63	87.62	20.50	361.00
peat 0–1 m	30	134.94	131.90	4.62	490.00
peat 1–2 m	77	161.53	172.53	4.09	978.50
peat > 2m	202	187.01	237.82	5.21	1903.50

N, number of fire line measurements; S.D., standard deviation.

doi:10.1371/journal.pone.0159410.t005

Table 6. Fire Propagation Speeds over Different Vegetation Types.

Vegetation type	Propagation speed (m/day)				
	N	Average	S.D.	Minimum	Maximum
Planted plantation	5	125.99	146.43	14.76	415.00
Secondary swamp forest	199	185.72	243.34	4.09	1903.50
Swamp scrubland	118	151.12	145.46	5.21	828.50
Swamp (grass & sedge)	1	207.33	N/A	N/A	N/A

N, number of fire line measurements; S.D., standard deviation.

doi:10.1371/journal.pone.0159410.t006

Fire propagation speeds over various vegetation types is presented in Table 6. Differences were only tested for the vegetation classes which contained more than 10 fire line measurements (secondary swamp forest and swamp scrubland), but no significant differences were found (Mann-Whitney U-test or Wilcoxon Ranked-Sum test, $p > 0.05$). The slowest propagation speeds were observed in the planted plantation class. Although the quickest propagation speed was observed over the swamp land cover class, it should be noted that this class is represented by only a single measurement. The highest maximum propagation speed (1,903.50 m/day) was observed over previously unburned secondary swamp forest.

Fire prevalence in relation to different levels of concession usage

Occurrence of fire under different levels of concession usage is presented in Table 7. The two largest usage categories by area were "Plantation" and "Concession area not converted", and both these areas were also found to contain the highest active fire area estimates (5,297 ha and 1,717 ha respectively). By normalizing area coverage, accomplished by dividing the active fire

Table 7. Oil Palm Plantation Fire Occurrence.

Current status	Total parcels	Area (ha)	Number with HGU	TET-1 active fires (ha; % by area)		
				Inside	Border 160m	Within 500 m
Plantation	25	129,140	7	5,297; 4.1%	1,309; 1.0%	4,246; 3.3%
Small-plot agriculture	11	54,435	1[a]	1,717; 3.2%	82; 0.2%	300; 0.6%
Recently cleared	19	8,606	3	468; 5.4%	188; 2.2%	573; 6.7%
Drained, not cleared	7	1,994	0	270; 13.5%	173; 8.7%	652; 32.7%
Concession area not converted	10	77,703	1[a]	6,459; 8.3%	456; 0.6%	1,544; 2.0%

HGU, Cultivation Right on Land (Indonesian: Hak Guna Usaha).
[a]Plots granted with only local permits.

doi:10.1371/journal.pone.0159410.t007

36

area with the total area within a concession category, one observes that fires occurred most frequently in concession areas that are "Drained, not cleared" (13.5% within the area, 8.7% along the border, and 32.7% within 500 m of the border). Fires were found to occur least often in the small-holder agricultural areas (3.2%), and plantation areas (4.1%).

Discussion

Over the study period, TET-1 detection of active fire pixels consistently outperformed the MODIS hotspot algorithm. Even when accounting for differences in image pixel resolution (1 MODIS pixel is equivalent to circa 39 TET-1 pixels), the MODIS hotspot data detected less than half the active fires as compared with TET-1. These results are consistent with findings in other studies [43]. The MODIS hotspots burned area estimate, based on hotspot active fire detections converted to burned area, was also outperformed by the Landsat OBIA burned area analysis, which estimated 38% more newly burned area despite the data being of lower quality due to haze and cloud cover. The assumption that a MODIS hotspot point represents a complete square kilometer of burned area is tenuous and likely presents an overestimation of burned area detection. This only further supports the conclusion that Landsat should be the preferred passive detection system for burned area estimates following a fire event, however analyses of fire dynamics are very limited with this sensor given revisit time and cloud, haze and smoke coverage. Potential issues presented by comparing an algorithm detecting a dynamic process (such as active fire) with an algorithm detecting the product of a process (burned area) are discussed below. Fire detection issues with haze and cloud cover for both Landsat as well as MODIS are not unknown [34,64], and Fig 3 displays excellent examples of thick haze hampering the ability of the MODIS sensor to detect active fires. While MODIS, with a high saturation temperature of 500 K in one of the MWIR bands and global coverage every day, has been and continues to be the workhorse of global fire detection, the coarse 1-km spatial resolution detracts from the sensor's capability to capture small fire events and fronts [43]. The improved ability of the TET-1 sensor to capture these dynamics is displayed well in Fig 3b and 3d, where multiple smaller fire fronts are detected which were not present in the MODIS hotspot data.

TET-1 was intended primarily as an experimental satellite platform, and as such this study was conducted under certain limitations. An atmospheric correction of the MWIR band was not possible using ATCOR (pers. comm. R. Richter). Radiance in the MWIR spectrum is primarily affected by aerosols and water vapor in the atmosphere, and working with non-atmospherically corrected data most likely increases issues with false positive detection. We controlled for issues with sun glint from water and bright land cover types, such as bare soil with high quartz sand content, through utilization of a water mask and focusing analyses on TET-1 image time series that displayed similar patterns over 3 separate dates. Synergy of atmospherically corrected TIR and MWIR band data would enable better quantification of characteristics such as fire radiative power [43], and further research is currently being conducted to address the need for an appropriate atmospheric correction for data from this sensor. TET-1 has been joined in 2016 by BIROS, which will lower time between acquisition dates and provide an opportunity to reduce false positive detections through image comparison. Additionally, an operational bi-spectral method product based on the MWIR and TIR bands is in development, which will enable subpixel analysis of fire temperature and area. A measurement of fire temperature, an indicator of fire intensity, could enable earlier estimation of fire emissions from a particular area.

Derivation of burnt area estimates from active fire detection algorithms have been found to be prone to error [31], primarily due to available active fire detection systems producing only a

37

snapshot of a continuously moving fire front. Our estimates of actively burning area from TET-1 (225,469.44 ha) were not surprisingly much less than those from the burned area Landsat analysis (684,561.47 ha). Under the current FireBird satellite constellation, TET-1 acquisitions were only possible every 2–3 days. We often observed jumps in the detected fire pixels from one image to the next, which were assumed to be due to quickly spreading fire within that period of time. A similar trend appeared when comparing the AOI active-burning area detected by TET-1 with the newly burned area detected by Landsat (Table 4), where TET-1 was found to be underestimating the area by up to 69%. The two area estimation methods came the closest to one another for the F04 fire (925 ha and 990 ha respectively), which could be expected since it was a relatively small fire with few large jumps observed in the TET-1 time series. This issue will be lessened by expanding the FireBird constellation and thus shortening the period of time between image acquisitions, but it should be noted that products from algorithms for detecting active fires should be expected to be fundamentally different than algorithms for detecting burned area after a fire event.

Measured fire propagation speeds were highly variable both between and within different fire AOI's (Table 4), and the highest propagation speeds observed were in excess of 500 m/day. Average fire propagation speeds measured are on par with those estimated for cleared tropical rainforest (202 m/day) [73], but are much higher than estimates by Usup et al. [22] for peat fires in the same region (0.3–0.9 m/day). Distributions of the fire propagation speeds were highly skewed, as indicated by the median being often smaller than the arithmetic average, but even when considering only the median, a two orders of magnitude reduction in the propagation speed was not revealed. Possible causes for the propagation speed discrepancy could be the study by Usup et al. [22] being conducted during a less severe ENSO event, thus under different peat moisture content conditions, and over a different vegetation type than present in many AOI's analyzed in this study. The observed fire ring forms resemble those predicted by Usup et al. [22], where surface peat fire fronts move in an erratic pattern determined by distribution of favorable ignition conditions and can burn into deeper peat layers. Fire fronts were found to slow or even stop when encountering an area that had been recently burned (excellent examples can be observed around the pink/purple areas in Figs 4b and 5b). This is not surprising as aboveground biomass is reduced through fire, with tropical forest taking many decades to recover [74], thus the observed slowed propagation speed could be due to lower fuel availability.

No significant difference was found in fire propagation speed over unburned secondary swamp forest and swamp scrubland that burned sometime within the last 30 years. The MoEF land cover classification is based on 30 m x 30 m resolution Landsat data but created using a manual delineation approach that utilized a minimum mapping unit of 6.25 ha [44,75,76]. TET-1 pixels correspond to an area of 2.56 ha, thus the two datasets are within the same order of magnitude of one another. Despite this, these data are likely not detailed enough to sufficiently capture the relationship between different fuel loads available in various forest types such as tall interior, low pole and mixed swamp forest. Fire propagation lines were observed to slow when moving from tall interior peat swamp forest to low pole or mixed swamp forest. These forest types are evident in Fig 5a, where logging railways together with the bright-green textured area in the image center indicate tall interior forest containing valuable timber species. To the East of this area, low pole/mixed swamp forest is indicated through very little logging infrastructure and less green textured area. In Fig 5b, a seeming fire propagation boundary occurs along the same area as this forest type boundary. This can also be observed in Fig 4b along the northwestern and eastern edges of the F03 fire ring. The northern edge of this fire burned into an area appearing to be tall interior forest (logging infrastructure), but despite this the fire front quickly slows after 2 weeks of burning. Low pixel brightness temperature, a proxy for fire intensity, along these edges can be observed in the original TET-1 images (Fig 4d–4f),

38

and may be indicative that the fire is slowly spreading through the deeper peat layer. From the November/December Landsat images, this area appeared to still contain many patches of partial green, providing supporting evidence for a low intensity fire front. This, together with the fire front's persistence for more than 2 weeks, suggests that the deep peat layer had begun to slowly burn, but without ground truth measurements, a conclusive determination is outside the scope of this study.

It is interesting to note in Table 5 that fires propagating over peat+sand were never found to burn slower than 20 m/day. The minimum propagation speeds in the other ground type categories (peat depths 0–1 m, 1–2 m, and > 2 m) were higher than those found by Usup et al. [22], although are closer to peat fire propagation speeds measured in Russia (2.4 m/day) [77] and Canada (2.9 m/day) [78]. Quickly spreading surface peat fires were likely mixed with deeper peat fires for each category during the analysis, which together with factors such as differing fuel availability and weather conditions, could explain the large variation in the data. The analysis was limited to what is possible to measure using a remote sensing system and there is a dire need to build upon the work of Usup et al. [22] in order to provide further *in situ* measurements of peat fire propagation speeds in Central Kalimantan over different ground and vegetation types.

Another potentially important factor not included in the analyses was water table level, as peat with low moisture content has a much higher risk of catching on fire [22]. Conservation efforts within the Sebangau National Park have included installing dams to help slow run-off and thus retain more water in the peat swamp forest [45]. Whether these dams have a dampening effect on fire dynamics could be observed during the 2015 fires (Fig 6). Three different fire fronts were measured (F10, F11, and F12), one of which had the lowest average fire propagation speed measured (F10, 87.94 m/day, see Table 4). The F10 and F11 fires occurred over peat > 2m deep, and the slow propagation speed of the F10 fire is likely due to the deeper peat layer catching fire. The F11 fire appears to be a quick-moving surface peat fire front. Installed WWF dam locations are also presented in Fig 6. It can be observed that the East and West boundaries of the F10 and F11 fires correspond to dam installation locations, while the central portions of these fires contain little to no dams. The F12 fire occurred over thin peat covering a quartz sand layer (peat+sand). From the fire front time series, this fire appears to have begun as a quick-moving surface fire and then slowing (similar to the F10 fire). The centrally located dams for the F12 fire did not appear to have the same dampening effect observed for the F11 and F10 fire. This may be due to the shallowly located sand layer, which presents different groundwater porosity conditions than peat. The TET-1 data alone can simply offer qualitative observations on dam effectiveness, and conclusions should only be made after extensive *in situ* sampling, but the opportunity to use observed fire dynamics to focus successful field campaign efforts post-fire event can be highlighted by this example.

From the analysis of fire occurrence in different concession areas (Table 7), it is evident that fires occur most often in plots with installed drainage infrastructure but have not yet been cleared. Since fire is the technique of choice to quickly and cheaply clear slashed areas [27], the frequent occurrence of fire within the "Drained, not cleared" areas is not surprising. This concession class also had the highest percentage of fire occurrence along its borders and within 500 m thereof, supporting the hypothesis that most peat swamp fires originate from anthropogenic sources [18]. Interestingly enough, small-plot agriculture areas had some of the lowest percentages of fire occurrence. Fires were often first detected in previously burned areas which then spread into surrounding primary forest. Indonesia has a long history with oil palm plantation management [18], including actions to control concession growth through a moratorium upon issuing new licenses in 2011 [79]. Low-intensity peatland fires can contribute heavily to emissions [29,78,80], and reducing their occurrence as well as their size will play an important factor in Indonesia's plan to reduce emissions 26% by 2020.

39
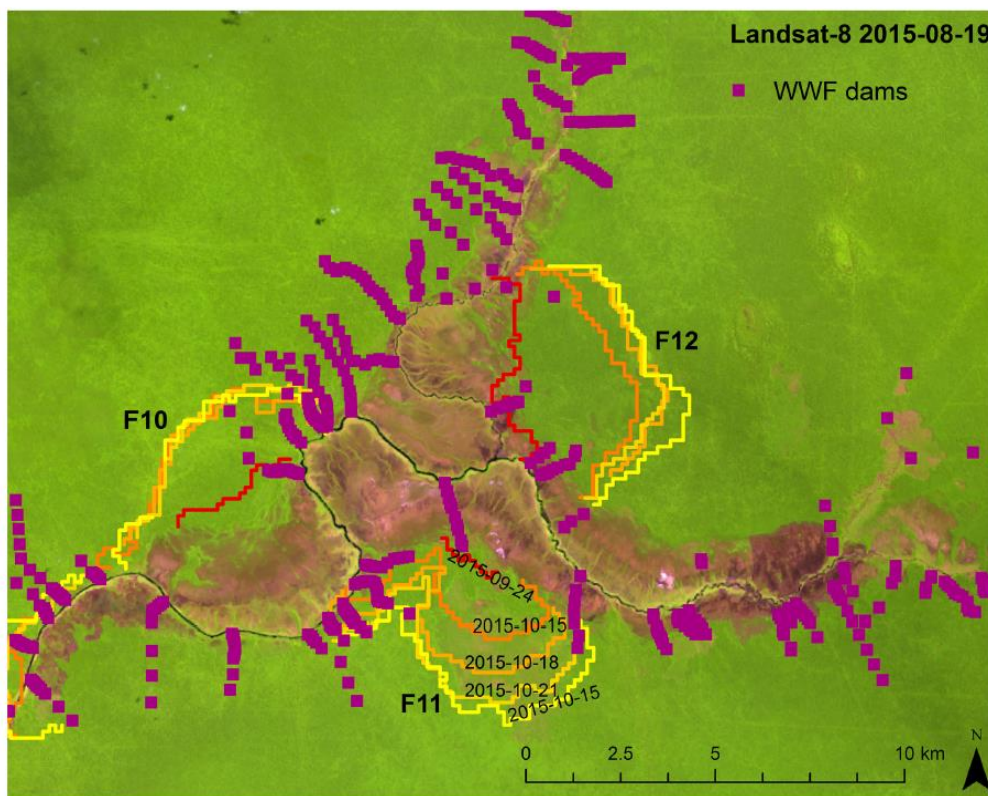
Fig 6. Fire front dynamics of AOI F10, F11 and F12 in relation to installed dams. Landsat-8 OLI imagery (false color: R, band 9 1.36–1.38 μm; G, band 5 0.85–0.88 μm; B, band 4 0.64–0.67 μm; source USGS/NASA) from Aug. 19th, 2015, overlain with TET-1 detected fire front time series from six acquisition dates. Location of dam installations shown by purple squares.

doi:10.1371/journal.pone.0159410.g006

Efficient and effective fire management is difficult on many levels [6], and a key component for improvement will depend upon the best fire occurrence monitoring system possible. Early detection of small fires, before they have the chance to become fire fronts many kilometers long, will greatly improve firefighting response efficiency. Fig 7 shows a TET-1 image series as fires first detected on Sept. 24th, 2015, thereafter spread and connect with one another over the following 2 weeks to become fire fronts over 10 km long. Relying solely upon the MODIS hot-spot data, one would have missed detection of the small fires in September. The hotspot dataset then detects less than half of all fires in the October image. The image displays the F06, F07 and F09 fires, which were estimated to have burned an area ranging from 15,547 ha (using TET-1) to 35,417 ha (using Landsat). The most common fire form observed over the entire study area were fire lines (13 out of 16 fires examined), all of which either started as a single point source or from multiple sources. This emphasizes how early detection of small fires before they have the chance to grow into large fire fronts will be very important for improving fire management efficiency as well as effectiveness.

40
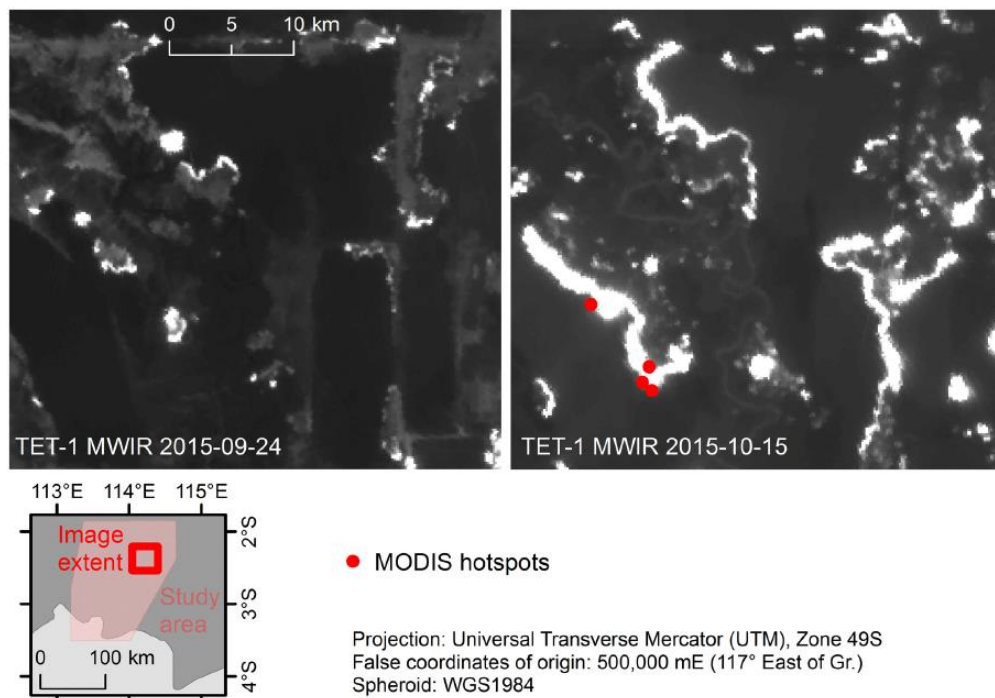
Fig 7. Rapid fire front growth during 2 weeks and comparing MODIS hotspot fire detection with TET-1. TET-1 midwave infrared (MWIR; source DLR FireBird Mission) images from Sept. 24th and Oct. 15th, 2015. Location of image extent within study area indicated in the inset. MODIS hotspot data for date concurrent to TET-1 imagery indicated in each image (red dots; source FIRMS collection MCD14).

doi:10.1371/journal.pone.0159410.g007

Conclusions

This study demonstrates the improved fire detection capabilities of TET-1 compared to commonly accepted fire monitoring systems, and how this sensor allows better measurement of temporal and spatial fire dynamics than heretofore possible. TET-1 fire detection capabilities, given the sensor's higher saturation temperature and finer spatial resolution, are clearly enhanced compared to those of the MODIS system. The MODIS hotspot data have and will continue to provide valuable information on global fire occurrence, playing a very important role in global monitoring of fire activity and analyses of decadal changes in fire occurrence. The FireBird mission offers an opportunity to build upon this system with a more sensitive fire monitoring system capable of providing more detailed, locally-based information on fire occurrence and previously not possible fire dynamic measurements. Early fire detection through smoke and haze provides valuable information for fire control management. The costs incurred, both financial as well as social, by the fall 2015 fire catastrophe present clear motives for improving current fire control management systems.

Another goal of this study was to provide a first estimate of the damage incurred to the Sebangau National Park during this event. Our calculations of active fire and area burned within the study area range between 225,469.44 ha (TET-1) and 684,561.47 ha (Landsat).

41

This discrepancy is due to differences in detection methodology, where TET-1 is providing snapshots of active fires while Landsat is providing a combined estimate of where fires burned. Both systems used in synergy with one another would support a monitoring system capable of accurately estimating area burned as well as measuring fire dynamics closer to real-time than previously possible. Monitoring of fire damage extent using sensors working in the VNIR and SWIR, such as those used in the Landsat and recently joining Sentinel-2 missions, provide estimates of burned area at fine spatial resolution (down to 10 m) but are limited by the requirement of waiting for relatively cloud and haze free images [34,64]. The longer the period of time between a fire event and acquisition of a clear image, the more vegetation regrowth and resettlement inhibits accurate detection of burn scars [64]. Fire dynamic measurements revealed maximum propagation speeds in excess of 500 m/day and that fires tended to spread most quickly over peat > 2m deep. Based on peat fire propagation speeds measured in other regions, we conclude that this group was likely a mix of quick-moving surface peat fire fronts and slow-burning, low intensity sub-surface peat fires. Changes in vegetation type were observed to co-occur with fire spreading boundaries. We also found that fires occurred with the highest frequency in concession areas containing drainage infrastructure but were not yet cleared prior to the fire event. Fires were observed to often begin in areas previously burned and then spread into neighboring primary forest. While these observations were statistically inconclusive, this demonstrates how the TET-1 sensor offers a wealth of data for further fire dynamic investigations. Conservation efforts, such as the installation of dams, likely helped to minimize spread of fire in some areas, but enhanced fire monitoring systems would provide an integral tool for improving firefighting management.

TET-1 has been joined in 2016 by BIROS, expanding the FireBird constellation and thus reducing time between acquisition dates. Issues with determining burned area from active fire detection data, where fast-moving fire fronts produce a discontinuous time series of events, will be lessened through decreasing the time period between detection events. Future expansion of the FireBird fleet is in discussion, which would enable near real-time fire detection. This would support firefighting activity organization through focusing efforts on fires while they are still small and more easily contained. In this study we have demonstrated not only how a FireBird sensor can improve hereto existing monitoring systems, but also how detected fire dynamic data can be used to help design measures to reduce risk of fire. This information will be useful for government agencies, fire managers and monitoring groups concerned with preventing such catastrophes in the future.

Acknowledgments

Author Contributions

Conceived and designed the experiments: SE FS ECA. Performed the experiments: ECA WW. Analyzed the data: ECA SE. Contributed reagents/materials/analysis tools: EL WH ECA SE WW. Wrote the paper: ECA SE FS EL.

42

References

1. World Bank. Indonesia economic quarterly: Reforming amid uncertainty; December 2015. Available: http://pubdocs.worldbank.org/pubdocs/publicdoc/2015/12/844171450085661051/IEQ-DEC-2015-ENG.pdf.

2. Atwood SA, Reid JS, Kreidenweis SM, Yu LE, Salinas SV, Chew BN, et al. Analysis of source regions for smoke events in Singapore for the 2009 El Nino burning season. Atmos Environ. 2013; 78: 219–230. doi: 10.1016/j.atmosenv.2013.04.047

3. Hyer EJ, Chew BN. Aerosol transport model evaluation of an extreme smoke episode in Southeast Asia. Atmos Environ. 2010; 44: 1422–1427. doi: 10.1016/j.atmosenv.2010.01.043

4. Reddington CL, Yoshioka M, Balasubramanian R, Ridley D, Toh YY, Arnold SR, et al. Contribution of vegetation and peat fires to particulate air pollution in Southeast Asia. Environ Res Lett. 2014; 9: 94006. doi: 10.1088/1748-9326/9/9/094006

5. Goh K, Schwela D, Goldammer JG, Simpson O. Health Guidelines for Vegetation Fire Events. Background papers; 1999. Available: http://www.preventionweb.net/files/1905_VL206106.pdf.

6. Barber CV, Schweithelm J. Trial by fire: Forest fires and forestry policy in Indonesia's era of crisis and reform. Washington, D.C.: World Resources Institute Forest Frontiers Initiative in collaboration with WWF-Indonesia & Telapak Indonesia Foundation; 2000.

7. Kunii O, Kanagawa S, Yajima I, Himatsu Y, Yamamura S, Amagi T, et al. The 1997 haze disaster in Indonesia: Its air quality and health effects. Arch Environ Occup Health. 2002; 57: 16–22.

8. Rieley JO, Siefermann RG, Page SE. The origin, development, present status and importance of the lowland peat swamp forests of Borneo. Suo. 1992; 43: 241–244.

9. Posa MRC, Wijedasa LS, Corlett RT. Biodiversity and conservation of tropicalpeat swamp forests. BioScience. 2011; 61: 49–57.

10. Cochrane MA, Schulze MD. Fire as a recurrent event in tropical forests of the eastern Amazon: Effects on forest structure, biomass, and species composition. Biotropica. 1999; 31: 2–16.

11. Mansourian S, Vallauri D, Dudley N, editors. Local participation, livelihood needs, and institutional arrangements: Three keys to sustainable rehabilitation of degraded tropical forest Lands. In: Forest restoration in landscapes. New York, USA: Springer; 2005.

12. van der Werf GR, Randerson JT, Giglio L, Collatz GJ, Mu M, Kasibhatla PS, et al. Global fire emissions and the contribution of deforestation, savanna, forest, agricultural, and peat fires (1997–2009). Atmos Chem Phys. 2010; 10: 11707–11735. doi: 10.5194/acp-10-11707-2010

13. van der Werf, Guido R. Indonesian fire season progression; 2015. Available: http://www.globalfiredata.org/updates.html.

14. Page SE, Rieley JO, Banks CJ. Global and regional importance of the tropical peatland carbon pool. Glob Change Biol. 2011; 17: 798–818. doi: 10.1111/j.1365-2486.2010.02279.x

15. Immirzi CP, Maltby E. The global status ofpeatlands and their role in the carbon cycle. Wetlands Ecosystems Research Group, Report 11. Exeter, UK: University of Exeter; 1992.

16. Page SE, Rieley JO, Shotyk W, Weiss D. Interdependence of peat and vegetation in a tropical peat swamp forest. Philos Trans R Soc Lond B Biol Sci. 1999; 354: 1885–1897. doi: 10.1098/rstb.1999.0529 PMID: 11605630

17. Miettinen J, Shi C, Liew SC. Deforestation rates in insular Southeast Asia between 2000 and 2010. Glob Change Biol. 2011; 17: 2261–2270. doi: 10.1111/j.1365-2486.2011.02398.x

18. Marlier ME, DeFries RS, Kim PS, Koplitz SN, Jacob DJ, Mickley LJ, et al. Fire emissions and regional air quality impacts from fires in oil palm, timber, and logging concessions in Indonesia. Environ Res Lett. 2015; 10: 85005. doi: 10.1088/1748-9326/10/8/085005

19. Miettinen J, Hooijer A, Shi C, Tollenaar D, Vernimmen R, Liew SC, et al. Extent of industrial plantations on Southeast Asian peatlands in 2010 with analysis of historical expansion and future projections. Glob Change Biol Bioenergy. 2012; 4: 908–918. doi: 10.1111/j.1757-1707.2012.01172.x

20. Muhamad NZ, Rieley JO. Management of tropical peatlands in Indonesia. In: Rieley JO, Page SE, editors. Peatlands for people, natural resources function and sustainable management: Proceedings of the international symposium on tropical peatlands; 2002. pp. 155–162.

21. Konecny K, Ballhorn U, Navratil P, Jubanski J, Page SE, Tansey K, et al. Variable carbon losses from recurrent fires in drained tropical peatlands. Glob Change Biol. 2015. doi: 10.1111/gcb.13186

22. Usup A, Hashimoto Y, Takahashi H, Hayasaka H. Combustion and thermal characteristics of peat fire in tropical peatland in Central Kalimantan, Indonesia. Tropics. 2004; 14: 1–19. doi: 10.3759/tropics.14.1

23. Takahashi H, Shimada S, Ibie BF, Usup A, Yudha, Limin SH. Annual changes of water balance and a drought index in a tropical peat swamp forest of Central Kalimantan, Indonesia. In: Rieley JO, Page SE,

43

editors. Peatlands for people, natural resources function and sustainable management: Proceedings of the international symposium on tropical peatlands; 2002. pp. 63–67.

24. Goldammer JG. History of equatorial vegetation fires and fire research in Southeast Asia before the 1997–98 episode: A reconstruction of creeping environmental changes. Mitig Adapt Strat Glob Change. 2006; 12: 13–32. doi: 10.1007/s11027-006-9044-7

25. Siegert F, Ruecker G, Hinrichs A, Hoffmann AA. Increased damage from fires in logged forests during droughts caused by El Niño. Nat. 2001; 414: 437–440. doi: 10.1038/35106547

26. Page S, Hoscilo A, Langner A, Tansey K, Siegert F, Limin S, et al. Tropical peatland fires in Southeast Asia. In: Cochrane MA, editor. Tropical fire ecology: Climate change, land use, and ecosystem dynamics. Berlin, Germany: Springer; 2009. pp. 263–287.

27. Simorangkir D. Fire use: Is it really the cheaper land preparation method for large-scale plantations. Mitig Adapt Strat Glob Change. 2006; 12: 147–164. doi: 10.1007/s11027-006-9049-2

28. Ballhorn U, Siegert F, Mason M, Limin S. Derivation of burn scar depths and estimation of carbon emissions with LIDAR in Indonesian peatlands. P Natl Acad Sci USA. 2009; 106: 21213–21218. doi: 10.1073/pnas.0906457106

29. Muraleedharan TR, Radojevic M, Waugh A, Caruana A. Emission from the combustion of peat: An experimental study. Atmos Environ. 2000; 34: 3033–3055.

30. Taylor D. Biomass burning, humans and climate change in Southeast Asia. Biodivers Conserv. 2010; 19: 1025–1042. doi: 10.1007/s10531-009-9756-6

31. Stolle F, Dennis RA, Kurniwan I, Lambin EF. Evaluation of remote sensing-based active fire datasets in Indonesia. Int J Remote Sens. 2004; 25: 471–479. doi: 10.1080/01431160310001618022

32. Robinson JM. Fire from space: Global fire evaluation using infrared remote sensing. Int J Remote Sens. 1991; 12: 3–24. doi: 10.1080/01431169108929628

33. Fuller DO. Satellite remote sensing of biomass burning with optical and thermal sensors. Prog Phys Geogr. 2000; 24: 543–561. doi: 10.1177/030913330002400404

34. Hoscilo A, Page SE, Tansey KJ, Rieley JO. Effect of repeated fires on land-cover change on peatland in southern Central Kalimantan, Indonesia, from 1973 to 2005. Int J Wildland Fire. 2011; 20: 578. doi: 10.1071/WF10029

35. Li Z, Kaufman YJ, Ichoku C, Fraser R, Trishchenko A, Giglio L, et al. A review of AVHRR-based active fire detection algorithms: Principles, limitations, and recommendations. In: Ahern FJ, editor. Global and regional vegetation fire monitoring from space: Planning a coordinated international effort. Hague, the Netherlands: SPB Academic Pub; 2001. pp. 199–225.

36. Li Z, Nadon S, Cihlar J. Satellite-based detection of Canadian boreal forest fires: Development and application of the algorithm. Int J Remote Sens. 2000; 21: 3057–3069.

37. Giglio L, Kendall JD, Justice CO. Evaluation of global fire detection algorithms using simulated AVHRR infrared data. Int J Remote Sens. 1999; 20: 1947–1985.

38. Prins EM, Menzel WP. Trends in South American biomass burning detected with the GOES visible infrared spin scan radiometer atmospheric sounder from 1983 to 1991. J Geophys Res. 1994; 99: 16719. doi: 10.1029/94JD01208

39. Arino O, Rosaz JM, Goloup P. The ATSR World Fire Atlas and a synergy with POLDER aerosol products. Available: http://earth.esa.int/workshops/atsr_workshop_1999/Papers/Arino.pdf.

40. Mota BW, Pereira JMC, Oom D, Vasconcelos MJP, Schultz M. Screening the ESA ATSR-2 World Fire Atlas (1997–2002). Atmos Chem Phys. 2006; 6: 1409–1424. doi: 10.5194/acp-6-1409-2006

41. Giglio L, Justice CO. Effect of wavelength selection on characterization of fire size and temperature. Int J Remote Sens. 2003; 24: 3515–3520. doi: 10.1080/0143116031000017056

42. Giglio L, Descloitres J, Justice CO, Kaufman YJ. An Enhanced Contextual Fire Detection Algorithm for MODIS. Remote Sens Environ. 2003; 87: 273–282. doi: 10.1016/S0034-4257(03)00184-6

43. Zhukov B, Lorenz E, Oertel D, Wooster M, Roberts G. Spaceborne detection and characterization of fires during the bi-spectral infrared detection (BIRD) experimental small satellite mission (2001–2004). Remote Sens Environ. 2006; 100: 29–51. doi: 10.1016/j.rse.2005.09.019

44. Margono BA, Potapov PV, Turubanova S, Stolle F, Hansen MC. Primary forest cover loss in Indonesia over 2000–2012. Nat Clim Chang. 2014; 4: 730–735.

45. WWF-Indonesia Sebangau Project. Rewetting of tropical peat swamp forest in Sebangau National Park, Central Kalimantan, Indonesia; 22 July 2014. Available: https://s3.amazonaws.com/CCBA/Projects/Rewetting_of_Tropical_Peat_Swamp_Forest_in_Sebangan_National_Park/SNP+Peat+Rewettting+Project+-+CCB+PDD+-+V01.pdf.pdf.

46. Global Forest Watch; 2014. Available: http://www.globalforestwatch.org. Accessed 29 February 2016.

44

47. Greenpeace; 2016. Available: http://www.greenpeace.org/seasia/id/Global/seasia/Indonesia/Code/Forest-Map/en/data.html. Accessed 14 March 2016.

48. Zhukov B, Briess K, Lorenz E, Oertel D, Skrbek W. Detection and analysis of high-temperature events in the BIRD mission. Acta Astronaut. 2005; 56: 65–71. doi: 10.1016/j.actaastro.2004.09.014

49. Remer LA, Kaufman YJ, Tanre D, Mattoo S, Chu DA, Martins JV, et al. The MODIS aerosol algorithm, products, and validation. J Atmos Sci. 2005; 62: 947–973.

50. Friedl MA, McIver DK, Hodges J, Zhang XY, Muchoney D, Strahler AH, et al. Global land cover mapping from MODIS: Algorithms and early results. Remote Sens Environ. 2002; 83: 287–302.

51. Friedl MA, Sulla-Menashe D, Tan B, Schneider A, Ramankutty N, Sibley A, et al. MODIS Collection 5 global land cover: Algorithm refinements and characterization of new datasets. Remote Sens Environ. 2010; 114: 168–182. doi: 10.1016/j.rse.2009.08.016

52. Huete A, Didan K, Miura T, Rodriguez E, Gao X, Ferreira L. Overview of the radiometric and biophysical performance of the MODIS vegetation indices. Remote Sens Environ. 2002; 83: 195–213. doi: 10.1016/S0034-4257(02)00096-2

53. Hall DK, Riggs GA, Salomonson VV, DiGirolamo NE, Bayr KJ. MODIS snow-cover products. Remote Sens Environ. 2002; 83: 181–194. doi: 10.1016/S0034-4257(02)00095-0

54. Box JE, Bromwich DH, Veenhuis BA, Bai L, Stroeve JC, Rogers J, et al. Greenland ice sheet surface mass balance variability (1988–2004) from calibrated polar MM5 output. J Clim. 2006; 19: 2783–2800.

55. Scambos TA, Haran TM, Fahnestock MA, Painter TH, Bohlander J. MODIS-based Mosaic of Antarctica (MOA) data sets: Continent-wide surface morphology and snow grain size. Remote Sens Environ. 2007; 111: 242–257. doi: 10.1016/j.rse.2006.12.020

56. Haines SL, Jedlovec GJ, Lazarus SM. A MODIS sea surface temperature composite for regional applications. IEEE T Geosci Remote. 2007; 45: 2919–2927. doi: 10.1109/tgrs.2007.898274

57. Kilpatrick KA, Podestá GP, Evans R. Overview of the NOAA/NASA advanced very high resolution radiometer Pathfinder algorithm for sea surface temperature and associated matchup database. J Geophys Res-Oceans. 2001; 106: 9179–9197. doi: 10.1029/1999JC000065

58. Gitelson AA, Dall'Olmo G, Moses W, Rundquist DC, Barrow T, Fisher TR, et al. A simple semi-analytical model for remote estimation of chlorophyll-a in turbid waters: Validation. Remote Sens Environ. 2008; 112: 3582–3593. doi: 10.1016/j.rse.2008.04.015

59. Hu C, Chen Z, Clayton TD, Swarzenski P, Brock JC, Muller–Karger FE. Assessment of estuarine water-quality indicators using MODIS medium-resolution bands: Initial results from Tampa Bay, FL. Remote Sens Environ. 2004; 93: 423–441. doi: 10.1016/j.rse.2004.08.007

60. Miller RL, McKee BA. Using MODIS Terra 250 m imagery to map concentrations of total suspended matter in coastal waters. Remote Sens Environ. 2004; 93: 259–266. doi: 10.1016/j.rse.2004.07.012

61. Roy DP, Boschetti L, Justice CO, Ju J. The collection 5 MODIS burned area product—Global evaluation by comparison with the MODIS active fire product. Remote Sens Environ. 2008; 112: 3690–3707. doi: 10.1016/j.rse.2008.05.013

62. Roy DP, Jin Y, Lewis PE, Justice CO. Prototyping a global algorithm for systematic fire-affected area mapping using MODIS time series data. Remote Sens Environ. 2005; 97: 137–162. doi: 10.1016/j.rse.2005.04.007

63. Spessa AC, Field RD, Pappenberger F, Langner A, Englhart S, Weber U, et al. Seasonal forecasting of fire over Kalimantan, Indonesia. Nat Hazards Earth Sys. 2015; 15: 429–442. doi: 10.5194/nhess-15-429-2015

64. Siegert F, Hoffmann AA. The 1998 forest fires in East Kalimantan (Indonesia): A quantitative evaluation using high resolution, multitemporal ERS-2 SAR images and NOAA-AVHRR hotspot data. Remote Sens Environ. 2000; 72: 64–77.

65. Drusch M, Del Bello U, Carlier S, Colin O, Fernandez V, Gascon F, et al. Sentinel-2: ESA's optical high-resolution mission for GMES Operational Services. Remote Sens Environ. 2012; 120: 25–36. doi: 10.1016/j.rse.2011.11.026

66. Richter R.; 2014. Available: https://www.rese-apps.com/software/atcor/index.html.

67. Schiewe J, Tufte L, Ehlers M. Potential and problems of multi-scale segmentation methods in remote sensing. GIS—Zeitschrift für Geoinformationssysteme. Heidelberg, Germany: Hüthig GmbH & Co. KG; 6/2001. pp. 34–39.

68. Blaschke T. Object based image analysis for remote sensing. ISPRS J Photogramm Remote Sens. 2010; 65: 2–16. doi: 10.1016/j.isprsjprs.2009.06.004

69. Blaschke T, Strobl J. What's wrong with pixels? Some recent developments interfacing remote sensing and GIS. GIS—Zeitschrift für Geoinformationssysteme. Heidelberg, Germany: Hüthig GmbH & Co. KG; 6/2001. pp. 12–17.

45

70. Card DH. Using known map category marginal frequencies to improve estimates of thematic map accuracy. Photogramm Eng Remote Sensing. 1982; 48: 431–439.

71. Mas J, Pérez-Vega A, Ghilardi A, Martínez S, Loya-Carrillo JO, Vega E. A suite of tools for assessing thematic map accuracy. Geogr J. 2014; Article ID 372349: 1–10. doi: 10.1155/2014/372349

72. Hoscilo A, Tansey KJ, Page SE. Post-fire vegetation response as a proxy to quantify the magnitude of burn severity in tropical peatland. Int J Remote Sens. 2013; 34: 412–433. doi: 10.1080/01431161. 2012.709328

73. Carvalho JA Jr, Gurgel Veras CA, Alvarado EC, Sandberg DV, Leite SJ, Gielow R, et al. Understorey fire propagation and tree mortality on adjacent areas to an Amazonian deforestation fire. Int J Wildland Fire. 2010; 19: 795. doi: 10.1071/WF08047

74. d'Oliveira M, Alvarado EC, Santos JC, Carvalho JA. Forest natural regeneration and biomass production after slash and burn in a seasonally dry forest in the Southern Brazilian Amazon. For Ecol Manage. 2011; 261: 1490–1498. doi: 10.1016/j.foreco.2011.01.014

75. Wijaya A, Sugardiman Budiharto RA, Tosiani A, Murdiyarso D, Verchot LV, editors. Assessment of Large Scale Land Cover Change Classifications and Drivers of Deforestation in Indonesia; 2015.

76. MoEF. National Forest Reference Emission Level for Deforestation and Forest Degradation: In the Context of Decision 1/CP.16 para 70 UNFCCC (Encourages developing country Parties to contribute to mitigation actions in the forest sector). Indonesia: DG-PPI MoEF Indonesia; 2015.

77. Chistjakov VI, Kuprijanov AI, Gorhkov VV, Artsybashev ES. Measures for fire prevention on peat deposits. In: Wein RW, MacLean DA, editors. The role of fire in northern circumpolar ecosystems. New York: John Wiley & Sons Ltd; 1983. pp. 259–271.

78. Wein RW. Fire behavior and ecological effects in organic terrain. In: Wein RW, MacLean DA, editors. The role of fire in northern circumpolar ecosystems. New York: John Wiley & Sons Ltd; 1983. pp. 81–95.

79. Austin K, Sheppard S, Stolle F. Indonesia's moratorium on new forest concessions: Key findings and next steps; February 2012. Available: http://www.wri.org/publication/indonesia-moratorium-on-new-forest-concessions.

80. Page SE, Siegert F, Rieley JO, Boehm HV, Jaya A, Limin S. The amount of carbon released from peat and forest fires in Indonesia during 1997. Nat. 2002; 420: 61–65. doi: 10.1038/nature01131

46

Chapter 2. Spatial evaluation of Indonesia's 2015 fire-affected area and estimated carbon emissions using Sentinel-1

Lohberger S, Stängel M, **Atwood EC**, Siegert F. (2018) Spatial evaluation of Indonesia's 2015 fire-affected area and estimated carbon emissions using Sentinel-1. Global Change Biology 24(2): 644–654.

PRIMARY RESEARCH ARTICLE

WILEY Global Change Biology

Spatial evaluation of Indonesia's 2015 fire-affected area and estimated carbon emissions using Sentinel-1

Sandra Lohberger[1] | Matthias Stängel[1] | Elizabeth C. Atwood[1,2] | Florian Siegert[1,2]

[1]RSS Remote Sensing Solutions GmbH, Baierbrunn, Germany

[2]Department of Biology II, GeoBio Center, Ludwig-Maximilians-Universität Munich, Planegg-Martinsried, Germany

Correspondence
Sandra Lohberger, RSS Remote Sensing Solutions GmbH, Baierbrunn, Germany.
Email: lohberger@rssgmbh.de

Funding information
European Space Agency, Grant/Award Number: N°4000115006/15/I-NB

Abstract

Fires raged once again across Indonesia in the latter half of 2015, creating a state of emergency due to poisonous smoke and haze across Southeast Asia as well as incurring great financial costs to the government. A strong El Niño-Southern Oscillation (ENSO) led to drought in many parts of Indonesia, resulting in elevated fire occurrence comparable with the previous catastrophic event in 1997/1998. Synthetic Aperture Radar (SAR) data promise to provide improved detection of land use and land cover changes in the tropics as compared to methodologies dependent upon cloud- and haze-free images. This study presents the first spatially explicit estimates of burned area across Sumatra, Kalimantan, and West Papua based on high-resolution Sentinel-1A SAR imagery. Here, we show that 4,604,569 hectares (ha) were burned during the 2015 fire season (overall accuracy 84%), and compare this with other existing operational burned area products (MCD64, GFED4.0, GFED4.1s). Intersection of burned area with fine-scale land cover and peat layer maps indicates that 0.89 gigatons carbon dioxide equivalents (Gt CO_2e) were released through the fire event. This result is compared to other estimates based on nonspatially explicit thermal anomaly measurements or atmospheric monitoring. Using freely available SAR C-band data from the Sentinel mission, we argue that the presented methodology is able to quickly and precisely detect burned areas, supporting improvement in fire control management as well as enhancing accuracy of emissions estimation.

KEYWORDS
burned area, carbon, El Niño, emissions, fire, Indonesia, Synthetic Aperture Radar

1 | INTRODUCTION

The vast and disastrous fires that swept across Indonesia in 2015 were catastrophic from an economic, public health, ecologic, and global climate perspective. Estimated inland costs hover in excess of 16 billion USD (World Bank 2015), representing 1.8% of Indonesia's gross domestic product in 2014 (Tacconi, 2016) and exceeding the value added from the entire nation's palm oil production (12 billion USD) that same year (World Bank 2016). These estimates do not include costs that are hard to quantitate, such as loss of biodiversity and long-term damage to human health (Chisholm, Wijedasa, &

Swinfield, 2016), or economic costs incurred to neighboring countries (Tacconi, 2016). Peat fires in particular, characterized by smoldering combustion (Page & Hooijer, 2016; Turetsky et al., 2014), produced thick toxic haze which spread over adjacent countries such as Malaysia, Singapore, and Thailand (Blunden & Arndt, 2016; Chisholm et al., 2016; Tacconi, 2016). Current government estimates of area burned are 2.6×10^6 ha, equivalent to four and a half times the size of Bali (Tacconi, 2016; World Bank 2016). Fires are assumed to be primarily started deliberately and illegally for large-scale development of pulpwood and oil palm plantations (Gaveau, Sloan et al., 2014; Page & Hooijer, 2016; Siegert, Ruecker, Hinrichs, & Hoffmann,

2001). Indonesia has often been criticized for its poor fire control (Abood, Lee, Burivalova, Garcia-Ulloa, & Koh, 2015; Barber & Schweithelm, 2000), to which the government responded in 2011 by increasing regulations (Austin, Sheppard, & Stolle, 2012). Despite these measures, uncontrolled fires remain an annual occurrence due to lack of better regulated burning measures and insufficient law enforcement (Chisholm et al., 2016; World Bank 2016).

Drainage of peatland areas increases their susceptibility to fire, which is further enhanced by prolonged drought periods induced by ENSO episodes (Page & Hooijer, 2016; Siegert et al., 2001; Wooster, Perry, & Zoumas, 2012). In 2015, the region experienced an extended ENSO-induced dry period on par with years of record-breaking fire disasters in 1982/1983 and 1997/1998 (Ballhorn, Siegert, Mason, & Limin, 2009; Siegert et al., 2001). Fires are able to spread quickly due to their remote location, aided furthermore by insufficient local fire-fighting infrastructure (Barber & Schweithelm, 2000; Chisholm et al., 2016; World Bank 2016). Smoldering peat fires produce very high levels of carbon emissions (Gaveau, Salim et al., 2014; Muraleedharan, Radojevic, Waugh, & Caruana, 2000; Page & Hooijer, 2016) and can continue to smolder deep below the surface for months, making them quite difficult to extinguish (Page & Hooijer, 2016). Lacking fire control at the start of the 2015 event allowed fires to form burning fronts over 10 km in length (Atwood et al., 2016; Huijnen et al., 2016), producing the thick haze that caused not only economic damage but also many pollution-related health issues (Gross, 2015; Tacconi, 2016).

Estimates of average annual global CO_2 emissions from biomass burning amount to 7.34 Gt CO_2e per year, with 2.20–3.67 Gt CO_2e coming from tropical deforestation and peatland fires (van der Werf et al., 2010). Peatlands represent the largest reservoir of soil carbon worldwide (Margono, Potapov, Turubanova, Stolle, & Hansen, 2014; Page & Hooijer, 2016), of which an estimated 89 Gt carbon (Gt C) are stored in the tropics (Page, Rieley, & Banks, 2011). Southeast Asia is estimated to contain 69 Gt C, with Indonesia alone holding the largest peat deposit (57 Gt C) in the region (Page et al., 2011), thus making this country one of the most important near-surface soil carbon pools in the world (Ballhorn et al., 2009; Page et al., 2011). Indonesian peatland fires from the 1997/98 catastrophe released between 2.97 and 9.43 Gt CO_2e, making up 13–40% of emissions from fossil fuels that year (Gaveau, Salim et al., 2014; Gaveau, Sloan et al., 2014; Page et al., 2002). GFED (Global Fire Emissions Database) provides fire emission estimates of 1.75 Gt CO_2e for the 2015 El Niño event, which are based in part on the MODIS (Moderate Resolution Imaging Spectroradiometer) burned area product. Huijnen et al. (2016) estimated total CO_2 emissions the same year at 0.88 Gt CO_2e over maritime Southeast Asia based on Fire Radiative Power measurements from MODIS coupled with satellite CO measurements and in situ emission factor measurements. Both these estimates are based on datasets with a spatial resolution of 27 km or higher (GFED provides 0.25° resolution and Huijnen et al. (2016) provides 0.50°). Given the importance of peat fires for emissions estimates, it is imperative that such a methodology be based on data allowing spatially exact estimates of burned area at high spatial resolution. Furthermore, both these methods rely heavily on the MODIS hotspots dataset to identify areas of active fire, which has known issues with fire detection through optically thick cloud and smoke cover (Roy, Boschetti, Justice, & Ju, 2008) as well as under-detection of smoldering fires (Atwood et al., 2016; Turetsky et al., 2014). Scaling MODIS active fire detection to burned area estimates in areas with continual cloud cover has also proved difficult (Giglio, Randerson, & van der Werf, 2013; Spessa et al., 2015). This exemplifies the need for an enhanced, high-resolution, nationwide burned area product which enables the identification of fire sources and the possibility of improved fire emission analysis.

Here, we present the first estimates of burned area from the 2015 Indonesian fire catastrophe based on a spatially explicit direct-detection analysis, at high spatial resolution, and an estimate of the resulting emissions released by the fires. Our objectives were to (1) determine the area burned during the 2015 fire catastrophe across the fire prone regions of Sumatra, Kalimantan, and West Papua, (2) derive resulting emissions released based on additional data such as land cover, biomass, and peat maps, and (3) compare our estimates with other burned area and fire emission estimates. Our analysis is based on data supplied by the Sentinel-1 mission, which at the time of the 2015 fires consisted of only one satellite. This mission now operates with two satellites, providing a 6-day repeat cycle and thus offering a good framework for an improved rapid burned area detection algorithm. We argue that the presented methodology lends itself well to the development of a monitoring system that would allow for more accurate assessment of fire-damaged area and the resulting emissions than currently existing methods.

2 | MATERIALS AND METHODS

Our study concentrated on Indonesia's three largest contiguous areas prone to wildfire: the island of Sumatra, Kalimantan on the island of Borneo, and West Papua. These regions are characterized by substantial tropical peat deposits which began to accumulate over 10,000 years ago (Rieley, Siefermann, & Page, 1992). These deposits can reach 20 m depth and cover up to 19.7×10^6 ha of the study area (Page, Rieley, Shotyk, & Weiss, 1999). The overlying tropical forest is home to many endemic and endangered animal and plant species, as well as supporting commercially important stocks of timber. Land cover change in Indonesia remains consistently high, with nationwide rates of primary forest cover loss surpassing Brazil (Margono et al., 2014). Processes such as fire, peatland drainage, deforestation, and establishment of plantations for palm oil or timber are the primary contributors to land cover change (Romijn et al., 2013). Both Sumatra and Kalimantan have experienced some of the highest deforestation rates worldwide for over three decades (Hansen et al., 2009), while the relatively low-populated region of West Papua has shown much lower rates of primary forest losses up through 2010 (Margono et al., 2014).

2.1 | SAR dataset

The European Space Agency (ESA) Sentinel-1 mission is a two satellite constellation, each carrying a C-band SAR sensor onboard which offers high spatial resolution data (10 m). Sentinel-1A was launched April 2014, followed by Sentinel-1B 2 years later. SAR data have the benefit of being daylight and weather independent, capable of penetrating thick smoke and haze, which enables timely detection of burned areas and thus reducing confounding factors from processes such as rapid tropical vegetation regrowth (Siegert & Hoffmann, 2000; Siegert, Hoffmann, & Kuntz, 2000). An example of these issues is shown in Figure 1, where a multitemporal composite SAR image is compared to MODIS hotspots and a Landsat-8 scene taken close to the end of the fire event. Burned areas are visible in the Sentinel-1 composite in orange, forests appear in blue, and oil palm plantations in light green. The false-color Landsat-8 image shown in Figure 1c depicts burned area in red, but due to heavy cloud and smoke cover, the surface reflectance signal is being inhibited in the upper portion of the image. The first post-fire Landsat image with <45% cloud cover over this area was acquired in March 2016, 5 months following the fire event. As stated above, this is a considerable amount of time in terms of tropical vegetation regrowth.

Selection of Sentinel-1A data was based on three criteria: data availability, fire season duration, and regional precipitation. Duration of the regional fire season was determined based on rapid increase in the number of MODIS hotspot detections (Active Fire Product collection MCD14; Giglio, Descloitres, Justice, & Kaufman, 2003), analyzed separately over the three regions. This time period was used to select Sentinel-1A images prior to and following the fire season as closely as possible, with the goal being to capture a clean and clear signal of burned area free from confounding factors such as vegetation regrowth. SAR backscatter is highly sensitive to surface water content due to water's dielectric properties (Lillesand, Kiefer, & Chipman, 2015). Data from the Tropical Rainfall Measuring Mission Multi-Satellite Precipitation Analysis (TRMM 3B42RT; Huffman, Adler, Bolvin, & Nelkin, 2010; Huffman et al., 2007), providing daily global precipitation rates from 50°N to 50°S at a spatial resolution of 0.25° × 0.25°, were incorporated into the data selection process to ensure comparable dry conditions in pre- and postfire acquisitions. Both length of fire season and onset of the rainy period for the region below a particular orbit were considered to select pre- and postfire season acquisitions.

Ground Range Detected (GRD) Level-1 data with mid-swath incidence angles between 38.85° and 39.26° were used in vertical-vertical (VV) and vertical-horizontal (VH) polarization over Kalimantan (ascending) and in VV polarization over Sumatra and West Papua (descending). The data were processed using the Sentinel-1 Toolbox implemented in SNAP (Sentinel Application Platform). All Sentinel-1A scenes were calibrated, radiometric corrected, and multitemporal speckle filtered. Data were controlled for full-coverage availability of pre- and postfire acquisitions with similar orbit pass and polarization. High slope terrain (>15°) had to be excluded for burned area mapping due to relief displacement effects on the SAR backscatter signal (Lillesand et al., 2015). In total, 30,485,500 ha were removed from the burned area analysis, representing 23% of the total project area. Although this is a relatively large percentage, <2% of all MODIS hotspot active fire detections were present in this area and thus the exclusion was assumed acceptable.
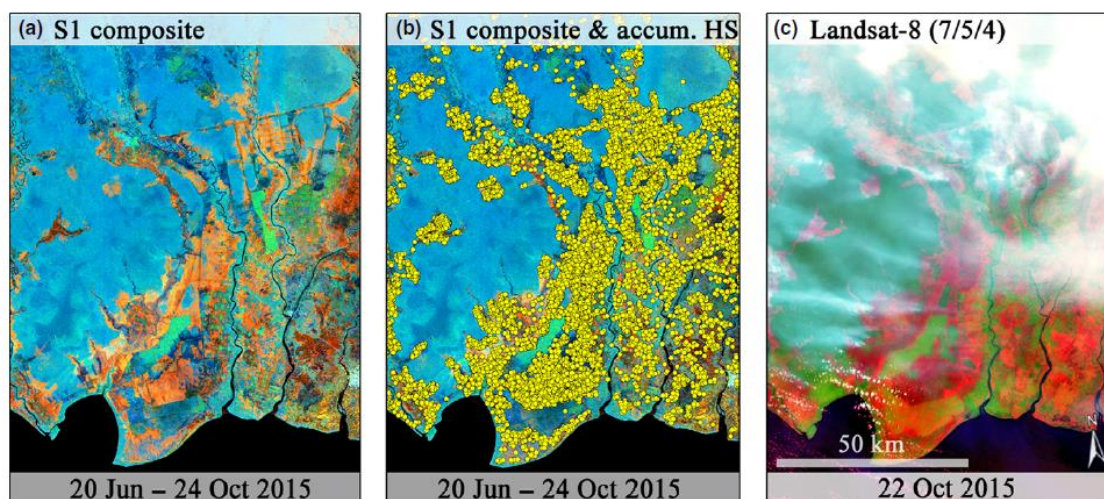
FIGURE 1 (a) A multitemporal false-color SAR composite image (20th Jun.—24th Oct., 2015) from Central Kalimantan comparing change in backscatter signal from prior to and following the fire season (red: backscatter change from before and after the fires; green: VV backscatter of the prefire image; blue: VH backscatter of the postfire image). (b) SAR composite overlain with accumulated MODIS hotspots from the same time period, indicated by yellow dots. (c) Landsat-8 image in false-color (bands 7,5,4) acquired closest to the end of the fire event [Colour figure can be viewed at wileyonlinelibrary.com]

51

2.2 | Burned area classification

An object-based image analysis approach, implemented using eCognition 9.2 (Trimble Navigation Ltd.), was used for segmentation and classification of burned areas. Objects, also known as segments, were first generated using a bottom up multiresolution segmentation to create meaningful objects with respect to the burned areas. Input for the segmentation included Sentinel-1 backscatter layers from before (time step 1; t1) and after the fire event (time step 2; t2), as well as temporal change metrics such as (VH_{t1}/VH_{t2}) and ($VV_{t1}-VV_{t2}$). Objects were classified based on probabilities of belonging to the class "burned area", produced from mean fuzzy logic threshold values for backscatter and temporal change metric layers, as well as neighborhood features and hierarchical relationships. Water bodies were excluded from burned area mapping in order to avoid misclassifications.

2.3 | Burned area validation

A validation analysis was performed comparing the classified burned area against a ground truth dataset consisting of in situ data and multispectral imagery over areas with sufficiently low cloud coverage. In situ data were collected in collaboration with the German Corporation for International Cooperation (GIZ) in South Sumatra, and consisted of GPS locations together with ground and aerial photos acquired by drone. All available in situ data that met specific criteria were used for the Sentinel-1 burned area accuracy assessment (Fig. S1). Selection criteria included removal of points located within 5 m of a burned area boundary and taking into account the spatial inaccuracy of each respective GPS device. This resulted in an in situ dataset of 138 GPS locations, 1,631 photos, and 145 drone samples.

Multispectral imagery (Sentinel-2 and Landsat-8) was used in areas distributed over the three islands that were identified as having sufficiently low cloud coverage to allow comprehensive burned area detection (Fig. S2). Only scenes acquired shortly after the fire season (defined as until December 2015; Table S1) were used to maintain high confidence of burn scar detection. Within each validation site of the multispectral validation, a stratified random sampling was applied using a sample size of 50 (resulting in 1,300 points total). GPS locations, geo-referenced ground photos and aerial drone data as well as each of the stratified random multispectral sampling points were visually categorized into the classes "burned" and "not burned". The GPS locations resulted in an overall accuracy of 77.54%, the photo validation in 84.92% and the drone data in 80.69%. The validation of classified burned areas using multispectral imagery resulted in an overall accuracy of 83.54%. Combining in situ and multispectral validation samples, an overall accuracy of 83.85% and a kappa index of 0.84 was achieved.

2.4 | Fire emissions

Total fire emissions were derived based on the resultant spatially explicit burned area maps and consisted of aboveground emissions from vegetation fires plus emissions coming from burning of underlying peat layers. Estimation of emissions from vegetation fires was based on burned aboveground biomass (AGB) coming from two different approaches. The first method followed (1) a *continuous approach*, based on continuous AGB estimates (Goetz et al., 2009). In this study, AGB maps from (i) Avitabile et al. (2016) and (ii) the GlobBiomass project (Schmullius, 2017; http://globbiomass.org) were utilized. Avitabile et al. (2016) provides a pan-tropical AGB map at 1 km spatial resolution, representative for the 2000s, that was constructed from GLAS LiDAR and MODIS optical data. The ESA DUE 'GlobBiomass' project aims at developing an innovative synergistic mapping approach to create AGB maps at fine spatial resolution in five regional sites for the epochs 2005, 2010, and 2015, and a global map at coarser resolution for the epoch 2010. The regional AGB map of Kalimantan, at a spatial resolution of 100 m for the epoch 2010 and derived from ALOS PALSAR K&C mosaic data, was used to estimate aboveground fire emissions. The most recent map from 2015 could not be used as it depicts the situation after the wildfires.

Emissions were also calculated using (2) a *stratify and multiply approach*. Here, vegetation emission estimation was performed by intersecting classified burned areas with a thematic map of land cover class or vegetation type (Goetz et al., 2009). In this study, we utilized the most recent Indonesian Ministry of Environment and Forestry (MoEF) land cover map from 2013. The MoEF land cover map is based on Landsat imagery and has a spatial resolution of 30 m. Mean AGB values for each land cover class were determined from extensive LiDAR studies within the FORCLIME (Navratil, Konecny, Jubanski, Ballhorn, & Siegert, 2016) and BIOCLIME (Navratil, Englhart, & Siegert, 2016) projects. A detailed list of the specific AGB values per land cover class together with steps for simplified emission estimation can be found in Table S2.

The AGB information from the two different approaches was then intersected with the burned area classification and converted to emissions (Gt CO_2e) by assuming a carbon content of 50% in dry biomass and a conversion factor of 3.67 from C to CO_2e. Previous studies in Indonesia show that forests lose between 92 and 95% of their biomass when fires occur (Englhart, Jubanski, & Siegert, 2013; Hashimotio, Kojima, Tange, & Sasaki, 2000; Hiratsuka, Toma, Diana, Hadriyanto, & Morikawa, 2006). Therefore, we assumed a conservative fire efficiency factor of 92% within forests. For all other land cover classes, we used the simplifying assumption of complete AGB burning and implemented a factor of 100%. Using an AGB estimation map, areas with AGB higher than 100 t/ha were considered forest.

Peat fire emissions were calculated by intersecting burned areas, the land cover or AGB estimation map, and a peat layer provided by Wetlands International (Wahyunto 2004). To estimate emissions as accurately as possible, we used the approach suggested by Konecny et al. (2016), where discrimination between the first fire and second or more fires is made with regard to burn depth into the peat. The Konecny et al. study was based on a 220,000 ha dataset, and determined a peat burn depth of 17 ± 16 cm for the first fire and an average burn depth of 8 cm for all following fires (two or more). This

estimate of first fire peat burn depth is supported by results from Simpson et al. (2016) in degraded peatland areas in Sumatra, who determined an average burn depth of 23 ± 19 cm over 5.2 ha of tropical peatland forest after the 2015 fires. The burn depth estimates from Konecny et al. (2016) translate to carbon loss values of 114 tC/ha for an initial fire and 51 tC/ha for peat areas already burned at least once, which were implemented in this study. Carbon loss was converted to emissions (Gt CO_2e) with the molecular weight conversion factor 3.67. Using the land cover map and taking into account that all peat areas were historically covered by forest, it was presumed that burned areas within forest land cover classes had burned for the first time and all other land cover classes (plantations, scrubland, savannah & swamp, agriculture) had already been burned at least once. Nonforest areas lying over peat are the result of either clearcutting or having been burnt by fire, with the latter being the low-cost method much preferred in Southeast Asia to clear land over large areas (Simorangkir, 2006). Using the AGB estimation map, we assumed that areas considered "forest" (based on AGB higher than 100 t/ha) were burned for the first time while areas with lower biomass values had already burned. It should be noted that under this method, areas able to have sufficiently recovered after a long-past burn event would be grouped as "first time burn".

3 | RESULTS

3.1 | SAR-derived burned area

Comprehensive burned area maps derived from the Sentinel-1A imagery were developed over Sumatra, Kalimantan, and West Papua (Fig. S3). The SAR dataset over entire Borneo is shown in Figure 2a,

depicted as a multitemporal false-color composite (R, G, B coding as in Figure 1). As stated earlier, burned areas are visible in orange, forests appear in blue, and oil palm plantations in light green. The high spatial detail of the dataset enables recognition of patterns in fire occurrence such as elevated prevalence along forest edges (Figure 2b), as well as clear detection of burnt areas surrounding oil palm plantations (Figure 2d).

The object-based classification approach to detect change from before and after the fires provided an estimate of 4,604,569 ha burned by the 2015 fires, with 37% located on peatland areas. The estimated burned area represents 3.2% of the combined regions of Sumatra, Kalimantan, and West Papua, and is close to double that from MoEF (2.6×10^6 ha). Figure 3 shows the detected burned area density over all three regions. Approximately half of the total burned area was located in Kalimantan (2,268,352 ha), of which over one-third (813,152 ha) occurred on peat. Successively less burned area was detected in Sumatra (1,518,127 ha, with 356,434 ha on peat) and West Papua (818,090 ha, with 534,616 ha on peat).

The Sentinel-1-derived burned area was compared to other established burned area products: MODIS Burned Area Product (MCD64A1; Giglio, Loboda, Roy, Quayle, & Justice, 2009), GFED4.0 burned area (Giglio et al., 2013) and GFED4.1s burned area (Giglio et al., 2013; Randerson, Chen, van der Werf, Rogers, & Morton, 2012). This comparison is shown in Table 1. Sentinel-1-derived burned area resulted in the highest estimation followed by GFED4.1s, which made up only 66% of the burned area estimated from Sentinel-1. MODIS achieved the third highest burned area and GFED4.0 estimated the lowest amount of burned area (55% and 40% of the Sentinel-1 estimate, respectively). The percentage of burned area that occurred over peatland areas is lowest for Sentinel-1 (37%), but represents an area of $1,704 \times 10^3$ ha, while the highest
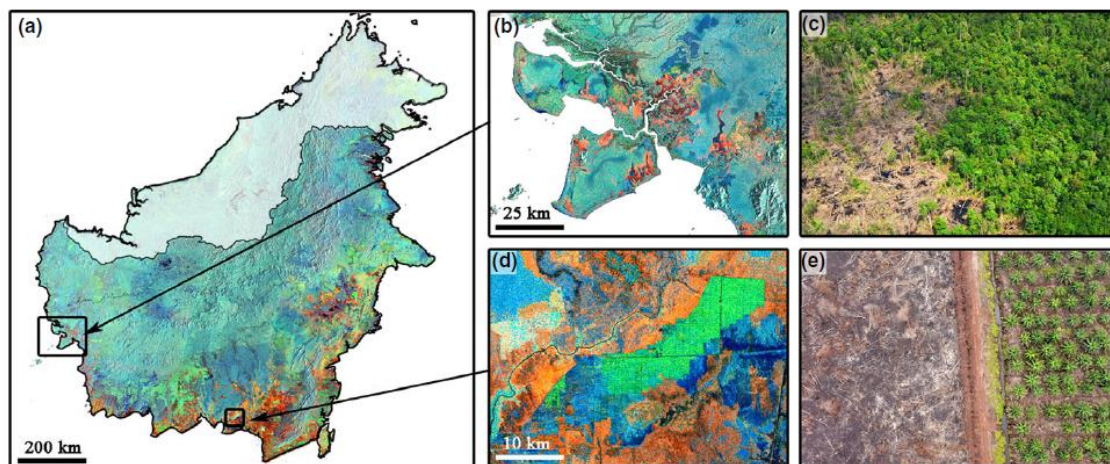
FIGURE 2 Burned area depiction based on high-resolution, multitemporal false-color Sentinel-1 composite image for (a) Kalimantan. Color coding is as in Figure 1. SAR image detail depicted for (b) burned area along forest edges with (c) an aerial photo of such a transition zone, and (d) around plantations with (e) an aerial photo from a palm oil plantation with adjacent burned forest [Colour figure can be viewed at wileyonlinelibrary.com]
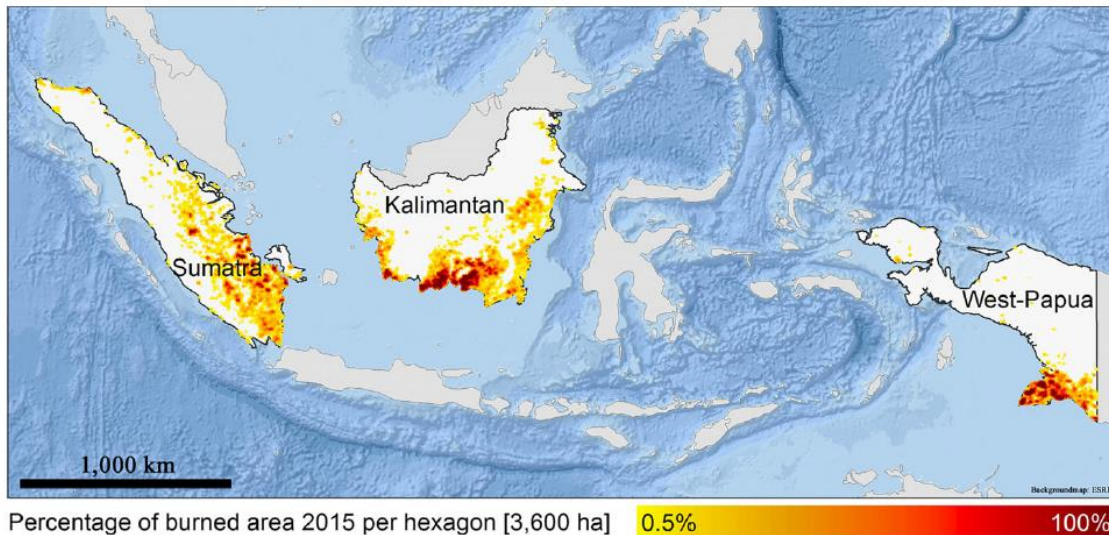
FIGURE 3 Distribution of burned area over Sumatra, Kalimantan, and West Papua. Mapped regions are outlined in black, and detected burned areas are aggregated into 3,600 ha hexagons. White areas depict a burned area fraction <0.5%, whereas yellow to dark red indicates areas of increasing burned fractions up to 100% [Colour figure can be viewed at wileyonlinelibrary.com]

TABLE 1 Comparison from Sentinel-1-derived burned area to existing, operational burned area products

Burned area product	Data specifications			Burned area (10^3 ha)				Percentage of burned area on peat
	Data basis	Spatial resolution (m)	Temporal resolution	Sumatra	Kalimantan	Papua	Total	
Sentinel-1	Sentinel-1	10	12 days	1,518	2,268	818	4,604	37%
GFED4.0	MCD64; VIRS & ATSR active fire data	App. 27,830[a]	Daily & monthly	465	841	522	1,828	39%
GFED4.1s	GFED4 & burned area from Randerson et al. (2012)	App. 27,830[a]	Monthly	921	1,352	756	3,029	41%
MCD64	MODIS imagery; MODIS active fire observation	500	Monthly	638	1,055	845	2,538	45%

[a]Conversion from decimal degree to meter at the equator.

percentage over peatland areas from MODIS only represents $1,144 \times 10^3$ ha. Differences in burned area come primarily from discrepancies in estimations over Sumatra and especially Kalimantan. A thick layer of smoke, haze, and cloud cover, which was continually visible over Borneo during the 2015 fire season, was likely inhibiting the optical and thermal satellite signal utilized by the other burned area products.

3.2 | Fire emissions

Calculated burned area was translated into CO_2 emissions using: (1) a *continuous approach*, based on two separate AGB maps from (i) the ESA GlobBiomass project and (ii) Avitabile et al. (2016); and (2) a *stratify & multiply approach*, based on the categorical MoEF land cover classification map. Emissions from burned aboveground

vegetation and belowground peat layers were calculated separately for all three maps (Table 2). Using the AGB map from Avitabile, we estimated aboveground vegetation fire emissions to be 0.86 Gt CO_2e. Based on the MoEF land cover map, an estimated 0.49 Gt CO_2e were emitted. The regional GlobBiomass AGB map is only available for Kalimantan. This calculation produced 0.25 Gt CO_2e in aboveground vegetation emissions, which is comparable to MoEF estimates for the same region (0.26 Gt CO_2e) but almost half that from Avitabile (0.45 Gt CO_2e). The two approaches diverge less when estimating emissions from burned peat, where emissions based on MoEF are only 14% less compared with Avitabile. Estimates of Kalimantan peat emissions from the GlobBiomass continuous AGB map are quite similar to those from MoEF. Total emissions based on MoEF data came to 0.89 Gt CO_2e, while those from Avitabile were 1.29 Gt CO_2e.

TABLE 2 Emissions from the 2015 fires over the three study regions released by burning of aboveground vegetation and belowground peat layers

		Emissions per region (Gt CO_2e)			
	Dataset	Sumatra	Kalimantan	Papua	Summed
Vegetation emissions	GlobBiomass	n/a	0.25	n/a	n/a
	Avitabile	0.30	0.45	0.11	0.86
	MoEF	0.16	0.26	0.07	0.49
Peat emissions	GlobBiomass	n/a	0.20	n/a	n/a
	Avitabile	0.10	0.22	0.11	0.43
	MoEF	0.10	0.19	0.11	0.40
Total emissions	GlobBiomass	n/a	0.45	n/a	n/a
	Avitabile	0.40	0.67	0.22	1.29
	MoEF	0.26	0.45	0.18	0.89

Calculations are based on two approaches: (1) *continuous*, performed using the AGB map from the GlobBiomass project, available only over Kalimantan, and the Avitabile AGB map; and (2) *stratify & multiply*, which utilizes the MoEF land cover classification map.

Figure 4 shows the distribution of burned area in dark gray across MoEF land cover types that either burned for the first time in recent history (dry land, mangrove, and peat swamp forests) or that had already burned at least once (plantations, scrubland, savannah & swamp, agriculture). Associated emissions, following the *stratify & multiply approach*, for each burned land cover class are also shown in Figure 4 in light gray. Within the forest land cover classes, secondary forest was observed to burn more often than primary forest. In general, degraded forests are more susceptible to fire than undisturbed forests (Ballhorn et al., 2009; Page & Hooijer, 2016; Siegert et al., 2001) due to processes such as peatland drainage (Hoscilo, Page, Tansey, & Rieley, 2011; Konecny et al., 2016), reduced humidity through forest canopy disturbance (Page & Hooijer, 2016) and increased ground litter from anthropogenic activities (Turetsky et al.,

2014). Burning of secondary forest areas was found to produce proportionally higher emissions as compared to areas that had burned at least once in recent history. For instance, the scrubland (S) class burned 18 times more area than in the secondary dry land forest (SDLF) class but produced proportionally much less (a factor of seven) emissions. The effect of underlying peat layers on emissions can be observed when comparing secondary swamp forest (SSF) with savannah & swamp (S&S), where a burned SSF area one-third the size of that in the S&S class produced an equivalent amount of emissions.

4 | DISCUSSION

A SAR methodology is more advantageous for rapid burned area detection in Southeast Asia as compared to procedures based on multispectral data, primarily due to overcoming the need for cloud- and haze-free images from prior to and following a fire event. Despite its benefits, the SAR approach utilized in this study has limitations. The burned area classification captures not only fire affected areas rather all areas with backscatter change above a certain threshold. While backscatter reduction might also result from processes such as flooding, agricultural harvesting, or logging activities, we assume that the primary cause of backscatter reduction during the dry season results from fires, the preferred method to cheaply clear land over large areas in this region (Simorangkir, 2006). Furthermore, fires could have continued to burn during the days between the last SAR acquisition and the onset of rain, which would result in a potential underestimation of the total burned area. Despite these shortcomings, an independent validation of the presented burned area methodology, performed using a comprehensive dataset containing field information, and multispectral imagery, resulted in an overall accuracy of 84%. In this study, only Sentinel-1A data were available, but with the launched Sentinel-1B, acquisition period will decrease to 6 days and a much enhanced multitemporal dataset can be employed in future burned area assessments.
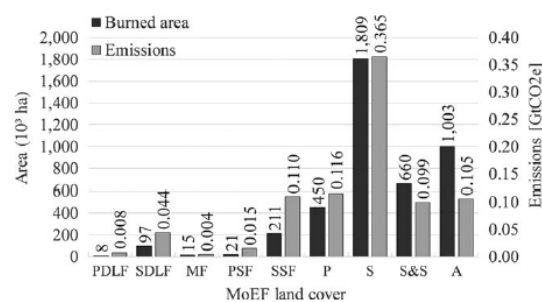
FIGURE 4 Burned area and resultant total (vegetation plus peat) emissions within MoEF land cover classes. Total burned area per class are dark gray (left axis; 10^3 ha) and resultant total emissions are light gray (right axis; Gt CO_2e). Exact totals are indicated above each bar. Land cover classes are based on the MoEF classification: primary and secondary dry land forest (PDLF and SDLF), mangrove forest (MF), primary and secondary swamp forest (PSF and SSF), plantation (P), scrubland (S), savannah & swamp (S&S), and small-plot agriculture (A). Some MoEF classes were merged to enable easier overview (Table S2)

55

The Sentinel-1-derived burned area is close to double that from MoEF (2.6×10^6 ha), which uses methods dependent on cloud- and haze-free multispectral images from before and after the fire events. The latter methodology is difficult to implement given Indonesia's often cloudy tropical climate (Hoscilo et al., 2011; Siegert & Hoffmann, 2000). MODIS burned area (MCD64A1), which is based on MODIS imagery together with MODIS active fire observations at a coarse spatial resolution of 500 m, detected approximately half of the Sentinel-1-derived burned area. GFED4.0 provides burned area estimates at a spatial resolution of 0.25° and is based on the MODIS burned area product (MCD64A1) in combination with VIRS and ATSR active fire data. GFED4.1s burned area estimates also have a spatial resolution of 0.25° and additionally incorporate a small fire database. GFED4.1s burned area estimates are considerably higher ($3,029 \times 10^3$ ha) than GFED4.0 ($1,828 \times 10^3$ ha), but results in only 66% of Sentinel-1-derived burned area. It should be noted that all comparison burned area products are intended for global scale analyses, whereas our presented Sentinel-1 burned area methodology is applied for national-scale analyses.

The method presented here offers rapid and direct detection of burned area at a much improved spatial resolution than previously available. Comparison with other available burned area products, which are based on coarser resolution data, demonstrates that 30–60% more burned area is detected using data with higher spatial resolution. Given the high overall accuracy (84%) and kappa statistic (0.84), we can argue that the presented methodology leads to much improved burned area classifications than until now available. Especially given the enhancement of the Sentinel-1 mission with a second satellite, this methodology allows burned areas detections every 6 days. High spatial resolution is essential for fire management as it furthermore allows fire pattern analysis, such as fire origin detection, which can be used to help to prevent fires in the future. A key component to improving fire management is the early and accurate detection of fire events, allowing proper response to fires while they are still small.

Emissions were estimated using a simplified method based on high-resolution burned areas. Various models (continuous AGB, land cover and peat maps) and datasets (SAR, multispectral imagery, LiDAR, field measurements, and aerial imagery) were used in order to show the potential of enhanced emission estimations. The *stratify & multiply approach*, based on the MoEF dataset, often resulted in lower overall emission estimates than the *continuous approach* calculations based on Avitabile. The MoEF land cover classification is based on remote sensing data from 2013. The Avitabile AGB map is a fusion of the Baccini et al. (2012) and Saatchi et al. (2011) datasets, and is constructed in large part on data that is representative for the 2000s. In the past two decades, Southeast Asia has experienced some of the heaviest rates of tropical forest degradation and deforestation worldwide (Margono et al., 2014; Page & Hooijer, 2016). When comparing the Avitabile AGB map with that of Glob-Biomass (based on data from 2009), we observe low biomass areas being overestimated and thus resulting in fewer areas being classified as previously burned. The Avitabile data also have coarser spatial resolution (1 km) than the MoEF land cover map (30 m) or the GlobBiomass AGB map (100 m). Emissions from the Kalimantan fires calculated from MoEF and GlobBiomass were quite similar (Table 2; both 0.45 Gt CO_2e), while emission estimates based on Avitabile were almost 50% higher. Based on our simplified calculations, the emissions estimation based on the MoEF land cover map is likely the best nationwide representation of actual emissions from the 2015 fires. The GlobBiomass AGB map probably provides an even better estimate for emissions from Kalimantan but is current not available for the rest of Indonesia. Apart from the temporal and spatial resolution differences, whose influence on accuracy is difficult to quantitate, all input models used for the three simplified emission estimations have associated estimation errors. A formal uncertainty analysis of the calculated emissions was well outside the scope of this project but expected overall error should fall within acceptable boundaries due to the high accuracy of burned area detection (84% overall accuracy at higher spatial resolution than hereto available) together with the errors from biomass estimation (GlobBiomass: RMSE up to 57 t/ha; Avitabile: RMSE of 15–21%; MoEF: 88% overall classification accuracy and mean AGB values for each land cover class were calculated from LiDAR measured AGB with an RMSE up to 47 t/ha).

The GFED fire emissions estimate (1.75 Gt CO_2e) is almost double the emissions derived from our approach (Table 2; 0.89 Gt CO_2e based on MoEF), which primarily lies in the assumption of the mean peat burn depth. GFED assumes a mean peat burn depth of 30 cm for Indonesia (van der Werf et al., 2010), supported by an initial LiDAR assessment in Borneo (Ballhorn et al., 2009). More recent LiDAR studies over both large- and small-scale areas alternatively suggest reduced burn depths (Konecny et al., 2016; Simpson et al., 2016), and discrimination between peat burn depth in areas burned for the first time or having already burned at least once in the recent past (17 and 8 cm, respectively; Konecny et al., 2016). The assumed peat burn depth has substantial consequences on the emission estimation as the carbon content of peat per m² can be up to 19 times that of overlaying vegetation layers (Jaenicke, Rieley, Mott, Kimman, & Siegert, 2008). Indonesia alone represents 65% of all tropic peatlands (Page et al., 2011) and is widely recognized globally as one of the most important near-surface soil carbon pools (Ballhorn et al., 2009; Page et al., 2011). Huijnen et al. (2016) estimated the total amount of released fire carbon emissions in 2015 at 0.88 GtCO2e over maritime Southeast Asia (spatial resolution of 0.5°) which is similar to our emission estimates, although the spatial extent is quite different (maritime Southeast Asia compared to Indonesia). The emission estimation of Huijnen et al. (2016) is based on a combination of spatially and temporally explicit Fire Radiative Power measurements from MODIS, coupled with CO measurements made from the MOPITT satellite instrument. Our simplified approach for emission estimations produced estimates on par with Huijnen et al. (2016), but much less than GFED despite the detected burned area being much higher. Main differences in estimations likely result from differences in assumed peat burn depth, available spatial resolutions, or characteristics of the data which were used for burned area/emission estimations. Considering drastic changes in emissions estimates

dependent upon the amount of peat burned, it is clearly advisable to use the most accurate data possible together with the most precise methodology for this region in particular. This indicates the vital importance of utilizing high spatial resolution burned area for fire emission estimation in combination with accurate peat burn depth assumptions and as up-to-date as possible remote sensing data, especially given the rapid rate of land cover change occurring in Southeast Asian tropical forests.

The methodology presented in this study can be automated, thus together with modern cloud computing processing it will offer a closer to real-time, high-resolution burned area product than heretofore possible. The main advantage of SAR methodology is to be independent of smoke, haze, and cloud coverage. The Sentinel-1 burned area product also offers much finer spatial resolution (10 m) than those from MODIS or GFED (500 m resolution at the best), which will allow for analysis of processes such as where fires were started. This is essential information needed by managers interested in improving fire prevention, thus the methodology presented here provides an excellent tool for government agencies responsible for improving fire regulations to avoid such catastrophes in the future. Indonesia still fights with implementing large-scale fire control regulations, with fires of varying severity occurring consistently each year in spite of increased regulations (Page & Hooijer, 2016). Future prevention of large fire disasters in this region is imperative not only for Indonesia, due to both national interests and maintaining good international relations with neighboring countries, but also for the global community given the implications of these fire disasters for the global climate.

CONFLICT OF INTEREST

The authors herewith claim that they have no conflict of interest to declare.

REFERENCES

Abood, S. A., Lee, J. S., Burivalova, Z., Garcia-Ulloa, J., & Koh, L. P. (2015). Relative contributions of the logging, fiber, oil palm, and mining industries to forest loss in Indonesia. *Conservation Letters, 8*, 58–67. https://doi.org/10.1111/conl.12103

Atwood, E. C., Englhart, S., Lorenz, E., Halle, W., Wiedemann, W., & Siegert, F. (2016). Detection and characterization of low temperature peat fires during the 2015 fire catastrophe in Indonesia using a new high-sensitivity fire monitoring satellite sensor (FireBird). *PLoS One, 11*, e0159410. https://doi.org/10.1371/journal.pone.0159410

Austin, K., Sheppard, S., & Stolle, F. (2012). *Indonesia's moratorium on new forest concessions: Key findings and next steps*. Retrieved from https://wri.org/sites/default/files/indonesia_moratorium_on_new_forest_concessions.pdf

Avitabile, V., Herold, M., Heuvelink, G. B., Lewis, S. L., Philips, O. L., Asner, G. P., ... Willcock, S. (2016). An integrated pan-tropical biomass map using multiple reference datasets. *Global Change Biology, 22*, 1406–1420. https://doi.org/10.1111/gcb.13139

Baccini, A., Goetz, S. J., Walker, W. S., Laporte, N. T., Sun, M., Sulla-Menashe, D., ... Houghton, R. A. (2012). Estimated carbon dioxide emissions from tropical deforestation improved by carbon-density maps. *Nature Climate Change, 2*, 182–185. https://doi.org/10.1038/nclimate1354

Ballhorn, U., Siegert, F., Mason, M., & Limin, S. (2009). Derivation of burn scar depths and estimation of carbon emissions with LIDAR in Indonesian peatlands. *Proceedings of the National Academy of Sciences of the United States of America, 106*, 21213–21218. https://doi.org/10.1073/pnas.0906457106

Barber, C. V., & Schweithelm, J. (2000). *Trial by fire: Forest fires and forestry policy in Indonesia's era of crisis and reform*. Washington, DC: World Resources Institute Forest Frontiers Initiative in collaboration with WWF-Indonesia & Telapak Indonesia Foundation.

Blunden, J., & Arndt, D. S. (2016). State of the climate in 2015. *Bulletin of the American Meteorological Society, 97*, Si–S275. https://doi.org/10.1175/2016BAMSStateoftheClimate. 1

Chisholm, R. A., Wijedasa, L. S., & Swinfield, T. (2016). The need for long-term remedies for Indonesia's forest fires. *Conservation Biology, 30*, 5–6. https://doi.org/10.1111/cobi.12662

Englhart, S., Jubanski, J., & Siegert, F. (2013). Quantifying dynamics in tropical peat swamp forest biomass with multi-temporal LiDAR datasets. *Remote Sensing, 5*, 2368–2388. https://doi.org/10.3390/rs5052368

Gaveau, D. L., Salim, M. A., Hergoualc'h, K., Locatelli, B., Sloan, S., Wooster, M., ... Sheil, D. (2014). Major atmospheric emissions from peat fires in Southeast Asia during non-drought years: Evidence from the 2013 Sumatran fires. *Scientific Reports, 4*, 6112. https://doi.org/10.1038/srep06112

Gaveau, D. L., Sloan, S., Molidena, E., Yaen, H., Sheil, D., Abram, N. K., ... Meijaard, E. (2014). Four decades of forest persistence, clearance and logging on Borneo. *PLoS One, 9*, e101654. https://doi.org/10.1371/journal.pone.0101654

Giglio, L., Descloitres, J., Justice, C. O., & Kaufman, Y. J. (2003). An enhanced contextual fire detection algorithm for MODIS. *Remote Sensing of Environment, 87*, 273–282. https://doi.org/10.1016/S0034-4257(03)00184-6

Giglio, L., Loboda, T., Roy, D. P., Quayle, B., & Justice, C. O. (2009). An active-fire based burned area mapping algorithm for the MODIS sensor. *Remote Sensing of Environment, 113*, 408–420. https://doi.org/10.1016/j.rse.2008.10.006

Giglio, L., Randerson, J. T., & van der Werf, G. R. (2013). Analysis of daily, monthly, and annual burned area using the fourth-generation global fire emissions database (GFED4). *Journal of Geophysical Research: Biogeosciences, 118*, 317–328. https://doi.org/10.1002/jgrg.20042

Goetz, S. J., Baccini, A., Laporte, N. T., Johns, T., Walker, W., Kellndorfer, J., ... Sun, M. (2009). Mapping and monitoring carbon stocks with satellite observations: A comparison of methods. *Carbon Balance and Management, 4*, 2. https://doi.org/10.1186/1750-0680-4-2

Gross, M. (2015). A fire with global connections. *Current Biology, 25*, R1107–R1109. https://doi.org/10.1016/j.cub.2015.11.029

Hansen, M. C., Stehman, S. V., Potapov, P. V., Arunarwati, B., Stolle, F., & Pittman, K. (2009). Quantifying changes in the rates of forest clearing in Indonesia from 1990 to 2005 using remotely sensed data sets. *Environmental Research Letters, 4*, 34001. https://doi.org/10.1088/1748-9326/4/3/034001

Hashimotio, T., Kojima, K., Tange, T., & Sasaki, S. (2000). Changes in carbon storage in fallow forests in the tropical lowlands of Borneo. *Forest Ecology and Management*, 126, 331–337. https://doi.org/10.1016/S0378-1127(99)00104-8

Hiratsuka, M., Toma, T., Diana, R., Hadriyanto, D., & Morikawa, Y. (2006). Biomass recovery of naturally regenerated vegetation after the 1998 forest fire in East Kalimantan, Indonesia. *Japan Agricultural Research Quarterly*, 40, 277–282. https://doi.org/10.6090/jarq.40.277

Hoscilo, A., Page, S. E., Tansey, K. J., & Rieley, J. O. (2011). Effect of repeated fires on land-cover change on peatland in southern Central Kalimantan, Indonesia, from 1973 to 2005. *International Journal of Wildland Fire*, 20, 578. https://doi.org/10.1071/WF10029

Huffman, G. J., Adler, R. F., Bolvin, D. T., & Nelkin, E. J. (2010). The TRMM Multi-Satellite Precipitation Analysis (TMPA). In M. Gebremichael, & F. Hossain (Eds.), *Satellite rainfall applications for surface hydrology* (pp. 3–22). Netherlands, Dordrecht: Springer.

Huffman, G. J., Bolvin, D. T., Nelkin, E. J., Wolff, D. B., Adler, R. F., Gu, G., ... Stocker, E. F. (2007). The TRMM Multisatellite Precipitation Analysis (TMPA): Quasi-global, multiyear, combined-sensor precipitation estimates at fine scales. *Journal of Hydrometeorology*, 8, 38–55. https://doi.org/10.1175/JHM560.1

Huijnen, V., Wooster, M. J., Kaiser, J. W., Gaveau, D. L. A., Flemming, J., Parrington, M., ... van Weele, M. (2016). Fire carbon emissions over maritime Southeast Asia in 2015 largest since 1997. *Scientific Reports*, 6, 26886. https://doi.org/10.1038/srep26886

Jaenicke, J., Rieley, J. O., Mott, C., Kimman, P., & Siegert, F. (2008). Determination of the amount of carbon stored in Indonesian peatlands. *Geoderma*, 147, 151–158. https://doi.org/10.1016/j.geoderma.2008.08.008

Konecny, K., Ballhorn, U., Navratil, P., Jubanski, J., Page, S. E., Tansey, K., ... Siegert, F. (2016). Variable carbon losses from recurrent fires in drained tropical peatlands. *Global Change Biology*, 22, 1469–1480. https://doi.org/10.1111/gcb.13186

Lillesand, T. M., Kiefer, R. W., & Chipman, J. W. (2015). *Remote sensing and image interpretation* (p. 18). Hoboken, NJ: Wiley.

Margono, B. A., Potapov, P. V., Turubanova, S., Stolle, F., & Hansen, M. C. (2014). Primary forest cover loss in Indonesia over 2000–2012. *Nature Climate Change*, 4, 730–735. https://doi.org/10.1038/nclimate2277

Muraleedharan, T. R., Radojevic, M., Waugh, A., & Caruana, A. (2000). Emission from the combustion of peat: An experimental study. *Atmospheric Environment*, 34, 3033–3055. https://doi.org/10.1016/S1352-2310(99)00512-9

Navratil, P., Englhart, S., & Siegert, F. (2016). *Quality assessment report of ICRAF historic land cover change dataset*. Baierbrunn, Germany: RSS - Remote Sensing Solutions GmbH.

Navratil, P., Konecny, K., Jubanski, J., Ballhorn, U., & Siegert, F. (2016). *Development of LiDAR based aboveground biomass models in Kalimantan: Locally explicit emission factors in Kapuas Hulu*. Jakarta, Indonesia: Deutsche Gesellschaft für Internationale Zusammenarbeit (GIZ) GmbH.

Page, S. E., & Hooijer, A. (2016). In the line of fire: The peatlands of Southeast Asia. *Philosophical Transactions of the Royal Society of London. Series B, Biological Sciences*, 371, 20150176. https://doi.org/10.1098/rstb.2015.0176

Page, S. E., Rieley, J. O., & Banks, C. J. (2011). Global and regional importance of the tropical peatland carbon pool. *Global Change Biology*, 17, 798–818. https://doi.org/10.1111/j.1365-2486.2010.02279.x

Page, S. E., Rieley, J. O., Shotyk, W., & Weiss, D. (1999). Interdependence of peat and vegetation in a tropical peat swamp forest. *Philosophical Transactions of the Royal Society of London. Series B, Biological Sciences*, 354, 1885–1897. https://doi.org/10.1098/rstb.1999.0529

Page, S. E., Siegert, F., Rieley, J. O., Boehm, H.-D. V., Jaya, A., & Limin, S. (2002). The amount of carbon released from peat and forest fires in Indonesia during 1997. *Nature*, 420, 61–65. https://doi.org/10.1038/nature01131

Randerson, J. T., Chen, Y., van der Werf, G. R., Rogers, B. M., & Morton, D. C. (2012). Global burned area and biomass burning emissions from small fires. *Journal of Geophysical Research: Biogeosciences*, 117, G04012. https://doi.org/10.1029/2012JG002128

Rieley, J. O., Siefermann, R. G., & Page, S. E. (1992). The origin, development, present status and importance of the lowland peat swamp forests of Borneo. *Suo*, 43, 241–244.

Romijn, E., Ainembabazi, J. H., Wijaya, A., Herold, M., Angelsen, A., Verchot, L., & Murdiyarso, D. (2013). Exploring different forest definitions and their impact on developing REDD+ reference emission levels: A case study for Indonesia. *Environmental Science & Policy*, 33, 246–259. https://doi.org/10.1016/j.envsci.2013.06.002

Roy, D. P., Boschetti, L., Justice, C. O., & Ju, J. (2008). The collection 5 MODIS burned area product — Global evaluation by comparison with the MODIS active fire product. *Remote Sensing of Environment*, 112, 3690–3707. https://doi.org/10.1016/j.rse.2008.05.013

Saatchi, S. S., Harris, N. L., Brown, S., Lefsky, M., Mitchard, E. T. A., Salas, W., ... Morel, A. (2011). Benchmark map of forest carbon stocks in tropical regions across three continents. *Proceedings of the National Academy of Sciences of the United States of America*, 108, 9899–9904. https://doi.org/10.1073/pnas.1019576108

Schmullius, C. (2017). *GlobBIOMASS – Estimates of Biomass on Global and Regional Scales*. 37th International Symposium on Remote Sensing of Environment (ISRSE-37), 8–12 May, 2017, Tschwane, South Africa.

Siegert, F., & Hoffmann, A. A. (2000). The 1998 forest fires in East Kalimantan (Indonesia): A quantitative evaluation using high resolution, multitemporal ERS-2 SAR images and NOAA-AVHRR hotspot data. *Remote Sensing of Environment*, 72, 64–77.

Siegert, F., Hoffmann, A., & Kuntz, S. (2000). Comparison of ATSR and NOAA AVHRR hotspot data acquired during an exceptional fire event in Kalimantan (Indonesia). *European Space Agency (Special Publication)*, 479, 122–128.

Siegert, F., Ruecker, G., Hinrichs, A., & Hoffmann, A. A. (2001). Increased damage from fires in logged forests during droughts caused by El Niño. *Nature*, 414, 437–440. https://doi.org/10.1038/35106547

Simorangkir, D. (2006). Fire use: Is it really the cheaper land preparation method for large-scale plantations? *Mitigation and Adaptation Strategies for Global Change*, 12, 147–164. https://doi.org/10.1007/s11027-006-9049-2

Simpson, J., Wooster, M., Smith, T., Trivedi, M., Vernimmen, R., Dedi, R., ... Dinata, Y. (2016). Tropical peatland burn depth and combustion heterogeneity assessed using UAV photogrammetry and airborne LiDAR. *Remote Sensing*, 8, 1000. https://doi.org/10.3390/rs8121000

Spessa, A. C., Field, R. D., Pappenberger, F., Langner, A., Englhart, S., Weber, U., ... Moore, J. (2015). Seasonal forecasting of fire over Kalimantan, Indonesia. *Natural Hazards and Earth System Science*, 15, 429–442. https://doi.org/10.5194/nhess-15-429-2015

Tacconi, L. (2016). Preventing fires and haze in Southeast Asia. *Nature Climate Change*, 6, 640–643. https://doi.org/10.1038/nclimate3008

Turetsky, M. R., Benscoter, B., Page, S., Rein, G., van der Werf, Guido. R., & Watts, A. (2014). Global vulnerability of peatlands to fire and carbon loss. *Nature Geoscience*, 8, 11–14. https://doi.org/10.1038/ngeo2325

van der Werf, G. R., Randerson, J. T., Giglio, L., Collatz, G. J., Mu, M., Kasibhatla, P. S., ... van Leeuwen, T. T. (2010). Global fire emissions and the contribution of deforestation, savanna, forest, agricultural, and peat fires (1997–2009). *Atmospheric Chemistry and Physics*, 10, 11707–11735. https://doi.org/10.5194/acp-10-11707-2010

Wahyunto (Ed.) (2004). *Peta sebaran lahan gambut, luas, dan kandungan karbon di Kalimantan. Map of peatland distribution area and carbon content in Kalimantan, 2002–2002*. Bogor Jawa Barat, Indonesia:

Wetlands International – Indonesia Programme & Wildlife Habitat Canada (WHC).

Wooster, M. J., Perry, G. L., & Zoumas, A. (2012). Fire, drought and El Niño relationships on Borneo (Southeast Asia) in the pre-MODIS era (1980–2000). *Biogeosciences, 9*, 317–340. https://doi.org/10.5194/bg-9-317-2012

World Bank (2015). *Indonesia economic quarterly: Reforming amid uncertainty*. Retrieved from http://pubdocs.worldbank.org/en/8441714 50085661051/IEQ-DEC-2015-ENG.pdf

World Bank (2016). *The cost of fire: An economic analysis of Indonesia's 2015 fire crisis*. Retrieved from http://documents.worldbank.org/cura ted/en/776101467990969768/pdf/103668-BRI-Cost-of-Fires-Knowled ge-Note-PUBLIC-ADD-NEW-SERIES-Indonesia-Sustainable-Landscapes-Knowledge-Note.pdf

SUPPORTING INFORMATION

Additional Supporting Information may be found online in the supporting information tab for this article.

How to cite this article: Lohberger S, Stängel M, Atwood EC, Siegert F. Spatial evaluation of Indonesia's 2015 fire-affected area and estimated carbon emissions using Sentinel-1. *Glob Change Biol*. 2018;24:644–654. https://doi.org/10.1111/gcb.13841

Section II: Plastic in waterways and the oceans

Chapter 3. Coastal accumulation of microplastic particles emitted from the Po River, Northern Italy: Comparing remote sensing and ocean current modelling with in situ sample collections

Atwood EC, Falcieri FM, Piehl S, Bochow M, Matthies M, Franke J, Carniel S, Sclavo M, Laforsch C, Siegert F.

Coastal accumulation of microplastic particles emitted from the Po River, Northern Italy: Comparing remote sensing and ocean current modelling with *in situ* sample collections

Elizabeth C. Atwood[a,b]*, Francesco M. Falcieri[c], Sarah Piehl[d], Mathias Bochow[d,e], Michael Matthies[f], Jonas Franke[a], Sandro Carniel[c], Mauro Sclavo[c], Christian Laforsch[d], Florian Siegert[a,b]

[a]*RSS Remote Sensing Solutions GmbH, Isarstr. 3, 82065 Baierbrunn, Germany*

[b]*Ludwig-Maximilians-Universität Munich, GeoBio-Center, Großhadernerstr. 2, 82152 Planegg-Martinsried, Germany*

[c]*Consiglio Nazionale delle Ricerche – Istituto di Scienze Marine (CNR-ISMAR), Arsenale-Tesa 104, Castello 2737/F, 30122 Venezia, Italy*

[d]*University Bayreuth, Dept. Animal Ecology I, Universitätsstr. 30, 95440 Bayreuth, Germany*

[e]*Helmholtz Centre Potsdam – GFZ German Research Centre for Geosciences, Telegrafenberg, 14473 Potsdam,*
Germany

[f]*University of Osnabrück, Institute of Environmental Systems Research, Barbarastr. 12, 49069 Osnabrück, Germany*

*corresponding author email: atwood@rssgmbh.de

Abstract

To date, microplastic research has mainly concentrated on open seas, while riverine plumes remain largely unexplored despite their hypothesized importance as a source of microplastics in coastal waters. In this work, coastal accumulation of particles emitted by the Po River over 1.5 years was modeled. We posit that river-induced microplastic accumulation can be predicted using (1) hydrodynamic-based and (2) remote sensing-based modelling. Model accumulation maps were validated against sampling at nine beaches, with sediment microplastic concentrations up to 78.8 particles/kg (dry weight). Hydrodynamic modelling revealed that discharged particle amount is only semi-coupled to beaching rates, which are strongly mouth dependent and occur within the first ten days. Remote sensing modelling was found to better capture river mouth relative strength, and accumulation patterns were found to be consistent with hydrodynamic modelling. This methodology lays groundwork for developing an operational monitoring system to assess microplastic pollution being emitted by a major river.

Introduction

Marine plastic litter has long been recognized as an environmental problem (Azzarello and van Vleet, 1987; Law and Thompson, 2014; Sheavly and Register, 2007) that has only recently begun to receive international attention at a level adequate to the potential severity of the threat (G7 Germany, 2015; GESAMP, 2016; UNEP, 2016). Microplastics, commonly defined as particles < 5 mm in diameter (Galgani et al., 2013), are increasingly proven to be ubiquitous in all water systems. Since first documentation of small plastic litter within the oceans (Carpenter and Smith, 1972; Colton et al., 1974), these particles have been detected in high mountain lakes (Imhof et al., 2013), remote inland water bodies (Free et al., 2014), major river systems (Mani et al., 2015; Moore et al., 2011; Zhang et al., 2015) and throughout the open ocean (Cózar et al., 2014; Eriksen et al., 2014; Law et al., 2014). Floating microplastics can be ingested by a wide variety of marine organisms (Andrady, 2017), beginning at the base of the food chain with zooplankton (Cole et al., 2015; Desforges et al., 2015), through filter feeding species of shellfish (Devriese et al., 2015; van Cauwenberghe and Janssen, 2014), bony fish (Collard et al., 2017; Romeo et al., 2015) and whales (Besseling et al., 2015), as well as higher trophic level marine mammals (Eriksson and Burton, 2003). A portion of these particles inherently contain harmful plastic additives such as polybrominated diphenyl ethers (PBDE), phthalates, nonylphenols (NP) and bisphenol A (BPA), which are known from both laboratory and field studies to be transferable to living tissues (Hermabessiere et al., 2017). Furthermore, particle surface characteristics enable continual adsorption of hydrophobic Persistent Organic Pollutants (POPs) from the marine environment (Ogata et al., 2009), thus providing a concentrated dose of banned chemical compounds to the organism which ingests the particle (Rios et al., 2007). Micrometer-sized plastic particles can translocation to other organs upon ingestion (Collard et al., 2017). Microplastic particles have been found in commercial canned fish products such as anchovy, herring and sprat (Collard et al., 2017; Karami et al., 2017a) as well as aquaculture-grown oysters and mussels (van Cauwenberghe and Janssen, 2014) and commercial sea salt (Karami et al., 2017b). It is estimated that all plastic waste entering the oceans each year causes an annual loss of $13 billion USD through environmental damage to marine ecosystems (UNEP, 2014), and the adverse effects to human health are still a subject of continued study (Schirinzi et al., 2017; Seltenrich, 2015).

Within the past half century, annual plastic production has increased by over two orders of magnitude to reach 332 million tonnes being manufactured worldwide

(PlasticsEurope, 2016). Over one third is used in disposable packaging, which is discarded within one year following production (Derraik, 2002; Lebreton et al., 2012; Thompson et al., 2009). Controlling for population growth over the last 60 years reveals that per capita consumption of plastics has been increasing sharply since the turn of the millennium (Andrady, 2017). Jambeck et al. (2015) estimated that between 4.8 and 12.7 million tonnes of plastic from land sources entered the oceans in 2010. In contrast, the most recent global estimate of floating microplastic debris within the oceans ranges between 96 and 236 thousand tonnes (van Sebille et al., 2015), greatly exceeding previous estimates of 7 to 35 thousand tonnes (Cózar et al., 2014) and 36 thousand tonnes (Eriksen et al., 2014). The discrepancy in excess of one order of magnitude between these estimates indicates the need to further improve in our understanding of relevant source/sink dynamics. Recent studies have shed more light on the vertical mixing of buoyant microplastics at the sea surface (Brunner et al., 2015; Kooi et al., 2016), as well as processes resulting in changes in particle density, such as flocculation and biofouling (Fazey and Ryan, 2016). Despite these advances, there remains much to still be clarified about the sources and sinks of plastic litter entering the oceans (Galgani et al., 2017; Law and Thompson, 2014; Zhang et al., 2017).

Roughly 70 to 80% of marine debris comes primarily from land-based sources (Wagner et al., 2014), much being passively collected into waterways which eventually flow to the sea. Mani et al. (2015) found river water concentrations up to 3.9 million particles/km² in metropolitan areas along the Rhine. Annual input of plastic particles to the Great Lakes is estimated at 9.8 thousand tonnes (Hoffman and Hittinger, 2017). Despite the fact that freshwater systems are equally as severely contaminated as the oceans (Dris et al., 2015), large rivers have received relatively little attention (Mani et al., 2015; Wagner et al., 2014). Between 1.15 and 2.41 million tonnes enter the oceans each year from rivers alone (Lebreton et al., 2017), representing up to 50% of the Jambeck et al. (2015) land based plastic emissions estimate. Besides rivers, other sources of land-based plastics to the oceans include atmospheric transport, beaches, harbors, storm water runoff, aquaculture and fishing activities (Lebreton et al., 2017; Wagner et al., 2014). Our understanding of the physical processes which determine microplastics transportation pathways upon being released into coastal seas is still limited. Some authors suggest that these processes may to some extent be comparable to well-studied suspended sediment transportation systems (Zhang, 2017), which could offer a more established framework for modelling microplastic transportation.

Microplastic transportation pathways are characterized by complex dynamics due to processes such as movement mechanisms (windage and sinking velocities) and unknown fragmentation rates (Law and Thompson, 2014). A combined hydrodynamic-Lagrangian transportation model effort would therefore be surely dependent upon necessary simplifying assumptions, as well as the quality of the forcing data. Such models, with different degrees of realism, have been recently utilized to hindcast potential sources of stranded plastic litter in the Indian Ocean (Bouwman et al., 2016; Duhec et al., 2015), Aegean Sea (Politikos et al., 2017) and Adriatic Sea (Carlson et al., 2017). To date, little attention has been placed on local-scale river plume microplastic transport modelling in coastal seas (Browne et al., 2010; Carlson et al., 2017; Zhang, 2017). It is furthermore important to note that dispersion pathways computed based on modelling results can accumulate errors over long distances and times, in part due to model assumptions diverging from reality. A remote sensing image, on the other hand, offers a real-life picture of the river plume that inherently includes actual environmental conditions. While an image provides a powerful technique of displaying the complex coastal ocean environment, it nevertheless offers restricted information for below the water surface and only represents the snapshot time period when the image was acquired.

In this paper, we implement and compare two different types of models to assess how microplastics from a major river is spreading into a semi-enclosed sea and accumulating along its coastline. Model (1) is a numerical tool based on a state-of-the-art hydrodynamic model, providing basin dynamical features, linked to a sub-module that adopts these velocity fields to carry out Lagrangian particle transportation. Model (2) is based on satellite remote sensing of river plume form and intensity along the coastline. We hypothesize that both models are able to capture coastal patterns in river plume emitted microplastic accumulation. Development of a system to model coastal accumulation of microplastic debris from rivers would represent a very useful tool for agencies responsible for monitoring and reporting this pollution as well as organization of clean-up activities and remediation strategies.

Materials and Methods

The Adriatic Sea separates the Italian peninsula and Balkan coast, extending 800 km from the connection with the Ionian Sea over the Strait of Otranto northwest toward the Venice Lagoon (Figure 1). The sea is bordered by six different countries, namely Albania, Montenegro, Bosnia and Herzegovina, Croatia, Slovenia and Italy. The Italian western coastline is characterized by terraced and alluvial plains in the north that change to karst cliffs along the Gargano Promontory, in contrast to the rocky eastern coastline strewn with karst protrusions and many small islands. The prevailing currents flow counterclockwise from the Strait of Otranto along the Balkan coastline and return southward with the Western Adriatic Current (WAC) along the Italian coastline (Artegiani et al., 1997a, 1997b; Carniel et al., 2016). The Adriatic coastline contains a population of over 3.5 million, of which over 27% is concentrated in the cities of Bari, Venice, Trieste and Split. Important financial sectors of the Adriatic coasts include fisheries, tourism and maritime transportation. The North Adriatic sub-basin is defined as the shallow area north than the 100 m isobath (Figure 1). Tidal fluctuation is usually small, on the scale of 30 cm, but in conjunction with exceptional river discharges, seiche and wind events tidal range can reach up to 140 cm and result in flooding events in the Venice lagoon (familiarly known as "acqua alta").
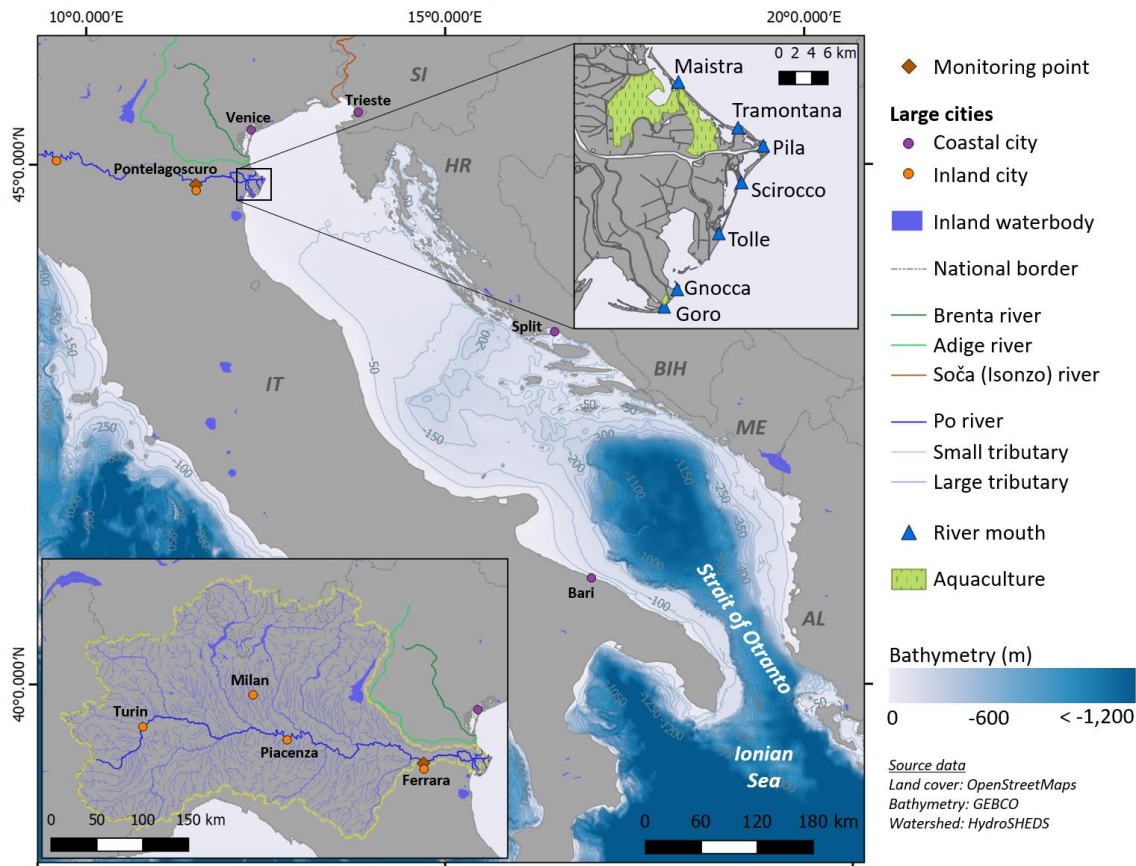
Figure 1: Adriatic Sea overview map, showing bathymetry (contour lines follow 50 m depth intervals) along with large coastal cities and bordering countries: AL - Albania, ME - Montenegro, BIH - Bosnia and Herzegovina, HR - Croatia, SI - Slovenia, IT - Italy. Lower left inset shows Po River watershed (yellow dashed line) with large inland cities, as well as the Brenta (dark green line) and Adige (light green line) rivers. The Po Delta is displayed in the upper right inset, showing all five major river mouths (Maistra, Pila, Tolle, Gnocca and Goro) as well as important side channels (Tramontana, Scirocco) and aquaculture areas.

The Po River provides the largest riverine influx to the Adriatic Sea, averaging daily 1500 m³/s with streamflow ranging between 100 m³/s and 11,550 m³/s (Falcieri et al., 2014). Other large rivers, with average discharge between 90-240 m³/s, flowing into the North Adriatic are the Adige, Soča (or Isonzo) and Brenta (Cozzi and Giani, 2011; Falcieri et al., 2014; Figure 1). Being the longest river in Italy, the Po River drainage area (74,000 km²) encompasses much of the northern region of the country and includes the cities of Turin, Piacenza, Ferrara and Milan (lower left inset Figure 1). The Po Delta wetlands are split into two protected park systems, managed separately by the regions of Veneto and Emilia-Romagna. The unique landscape, consisting of wetlands, forests, sand dunes and salt pans, supports a high biodiversity of both plant and animal species, particularly various types of birds, led to the delta becoming a UNESCO World Heritage Site in 1999. The river splits into many sub-rivers before flowing into the Adriatic Sea, the main recognized arms of which are the Po di Maistra, della Pila, delle Tolle, di

Gnocca (or della Donzella) and di Goro (upper right inset Figure 1). Additionally, there exist many side channels and lagoons which also carry a portion of the river water to the sea, notable among these are the Busa di Scirocco and di Tramontana. The delta is an actively changing system with shifting sandbars that can obstruct outflow from a particular mouth (Simeoni and Corbau, 2009) and thus increase the outflow elsewhere. The highest river discharge occurs in the spring, associated with high precipitation and snow-melt runoff, and the lowest in autumn (Falcieri et al., 2014). The Po Delta is bordered to the north by the Adige and Brenta rivers (respective average discharges of 235 and 93 m³/s, see Figure 1), which become incorporated with the Po River plume.

Both wind regime and freshwater influx play a deciding role in North Adriatic circulation patterns (Bignami et al., 2007; Bolaños et al., 2014; Falcieri et al., 2014). There are three main recognized wind regimes: Bora, Scirocco and Mistral. Bora events consist of strong, dry, northeasterly winds that tend to occur more often during the winter months, which together with low river discharge results in a small Po river plume that remains close to the coastline (Boldrin et al., 2009; Falcieri et al., 2014). As mentioned above, a Scirocco event comprises warm, humid, east-southeasterly winds that tend to occur more often during the spring to fall. This wind regime together with high river discharge results in a wider plume that can extend far across the Adriatic Basin. Mistral events are the least powerful of the wind regimes and are defined based on winds coming from the northwest, which have been found to minorly enhance WAC flow into the Ionian Sea (Bignami et al., 2007).

Sample design

The Po Delta field campaign was conducted from June 4th-25th, 2016, during which both water and sediment samples were taken. Water sample locations were selected to cover the main Po river, recognized river mouths and important subsidiary river mouths as well as the plume, ranging from near-coast water to the plume outer edge (indicated by surface waters with salinity more than 30 PSU). At each station, microplastic concentrations were sampled using a specially designed mini-manta trawl (15 cm x 30 cm opening with integrated flowmeter, 300 µm mesh, trawl locations are indicated in Figure 3 of the Results). One trawl pass per location was conducted alongside the boat for an average of 20 minutes and only when wind conditions were below Beaufort 2. Samples were stored in glass jars until further processing in the lab. During trawling, *in situ* measurements were collected for water clarity (visibility depth with a Secchi disk), sea surface

temperature (°C) and salinity (PSU). Additionally, 2 L water samples were collected from the water surface (top 40 cm) for later determination of further water parameters: chlorophyll-A (Chl-A), suspended particulate matter (SPM) and colored dissolved organic matter (cDOM, or Gelbstoff). These samples were wrapped in aluminum and kept cooled with ice until filtering the same day.

Chl-A samples were filtered using Whatman GF/F glass microfiber filters (0.7 µm pore size), following the IOC and SCOR (1994) protocol. Filters were then wrapped in aluminum and stored at -20° C for the remainder of the field campaign, after which they were stored in the lab at -80° C until further processing. Chl-A was extracted with 96 % EtOH and analyzed with a JASCO FP-8600 fluorometer at an excitation wavelength of 435 nm and an emission wavelength of 670 nm. The fluorometer was calibrated using a photometer (JASCO V-670) and a Chl-A standard (C6144-1MG, Sigma-Aldrich). After the first measurements, samples were acidified with HCl and again measured to subtract phaeopigments from the chlorophylls to get concentration of Chl-A in mg/L following the JGOFS protocol (UNESCO, 1994).

SPM samples were filtered using pre-weighed Cellulose Acetate filters with 0.45 µm pore size, air dried and stored in aluminum foil (Lindell et al., 1999). Before weighting on a Sartorius R 200 D, filters were further dried in a 60-80° C oven for 2 hours and allowed to cool in a desiccator.

Surface reflectance measurements concurrent to each trawl were taken following the measurement methodology from Mobley (1999) and Fargion and Mueller (2000). An ASD FieldSpec Pro spectrometer was fitted with an 8° optic lens and set to measure raw digital numbers over an averaging of 50 rapid measurements. For each sampling location, a minimum of five reflectance measurement cycles were taken with the goal to collect as many cycles as possible during trawling. Each cycle consisted of a downwelling irradiance measurement over a white reference, an upwelling plus a sky radiance measurement both made following Mobley geometry (Mobley, 1999), and lastly a downwelling irradiance measurement to control for potential changes in lighting intensity conditions over the measurement cycle. Downwelling irradiance was measured over a 90% Spectralon® white reference panel. Processing of raw digital numbers into remote sensing reflectance is discussed further below.

Sediment samples were collected from nine beaches in order to serve as a validation dataset for the hydrodynamic and remote sensing models (sample locations are indicated in Figure 3 of the Results). Beach sample locations were selected so that three each of

low, medium and high river plume impact areas would be represented. Estimates of river impact were based on the hydrodynamic modelling accumulation map (more details below under Hydrodynamic model). At each location, samples were taken along the extreme high tide line, following protocols from Moreira et al. (2016) and Turra et al. (2014). Sampling was only conducted between high tide cycles. The extreme tide line was defined visually as the area with the largest accumulation of drift material, which was found to always be a clearly separate line to the last high tide line. Samples were taken at equal intervals along a 100 m transect line, where first 10 m were walked along the straight transect line and then turned at 90° for placement along the meandering drift line. Samples were taken with a 25 x 25 cm quadrat and sampled to a depth of 5 cm. Wet weight of the samples were recorded and then sieved over 1 mm mesh (matching model assumptions from the hydrodynamic model, more details below). Additionally, two 1 L bottles where filled with unsieved sand from the same transect line for later processing in the lab to convert the wet weight to dry weight.

Microplastic sample processing

Water samples were first fractionated into two size classes: 5 mm – 500 µm and 500 – 300 µm. To remove organic matter (which would disturb spectroscopic analysis) from the microplastic water samples, samples of the size class 500 – 300 µm were treated with enzymatic purification (Löder et al., 2017) and wet peroxide oxidation (Mausra et al., 2015). For the latter class (size 5 mm – 500 µm), samples with high organic content were treated solely with wet peroxide oxidation. All potential microplastic particles > 500 µm were visually pre-sorted, photographed and stored for further analysis with Attenuated Total Reflectance (ATR) Fourier Transform Infrared (FT-IR) spectroscopy. For a full-quantitative analysis of the fraction < 500 µm, samples were split. One subsample was filtered onto aluminum oxide membranes (Whatman Anodisc filters) and analyzed with Focal Plane Array (FPA) based Micro-FT-IR spectroscopy. The rest of the subsamples were filtered onto glass fiber filters (grade MN 85/90 BF) and analyzed with a newly developed remote sensing shortwave infrared (SWIR) spectroscopy methodology (Schmidt et al., in review) using a HySpex SWIR-320m-e sensor (Norsk Elektro Optikk AS).

Sediment samples along the 100 m transect were pooled. Samples were first processed by drying at 55°C, and then separated from inorganic material using a zinc chloride solution (density 1.6-1.8 g/cm³). The supernatant, which included both organic

material and potential polymer particles, was collected using a self-made mote spoon (stainless steel, mesh size < 1 mm), rinsed with 98% EtOH and transferred into glass petri dishes. All potential microplastic particles were visually separated from organic material under a stereomicroscope (Leica M50 with cold light source Leica KL 300 LED, Leica Microsystems), photographed (attached Olympus DP26 camera, 5 Megapixel, Olympus Corp.) and identified to polymer type using ATR FT-IR spectroscopy.

Spectra of all potential microplastic particles > 500 µm, from both water and sediment samples, were recorded with a Tensor 27 FT-IR spectrometer (Bruker Optik GmbH) from 8 co-added scans within a spectral range from 4,000 to 400 cm-1 and a spectral resolution of 8 cm^{-1}. Background scans were performed after every 10th measurement. Spectra were identified using the OPUS v7.5 software, correlating measured spectra against reference spectra from a custom in-house library (containing polymer spectra as well as spectra from both natural and lab materials used during sampling and processing, see Löder et al., 2015). Spectra of all potential microplastic particles < 500 µm were collected using the Tensor 27 FT-IR spectrometer further equipped with a Hyperion 3000 FT-IR microscope that had a 15x cassegrain objective and a 64x64 FPA detector mounted. Spectra were obtained in transmission mode and measurement settings were as published by Löder and Gerdts (2015). Obtained chemical images were analyzed with the ImageLab v2.26 software and the BayreuthParticleFinder tool (developed during the project together with Epina Software Lab GmbH), which automatically highlights potential polymer particles on the chemical image obtained from the FT-IR measurements of the filter. Given that polymer spectra can diverge, dependent on factors such as particle size, thickness, color, polymer additives or adsorbed chemicals, all automatically detected particles were again manually controlled afterwards.

Hydrodynamic model

Ocean current simulations of microplastic dispersal from the Po river into the North Adriatic were performed to cover from January 1st, 2015, to June 15th, 2016, ending to coincide with the field sampling in June 2016. A Lagrangian model was implemented to simulate the dispersion of virtual microplastic particles (VMP) due to currents obtained from the forecast of a state-of-the-art coupled ocean-waves hydrodynamical model (Carniel et al., 2016).

The model covers the northern Adriatic Sea with a horizontal resolution of 500 m and 12 vertical sigma layers. The hydrodynamical model (ROMS, Regional Ocean Modelling System; Haidvogel et al., 2008; http://myroms.org) was implemented in a couple version with a surface wave model (SWAN, Simulating WAves Nearshore model; Booij et al., 1999; http://swan.tudelft.nl) through the COAWST (Coupled-Ocean-Atmosphere-Wave-Sediment Transport Modeling System; Warner et al., 2010; Warner et al., 2008) system. Surface forcings were derived from COSMO-I7, a local implementation of the Lokal Model (Steppeler et al., 2003) developed in the framework of the COSMO Consortium (http://cosmo-model.org) and run by the Emilia Romagna Environmental Agency (Agenzia regionale per la prevenzione, l´ambiente e l´energia dell´Emilia-Romagna, Arpae-ER) Servizio Idro-Meteo-Clima (SIMC). Atmospheric forcing for the hydrodynamical model was obtained from an operational model run by the Università Politecnica delle Marche (UNIVPM) and the Regione Marche. The UNIVPM – Regione Marche model implementation was chosen because at the time of simulations it was the only freely available and operationally running forecast model with a high horizontal resolution. UNIVPM-Regione Marche model outputs were collected on a weekly/monthly basis and the first day of each forecast processed to function as current forcing for the Lagrangian model.

To study the dispersal patterns and pathways of microplastic particles released by the Po River, the Individual Based Model ICHTHYOP (Lett et al., 2008) was implemented. ICHTHYOP is a 3D Lagrangian model developed to study eggs and larval dispersion in the marine environment under the influence of currents and thermohaline water properties; it includes several biological features (such as larval growth and mortality) which in the case of the present work were not activated. In the model, the VMP behave as a Lagrangian drifter under the effect of horizontal/vertical advection and dispersion as well as buoyancy force due to the difference between the particle and surrounding water density. Particles were assigned a density of 0.91 g/mL to correspond with the averaged density of virgin polyethylene and polypropylene, which together account for over 48% of EU demand (PlasticsEurope, 2014) and represent the majority of sampled microplastic debris (Imhof et al., 2013; Zbyszewski and Corcoran, 2011). VMP were given the shape of sphere, which would only have influence within the model on sinking rates, with 1 mm diameter. ICHTHYOP was run offline using only the physical forcing from the outputs of the UNIVPM-Regione Marche COAWST simulations (i.e. 3D current field, water column temperature and salinity). For each time step, individual

displacement of particles was computed with a Runge-Kutta 4 integration scheme (Runge, 1895). Horizontal dispersion was included with a turbulent dissipation rate of $\epsilon=10\text{-}7 \text{ m}^2/\text{s}^3$, in agreement with turbulent kinetic energy observations in the Adriatic Sea (Falcieri et al., 2014). VMP were tracked for a total of 60 days, in excess of Adriatic particle half-life model estimates (Liubartseva et al., 2016) and drifter mean half-life observations (Poulain, 2001) of circa 40 days.

Simulations were based on the simplifying assumption of a constant concentration of 10 microplastic particles/m³ in the Po waters during the simulation period, as based upon previous observations from the Po river (van der Wal et al., 2015; Vianello et al., 2015). The number of VMP released was dynamically calculated using daily average streamflow measured at Pontelagoscuro (Figure 1) and the above-named concentration. Given that the river is represented as a point source inside the hydrodynamical model, VMP were released at the surface along straight 500 m lines located 250 m in front of each river mouth, with the goal being to mimic a direct discharge from the river itself. Po river mouths included Maestra, Pila, Tolle, Gnocca and Goro plus the Busa di Scirocco (given its presence in the hydrodynamic model). VMP were released over the entire simulation period at hourly intervals from all 6 locations and followed for a subsequent 60 days. The total number of VMP released at each mouth was defined following the water discharge distribution among the main branches of the Po River.

Once released, a VMP was considered beached if it passed closer than 250 m from the coastline. This distance was set by the model spatial resolution, and a more plausible parameterization of nearshore processes was not possible with the hydrodynamic model utilized. VMP were tagged with release date and river mouth, so that relative contribution from each river mouth could later be assessed. Once identified as beached, the VMP was removed from the dataset. VMP resuspension after beaching was not accounted for in the model, given the still existing amount of uncertainty surrounding this process (Hardesty et al., 2017; Zhang et al., 2017). A coastal reference grid was developed for displaying the distribution of beached particles along the Po Delta shore. To avoid artificial "shadowing" effects from corners of the hydrodynamic model grid cells located along the coastline, a smoothed grid was developed based purely on the coastline. This grid was created with ArcGIS v9.31 software by projecting the coastline 250 m offshore, separating this into 500 m segments and buffering each segment with 250 m, producing grid cells variable in both shape and surface but without sharp angles or abrupt changes in direction. After post processing, distribution maps of estimated accumulation could be

defined for each day up to the entire simulation period. Beach sediment sampling transect locations were placed as close as possible to the middle of the modeled accumulation pixel.

Near-range spectral measurements and remote sensing model

Near-range spectral measurements were used to build remote sensing spectral reflectance water parameter algorithms calibrated for different satellite platforms. First, raw digital number measurements from the spectroradiometer of downwelling irradiance plus upwelling and sky radiance were converted to irradiance, $E(z, \lambda)$ in units of W/(m² nm), and radiance, $L(z,\theta,\varphi,\lambda)$ in units of W/(m² sr nm), using the software package RS³ version 6.4.0 from ASD Inc. Radiance measurements were visually checked for abnormal behavior before being converted to remote sensing reflectance (R_{RS}) following the methodology detailed by Heim (2005):

$$R_{RS}(0+,\lambda) = \frac{L_{up}(0+,\lambda) - r_{wa} \times L_{sky}(\lambda)}{E_{down}(0+,\lambda)} \quad [sr^{-1}]$$

where $R_{RS}(0+,\lambda)$ is the remote sensing reflectance directly at the water surface (0+) for a given wavelength (λ), L_{up} is the above water (upwelling) radiance measurement, r_{wa} is the proportion of directly back-reflected skylight at the air-water interface (taken here to be 0.021, following Heim, 2005), L_{sky} the sky radiance, and E_{down} the downwelling irradiance measurement.

Four separate algorithms for spectral detection of SPM were considered: (i) Jørgensen (1999) based on the CZCS band 3 detecting in the range 540-560 nm, (ii) Dekker (1993) based on *in situ* spectrometer measurements at 706 nm, and two different SPOT-3 ratio-based algorithms from Doxaran et al. (2002) based on (iii) band 3 (780-890 nm) divided by band 1 (500-590 nm) and (iv) band 3 divided by band 2 (610-680 nm). The ASD R_{RS} dataset from the field campaign together with the *in situ* SPM measurements were used to calibrate each algorithm to the Po river water and for a given satellite sensor (Figure 2). All considered algorithms were noted to have the form of a linear regression, which in the original publication were fitted via the regression coefficients to a particular water body (e.g. a lake or river mouth). Our first step involved testing how the original algorithms, as they appeared in the publication, performed using the *in situ* R_{RS} dataset and SPM measurements. This was termed "Standard fit". When the original algorithm was fitted using reflectance data with a coarser spectral resolution,

as is the case for all algorithms except (ii), the *in situ* R_{RS} data would be transformed using the sensor-specific Spectral Response Function (SRF) to emulate the required bands of the satellite sensors that were used in the original publication. In a next step, the algorithms were calibrated specifically to the Po Delta system using ordinary least squares. This was termed the "Baseline fit", as this should be expected to represent the best performing form of each algorithm. It was necessary to introduce a log transform to the regressor in algorithms (i) and (ii) to avoid modelling of negative SPM values. In the final step, the algorithms were calibrated for each satellite sensor used to build the remote sensing timeseries (Landsat 8 and Sentinel-2). These were termed "Calibrated fit" for each satellite assessed. In order to accomplish this, the *in situ* R_{RS} data would be transformed using the respective SRF prior to running the regressions. All models were assessed for quality via the Root Mean Square Error (RMSE) as well as goodness of fit statistics following the methods of the Ocean Color Group (Campbell and O'Reilly, 2006). This allowed determination of the best calibrated algorithm for a particular satellite. Both the "Baseline" and "Calibrated" fits were also assessed for data overfitting using a leave-one-out cross-validation (LOOCV) technique (Michaelsen, 1987). LOOCV is particularly useful with low number of field sampling measurements or a lack of additional validation data (Brovelli et al., 2008; Peduzzi et al., 2012). Differences of an order of magnitude between the LOOCV-RMSE with the overall model RMSE can be used as an indication of model overfitting (Andersen et al., 2005).
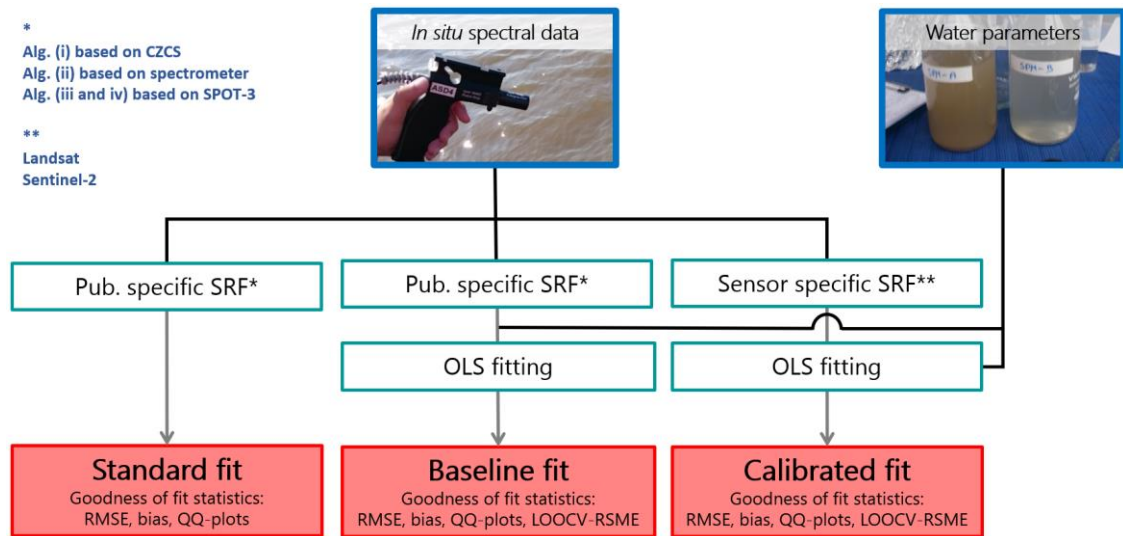
Figure 2: Flow diagram of water parameter algorithm calibration process. *In situ* spectral data (R_{RS}) were used to create three fits: standard, baseline and calibrated. Spectral data were transformed to either match the publication specific algorithm (Alg.) or the targeted satellite, both accomplished using the sensor specific Spectral Response Function (SRF). SRF used for each step are indicated with (*) for Baseline and (**) for Calibrated. Baseline and calibrated fits were created using ordinary least squares (OLS) fitting of transformed spectral data to *in situ* water parameter measurements. Fits were compared using root mean square error (RSME), bias, quantile-quantile (QQ) plots and, in the case of the baseline and calibrated fits, the leave-one-out cross-validation (LOOCV) RSME.

Landsat 8 (L8), a joint mission of the U.S. Geological Survey (USGS) and National Aeronautics and Space Administration (NASA), is equipped with two push-broom sensors, the Operational Land Imager (OLI) and the Thermal Infrared Sensor (TIRS), which provide multispectral images with 30 m spatial resolution at a revisit time of 8 days. The Po Delta study area is located in the overlap region between two Landsat flight paths, thus reducing the revisit time for this particular study. The European Space Agency (ESA) Sentinel-2 (S2) mission is a constellation of two identical satellites that are equipped with a push-broom MultiSpectral Instrument (MSI) sensor. S2 provides multispectral images with 10 m, 20 m and 60 m spatial resolution depending on the spectral band. S2 has a revisit time of up to 2-3 days at midlatitudes. Useable images from L8 and S2 acquired between January 1st, 2015, and June 30th, 2016 were compiled. Other platforms with coarser image spatial resolution (> 375 m) but proving daily (MODIS) to 3-day (MERIS) acquisitions with much greater Signal-to-Noise Ratio (SNR) were considered but not implemented given that our goal was to capture the fine river plume structure as close to the coastline as possible.

Different atmospheric correction algorithms were tested to minimize the introduction of artifacts to the bands needed for detection of various water parameters. Algorithms

were compared for each sensor through the *in situ* R_{RS} spectrometer measurements, taken within 2 hours of the satellite overpass, together with the corrected satellite R_{RS} from the pixel corresponding to the same location. The atmospheric correction algorithms considered were ATCOR (ReSe Applications LLC), Sen2Cor (ESA, Science Toolbox Exploration Platform – STEP) and ACOLITE (Vanhellemont and Ruddick, 2015, 2014). ATCOR and Sen2Cor depend on the dark-pixel assumption, the former accomplishing this using a band in the near-infrared (NIR) and the latter using a band in the short-wave infrared (SWIR). ACOLITE is specially designed for turbid water remote sensing applications and can be implemented to use only SWIR bands.

The L8 and S2 acquisitions were processed with a hierarchical object-based image analysis (OBIA) developed with eCognition software (Trimble Navigation Ltd.) to remove land, clouds, boats, white caps and breaking waves. The masked images were then used to create SPM concentration maps, which showed how the river plume was spreading into the surface coastal waters over the examined time period.

For each acquisition date, non-coastline pixels were masked and the remaining utilized as the basis for creating the coastline exposure map. This was accomplished by converting pixel values to a similarity ratio using the average SPM concentration from all five river mouths for that acquisition date. The goal was to display how similar a given coastline pixel was to a pure river water pixel, which was then used to indicate influence from river plume waters along the coastline. Data were binned into hexagons to allow for combination of images with differing geo-registration as well as spatial resolution, at diameters of both 30 m and 100 m. This was accomplished using the "hexbin" package within the R software package (R Core Team, 2016). The first diameter represents the minimum allowable resolution and the second to match the sediment sampling scheme as well as easier visualization of the entire Po Delta coastline. Gaps in the dataset, produced through masking areas such as cloud cover or breaking waves, were filled in the time series using a combination of Nearest Neighbor Filtering and temporal linear interpolation. This was done again in R using the packages "raster", "rgdal", "rgeos", "sp" and "spacetime". The timeseries was then summed to create a composite image of river plume influence along the Po Delta coastline for the entire modelled time period.

Po river level gauge measurements were obtained for the modelling period from Arpae-ER, taken at Pontelagoscuro. Land-based wind measurements are publicly available from the Italian National Institute for Environmental Protection and Research

(Istituto Superiore per la Protezione e la Ricerca Ambientale, ISPRA) and were downloaded for the modelling period from Ravenna, the closest wind station to the Po Delta.

Model validation

SPM values between L8 and S2 images were compared using standardized differences to check for any inherent bias between the different sensors. Modelled accumulation values from both the remote sensing time series as well as the ocean current particle tracking were compared to beach sediment microplastic concentrations to assess model validity as well as identify weaknesses and strengths of each modelling method. Comparisons were made using both Pearson's Correlation r as well as Spearman's Rank Coefficient ρ. All calculations were carried out using R software. Model maps were also compared to one another by unit-base normalizing each map and then comparing difference values at regular latitudinal intervals along the coastline.

Results

Water parameter sampling

Water parameter field measurements are presented in Table 1. Chl-A measurements fell within a range expected for a productive river mouth system, and SPM values covered a moderate range (Arpae-ER monitoring measurements of SPM from Pontelagoscuro for the time period January 2015 to June 2016 ranged from 12-372 mg/L). Secchi depth measurements only reached a maximum of 163 cm, all located along the outer edge of the river plume. Sea surface salinity (SSS) was found at the time of sampling to be a much better indicator of river water presence, ranging from 0.1 up to 31.9 psu, than sea surface temperature (SST), which only covered a range from 21.5 up to 26° C.

Table 1: Measured water parameters during the field campaign. Chlorophyll-A (Chl-A) and suspended particulate matter (SPM) reported in mg/L, Secchi depth average from before and after trawl in cm, sea surface temperature (SST) in ° C, and sea surface salinity (SSS) in practical salinity units (psu).

	Chl-A (mg/L)	SPM (mg/L)	Secchi (cm)	SST (° C)	SSS (psu)
Mean / Median	0.011 / 0.009	30.2 / 21.1	67 / 51	22.60 / 22.53	10.7 / 4.1
Standard deviation	0.008	29.4	36	0.93	12.0
Maximum	0.043	127.9	163	25.99	31.9
Minimum	0.005	7.7	29	21.45	0.1

Microplastic sampling

Water microplastic samples analyzed by ATR FT-IR and SWIR spectroscopy ranged from 1-75.73 particles/m³ (Figure 3), with the highest concentrations being found along the outer river plume edge, within the main arm of the river (Po di Pila) and the side channel Busa di Tramontana. The Maistra and central Tolle river mouths both had very low concentrations, < 4 particles/m³. Repeated measures from a particular river section, such as where Po di Tolle separates from Po di Pila or where Po di Tolle splits into 3 channels, indicates large variability from one sampling time to another.

The sediment microplastic samples (Figure 3) ranged from 0.5-78.8 particles per dry weight (DW) kg. The highest measurement by far was on the northernmost beach, Caleri, where a total of 3,080 microplastic particles were identified for the entire sample (Table 2). Polystyrene (PS), acrylonitrile butadiene styrene (ABS) and styrene acrylonitrile (SAN) were found to have similar spectral signatures, thus were pooled into a group called styrene polymers to avoid potential confusion between these types. The same was true for the polymer types ethylene vinyl alcohol (EVOH) and ethylene-vinyl acetate (EVA). Polyethylene (PE), polypropylene (PP) and the styrene polymer group made up more than 97% of all particles sampled on 6 beaches (Boccasette, Pila North 1, Pila South, Allagamento, Barricata and Goro). The remaining three beaches had either an increased contribution from EVOH/EVA or, in the case of Pila North 2, elevated contributions for the polymer types polyamide (PA) and polyethylene terephthalate (PET).
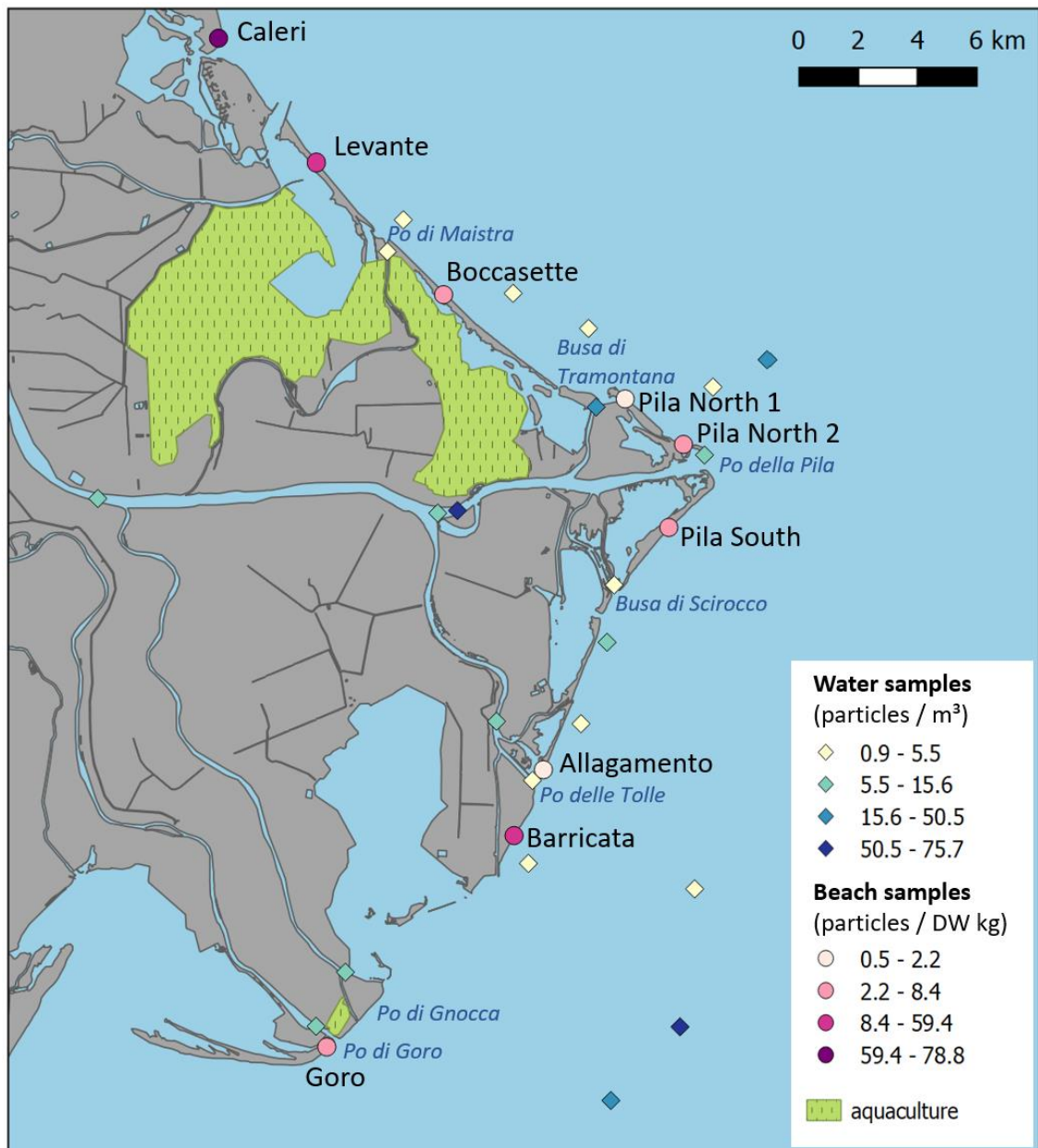
Figure 3: Overview of water microplastic samples (diamonds, blue scale) and sediment microplastic samples (circles, pink scale) collected during the June 2016 field campaign. A total of 24 water locations and 9 beach locations were sampled, only beach locations are labelled (black text). Water samples are reported as particles/m³ while sediment samples are reported as particles per dry weight kg (DW kg). River mouths are labelled in dark blue and aquaculture areas within lagoons are indicated.

Table 2: Sediment microplastic overview for all 9 beaches sampled, listed north to south. Percent contribution from each plastic type identified is listed: PE polyethylene, PP polypropylene, PS polystyrene ([1] also includes ABS acrylonitrile butadiene styrene and SAN styrene acrylonitrile), PA polyamide, EV[2] accounts for EVOH ethylene vinyl alcohol and EVA ethylene vinyl acetate, PEST polyester, PET polyethylene terephthalate, PVC polyvinyl chloride, PUR polyurethane, PVAL polyvinyl alcohol, SBR styrene butadiene rubber, C/U accounts for either composite particles or unknown plastic types. Total microplastic particles found as well as particles/DW kg is also indicated for each beach sampled.

Beach	% contribution												Tot. part.	part./ DW kg
	PE	PP	PS[1]	PA	EV[2]	PEST	PET	PVC	PUR	PVAL	SBR	C/U		
Caleri	45.0	8.6	28.0	< 1	18.0	< 1	< 1	< 1	< 1	0	0	< 1	3080	78.8
Levante	62.2	14.6	16.4	< 1	5.7	< 1	< 1	< 1	< 1	< 1	< 1	< 1	2032	59.4
Boccasette	42.9	13.2	42.9	0	< 1	0	0	0	0	0	0	< 1	182	3.9
Pila North 1	27.0	14.8	54.8	0	< 1	0	< 1	0	0	0	0	< 1	115	2.2
Pila North 2	60.2	9.7	20.4	1.9	0	< 1	4.9	0	< 1	0	0	< 1	103	3.6
Pila South	45.7	18.9	34.1	0	1.4	0	0	0	0	0	0	0	440	8.4
Allagamento	10.0	5.0	85.0	0	0	0	0	0	0	0	0	0	20	0.5
Barricata	19.2	13.8	66.3	< 1	< 1	0	0	0	0	0	0	0	652	14.3
Goro	52.0	19.0	27.8	0	< 1	0	0	0	0	0	0	< 1	248	5.2

Ocean current model accumulation

Comparing Po average daily outflow with the total daily beached VMP (Figure 4), a loose connection between the streamflow (hence the number of particles released in the model) and the beached VMP was evident, as could be expected. High beaching rates in April, July and October 2015 were observed to follow high river discharge events (which as part of the model design, positively correlate with the number of VMP released), but this pattern was not always present. Beaching peaks in August 2015 and January 2016 did not correlate with high river discharge events, hinting that beaching is not only driven by the amount of released VMP (which was intrinsically associated with high river discharge within the model) but also by surface currents.
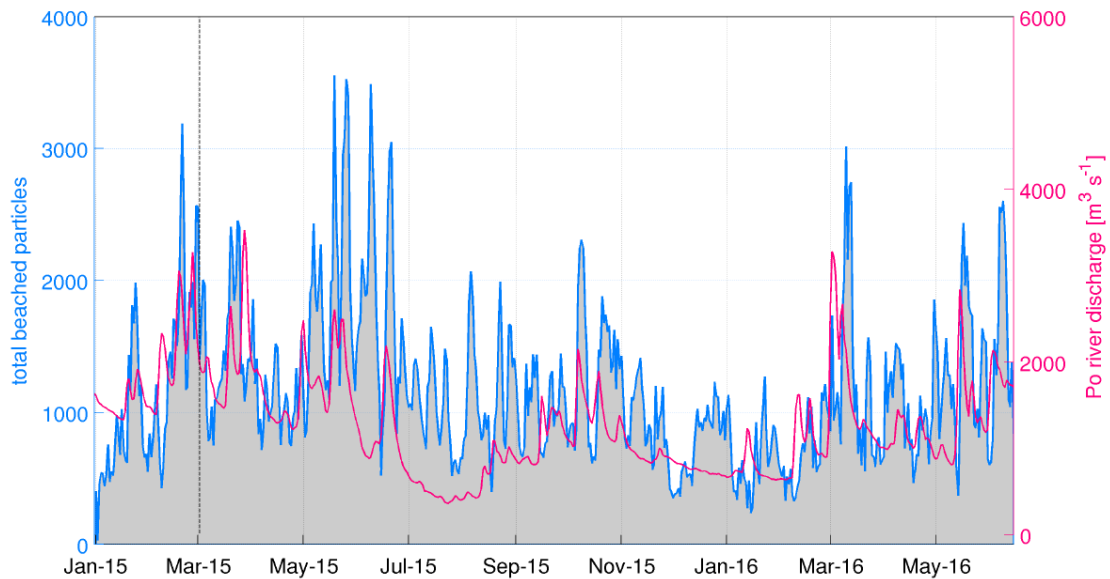
Figure 4: Average daily outflow of the Po River taken at Pontelagoscuro (magenta line, right axis) compared with average daily total of beached virtual microplastic particles (VMP, blue line, left axis). VMP were tracked in the model a total of 60 days, the first day that satisfies this condition is indicated by the dashed black line.

Of all VMP released, only 18% were found to beach during the entire modelling time period. The ratio of released-to-beached VMPs for each mouth was highly variable. Po della Pila, Busa di Scirocco and Po di Gnocca river mouths were found to beach less than 10% of all VMP released. Po di Maistra and delle Tolle were found to beach between one fourth and one fifth (26% and 19% respectively) of their released VPM. By far the highest rate of beaching was determined for the southernmost river mouth, Po di Goro, with 94% of all released VPM being found to have beached. Figure 5 depicts the daily percentage of beached VMP per river mouth after release. In Figure 5a, the percentage of beached VPM from a particular river mouth are compared with the total VPM beached for each model run day. The northern river mouths (Maistra, Pila, Scirocco, Tolle and Gnocca) display similar behavior in that the majority of beaching occurs within the first 3 days and was then followed by a sudden drop to low values, remaining close to zero after about 10 days. The Po di Goro mouth, on the other hand, also displayed high beaching rates in the first 5 days but thereafter a more gradual decline, reaching zero levels after circa 20 days. Thus, VMP released by the Po di Goro mouth were able to reach the coastline for a longer period of time (up to 30 days after release, as shown in panel a) and thus had higher probability to be beached than VMP released from the other mouths. Figure 5b depicts the percentage of beached VMP per river mouth as compared to the total VMP released by the same river mouth. Here the much larger percentage of VPM to become beached from the total released by the Po di

Goro mouth was quite clear, with over 34% of all VMP released from the river mouth being beached within the first three model run days. The elevated beaching rates of the Po di Maistra and delle Tolle were also more clearly depicted.
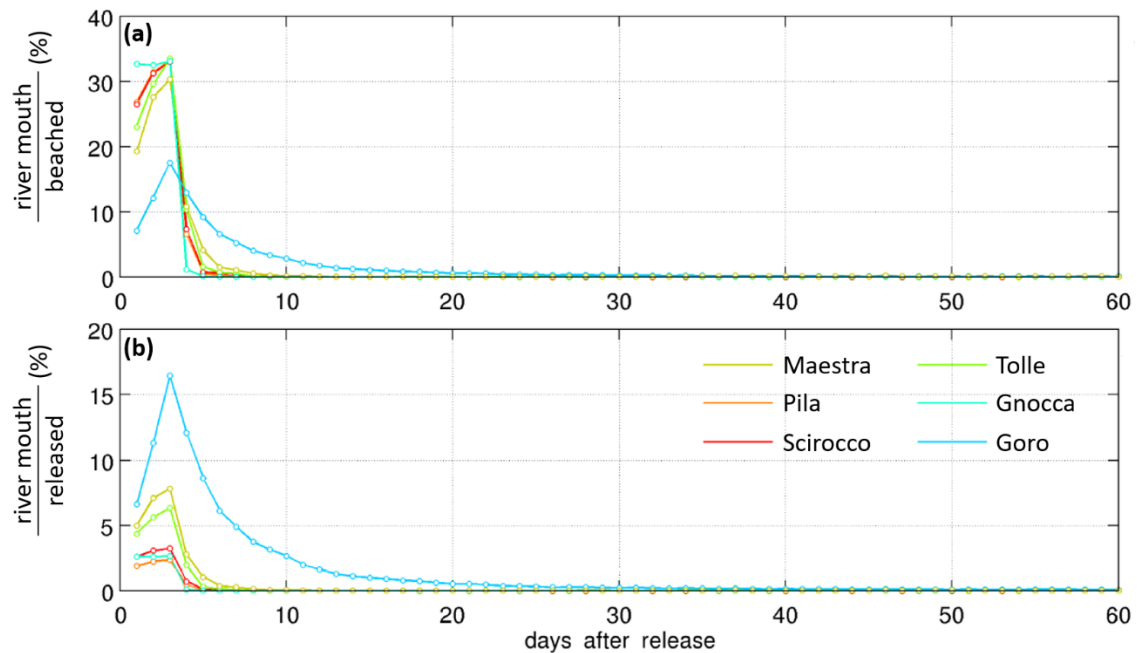
Figure 5: Percent beached virtual microplastic particles (VMP) from each river mouth in comparison to (a) total daily beached VMP and (b) total daily released VMP. Days after release are depicted along the horizontal axis. Release events after April 15th, 2016, are not included since these were run for less than 60 days.

The ocean current model beaching accumulation map for the entire simulation period is shown in Figure 6. VMP release points in front of river mouths are indicated by the red arrows. Higher beached VMP accumulation was evident locally around each of the river mouth release points (Figure 6a), as well as along the southern coast of the Po Delta and extending south along the coast after Lido di Volano. The highest accumulation areas were modelled to be just south of the Po della Pila river mouth, and near to the Po di Gnocca and di Goro river mouths. The individual distribution from each river mouth is depicted in Figure 6b, showing that the VMP beaching rates for all mouths remain quite local except for the southernmost Po di Goro mouth.

86
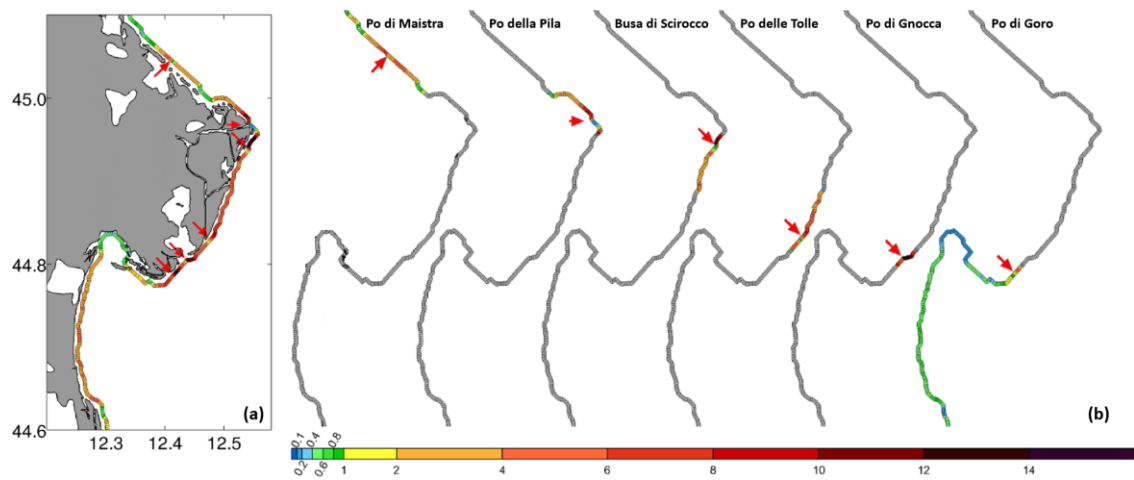
Figure 6: (a) Distribution map for VMP beaching accumulation over the entire 1.5-year simulation period, VMP release locations in front of river mouths are indicated by the red arrows. Color scale indicates ten times the percentage of total particles beached. (b) Beached VMP percentage for each river mouth separately displayed, color scale indicates percentage of total VMP beached from that particular river mouth.

Remote sensing model accumulation

Spectral reflectance R_{RS} measurements from the spectroradiometer are shown in Figure 7, organized into locations with either "high" or "low" Chl-A and SPM levels. High was defined as all measurements above the median, low all those below. One and two standard deviations (68% and 95% respectively) around the median curve are also displayed in Figure 7, indicating variation in reflectance values over the different types of water. As expected, a decrease in R_{RS} around 440 nm with low SPM and high Chl-A (lower left plot in Figure 7) was observed, which correlates to a known absorption peak of chlorophyll. Along the same curve, the augmented minimum at 665 nm was assumed to correspond to a second Chl-A absorption peak and the following maximum close to 700 nm likely to be the product of chlorophyll fluorescence. The low Chl-A, high SPM curve (upper right plot in Figure 7) showed no decrease around 440 nm, increased reflectance in all bands from 550-700 nm and augmentation of the reflectance maximum near 800 nm, all of which are similar to patterns documented by Doxaran et al. (2002) for the high turbidity waters from the Gironde river, France. These R_{RS} measurements of samples with low Chl-A and high SPM content were also found to have the least variation, as indicated by the small deviations of the 1- and 2-σ curves from the median line. In the case of high Chl-A together with high SPM, variance among individual R_{RS} measurements was found to be the highest (lower right plot in Figure 7). Reflectance between 600-700 nm was even more elevated relative to the maximum around 575 nm,

but many of the Chl-A spectral signature features (such as a decrease in R_{RS} at 440 nm and the min/max curve between 650-700 nm) were not as clearly evident.
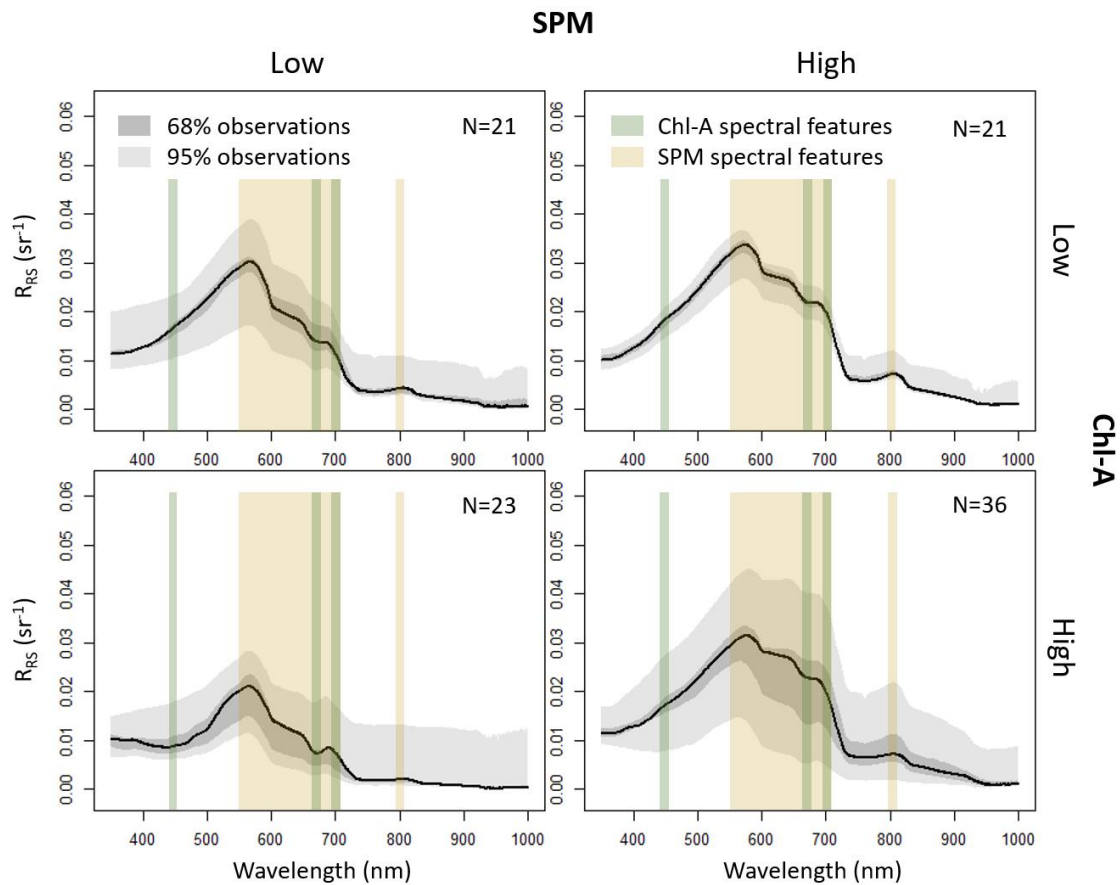
Figure 7: All spectral remote sensing reflectance (R_{RS}) data, organized by relative *in situ* chlorophyll-A (Chl-A) and suspended particulate matter (SPM) measurements. Grouped into "high" and "low" based on median of all Chl-A or SPM measurements, respectively. Number of individual reflectance measurement contributing to each curve is indicated (N), and percent of all observations at one standard deviation (1-σ, 68%, dark gray) or two (2-σ, 95%, light gray) is also indicated. Median R_{RS} is indicated by a black line. Spectral features characteristic of Chl-A and SPM which are discussed in the text are indicated in green and tan bars, respectively.

An example of improved model fit to the data during the calibration/validation process is presented in Figure 8. The Dekker algorithm is based on the expected elevation of the R_{RS} spectrum around 700 nm, as also observed from our data in the Figure 7 plots with high SPM. A better fit to the measured values was observed, as is evident through the reduction of the RMSE and bias by an order of magnitude. The LOOCV-RMSE was found to be less than an order of magnitude different, suggesting that model overfitting is not an issue despite low sample numbers. Results of all four assessed SPM algorithms are presented in Table 3, where the algorithm basis is listed along with the fitted algorithm and model fit statistics (RMSE, LOOCV-RMSE, bias). Model fit statistics were found to be reduced by an order of magnitude through the calibration/validation for both the Jørgensen and Dekker algorithms, only slight improvement was achieved for

one of the band-ratio Doxaran algorithms while the other was found to be a non-significant predictor for the Po River water. An exponential relationship was determined preferential for the Jørgensen and Dekker algorithms to avoid modelling of negative values. Model fit statistics were relatively unaffected by fitting to coarser spectral resolution satellite sensor specific bands. Given the observed overlap of the Chl-A reflectance peak at 560 nm with the SPM signal saturation between 550-700 nm (Figure 7), the Dekker algorithm was selected as preferable to the Jørgensen algorithm. Furthermore, the Dekker algorithm was found to be a significant predictor for both L8 as well as S2 data.
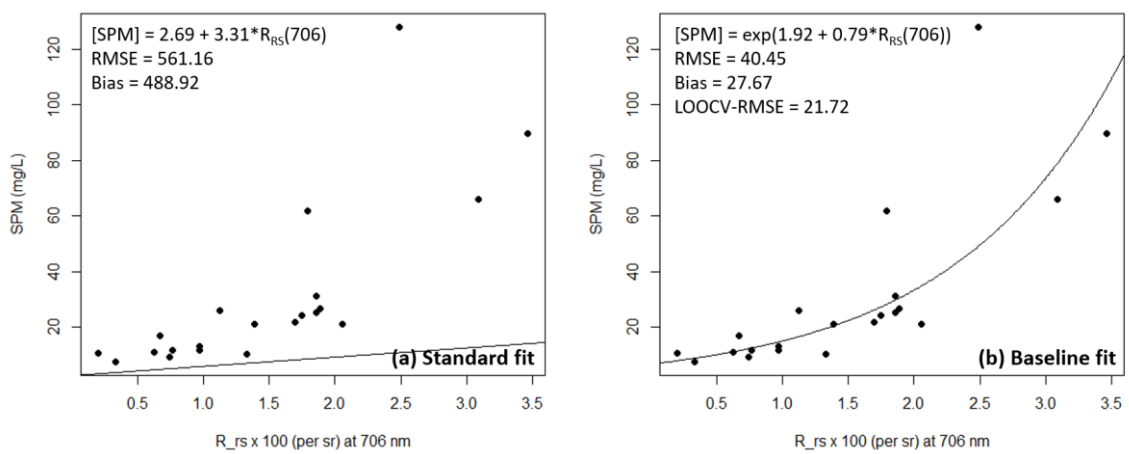

Figure 8: Comparison (a) published SPM Dekker algorithm with (b) baseline fit algorithm. Scaled spectral signal at 706 nm wavelength (R_{RS} in sr^{-1}) is depicted along the horizontal axis, measured *in situ* SPM (mg/L) along the vertical axis, and modelled values with the black line. *In situ* measured values are the black points. Algorithm is listed in upper left of each plot, along with model root mean square error (RMSE), bias and leave-one-out cross-validation RMSE (LOOCV-RMSE, right plot only).

Table 3: Calibrated algorithms for suspended particulate matter (SPM). Algorithm spectral basis and publication is indicated in the first column, standard fit algorithm in the second column together with model fit statistics: root mean square error (RMSE) and bias. Baseline and satellite specific algorithms are listed in the following columns, with fitted algorithm listed followed by fit statistics (RMSE, leave-one-out cross-validation RMSE, bias) in parentheses. Relationships that were found to be non-significant ($\alpha \geq 0.05$) during fitting are indicated with N/A. The satellite sensor band used is also indicated, e.g. Landsat 8 band 3 centered at 560 nm is indicated by b3$_{560}$.

Algorithm basis	Standard fit	Baseline fit	Landsat 8	Sentinel-2
Band at 555 nm (Jørgensen, 1999)	0.09+56.19*b$_{555}$ (154.91; 148.22)	exp(1.47+0.60*b$_{555}$) (40.66; 29.98; 27.67)	exp(1.46+0.60*b3$_{560}$) (40.64; 29.35; 27.67)	exp(1.45+0.60*b3$_{561}$) (40.65; 29.63; 27.67)
Band at 706 nm (Dekker, 1993)	2.69+3.31*b$_{706}$ (561.16; 488.92)	exp(1.92+0.79*b$_{706}$) (40.45; 21.72; 27.67)	exp(1.82+0.66*b4$_{655}$) (40.50; 22.91; 27.67)	exp(1.91+0.78*b5$_{706}$) (40.45; 21.65; 27.67)
SPOT bands XS3 (cen. 835 nm) and XS1 (cen. 545 nm) (Doxaran et al., 2002)	exp(3.01+3.13* XS3$_{835}$/XS1$_{545}$) (27.37; 21.06)	exp(2.37+3.25* XS3$_{835}$/XS1$_{545}$) (26.29; 29.62; 16.43)	N/A	exp(2.39+3.57* b8$_{843}$/b3$_{561}$) (26.42; 29.79; 16.49)
SPOT bands XS3 (cen. 835 nm) and XS2 (cen. 645 nm) (Doxaran et al., 2002)	exp(2.56+5.31* XS3$_{835}$/XS2$_{645}$) (83.15; 50.92)	N/A	N/A	N/A

A total of 26 useable images from L8 and S2 (12 and 14 respectively) were compiled covering the modelling time period (Figure 9). Useable images from two out of the total eighteen considered months could not be obtained. River level and wind speed, overlain with wind regimes, are also shown in Figure 9. Peaks in river outflow were observed during the spring months, with secondary peaks occurring during fall. The highest observed peaks in daily wind speed occurred in January, March and November 2015, which all corresponded to northeast (Bora) wind events. Scirocco (southeast wind) events were observed to have less strong wind speeds. Half of all Mistral events were found to occur either preceding or following other wind events. Both Mistral and Scirocco events were found to have occurred less frequently than Bora events. Of the compiled useable satellite images, five instances each of Bora/low discharge and Mistral/low discharge were captured, as well as three instances of Scirocco/high discharge and one instance of Bora/high discharge conditions.

Satellite	Jan	Feb	Mar	Apr	May	Jun	Jul	Aug	Sep	Oct	Nov	Dec	Jan	Feb	Mar	Apr	May	Jun	Total
L8	1	0	1	2	1	0	0	0	1	1	1	0	1	0	1	1	0	1	12
S2A	-	-	-	-	-	-	1	2	3	1	0	1	1	1	1	0	1	2	14
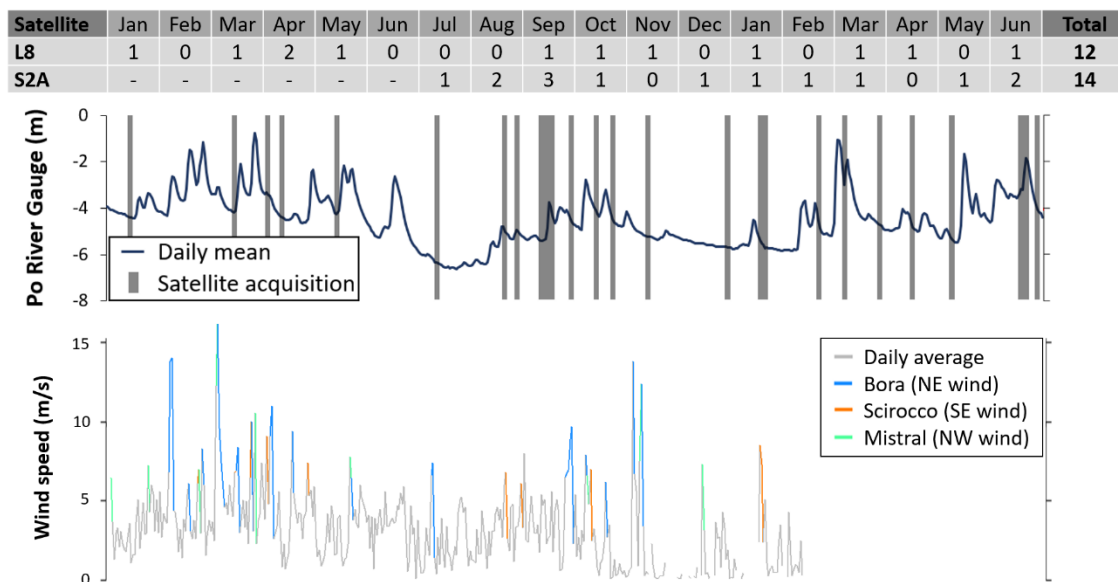
Figure 9: Temporal satellite image coverage from January 2015 to June 2016, together with daily river level at Pontelagoscuro (Po River gauge, dark blue line) and daily wind speed measured at Ravenna (wind speed, gray line). Total images from each satellite (Sentinel-2: S2; Landsat 8: L8) are listed in the table as well as depicted by gray bars overlain on the river gauge timeseries. S2 images first became available July 2015. Wind regimes (here defined as daily wind > 6 m/s) are indicated with colored lines in the bottom plot: Bora (NE winds, in light blue), Scirocco (SE winds, in orange) and Mistral (NW winds, in green). River gauge data provided by Arpae-ER. Wind data were provided by ISPRA, gaps are due to the anemometer malfunction during the latter portion of study period.

An S2 image acquired on June 15, 2016, was taken the same day as *in situ* sampling, which allowed optimal comparison of R_{RS} measurements made by spectroradiometer from the boat with atmospherically corrected R_{RS} values from the satellite. Three *in situ* measurements could be achieved within two hours of the S2 overpass, with one

measurement from the middle of the Po della Pila mouth being taken directly following the satellite acquisition. The image was corrected separately using ATCOR, Sen2Cor and ACOLITE, and the pixel value from the same location as *in situ* sampling was compared with *in situ* R_{RS} measurements. Variation of the eight neighboring atmospherically corrected pixels was also considered. No L8 images could be acquired concurrent to *in situ* field sampling, thus comparisons with ATCOR and ACOLITE corrected pixel values had to be completed using *in situ* measurements from two days prior and one day posterior to the satellite acquisition. All atmospherically corrected R_{RS} values were found to capture the same overall spectral signature characteristics observed from the *in situ* R_{RS} measurements, performing quite well for the offshore clearer Adriatic water sampling location. Underestimation of R_{RS} values were observed for the highly turbid Po della Pila waters. For the purposes of this study, Sen2Cor was determined to be the optimal atmospheric correction algorithm for S2 data and ACOLITE for L8 data.

Examples from satellite image masking and implementation of the calibrated Dekker SPM algorithm are shown in Figure 10. High/low river discharge was classified as daily average river gauge levels over/below the median gauge level for the entire modelling period (-4.6 m). From the acquisition with high discharge, the strong effect of a wind event on river water transportation was quite evident. In the case of high discharge together with southeasterly Scirocco winds ((Figure 10b), plume water can be observed being pushed northward of the Po di Pila mouth. With northwesterly Mistral winds (Figure 10c), the plume shape appears to be more heavily influenced by river outflow, with high river discharge producing a plume extending further into the Adriatic. But in the case of northeasterly Bora winds (Figure 10a), the high discharge plume was kept closer to the coastline while primarily spreading high SPM waters towards the south. A somewhat different pattern was observed for the acquisitions concurrent to low discharge. The Bora wind event on September 29, 2015, was observed to again retain the plume close to the southern coastline (Figure 10e). Plume form under low discharge and Scirocco wind was only demonstrated with one acquisition (Figure 10f). SPM signal from the river water on this date were quite low, making the plume difficult to detect, but through utilizing a different stretch the plume could be observed to extend further into the Adriatic. The Mistral wind together with low discharge (Figure 10g) was observed to retain river plume close to the coastline, but much smaller than was observed with high discharge.
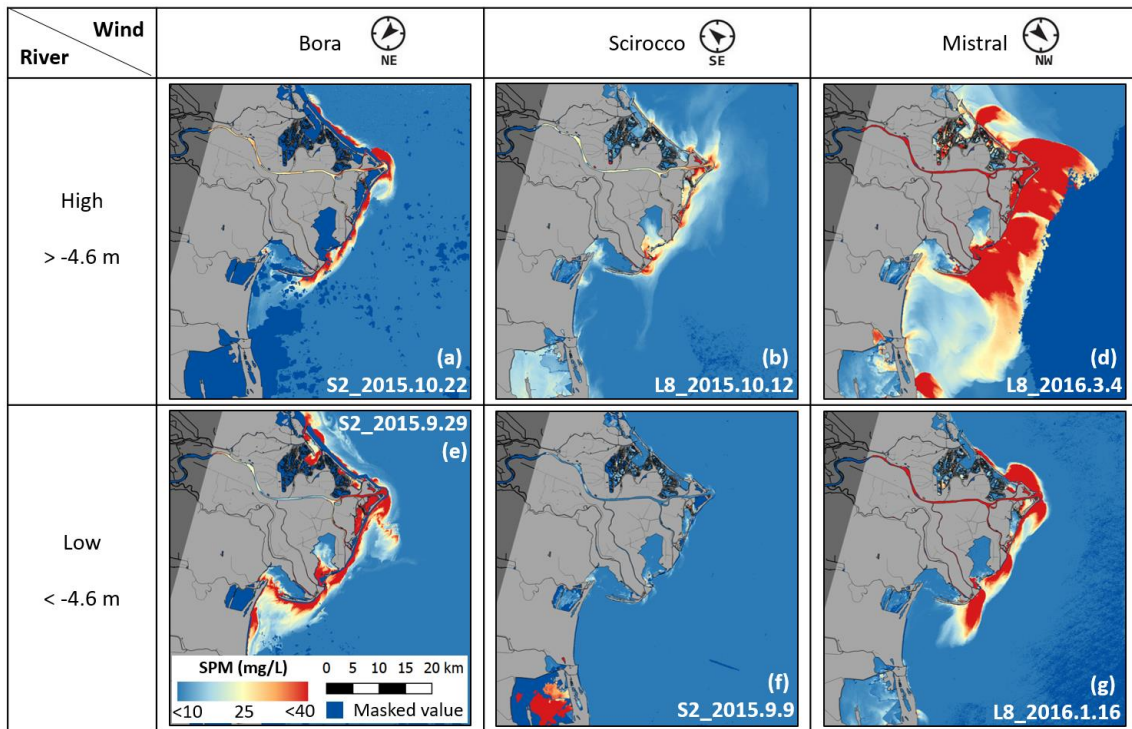
Figure 10: Combined effect of different wind regimes (Bora, Scirocco or Mistral) with different river discharge conditions on river plume transportation along the Western Adriatic. River discharge is termed "high" (panels a,b,c) or "low" (panels e,f,g) depending on daily discharge relative to the median water level (-4.6 m) over the entire simulation period. Wind events were classified based on wind direction (indicated by wind compass in each column, pointing in the direction that wind is blowing) and strength (excess of 6 m/s winds). Suspended Particulate Matter (SPM) values, ranging from low in blue to high in red, depict river plume shape. Masked pixels are depicted in dark blue, land in light gray (outside of area of interest in dark gray).

Results of the remote sensing composite hexagon binning processing are presented in Figure 11, with red indicating coastal areas of high river water influence and green areas with less. Strong river water influence was detected around all five river mouths (Maistra, Pila, northern and central Tolle, Gnocca and Goro) as well as the Busa di Tramontana and di Scirocco. The southern arm of the Po delle Tolle was observed to have a lesser influence, while the northern section of coastline between river mouths presented very low rates of river water influence. Coastline sections near to the Po della Pila mouth and southward were observed to have higher rates, with the highest influence evidently being along the coastal section just north of Po della Pila. An area of very high river water influence (red) was detected between Po della Pila and Busa di Tramontana, which corresponds to an additional river mouth flowing out from the lagoon that was first observed during the field campaign.
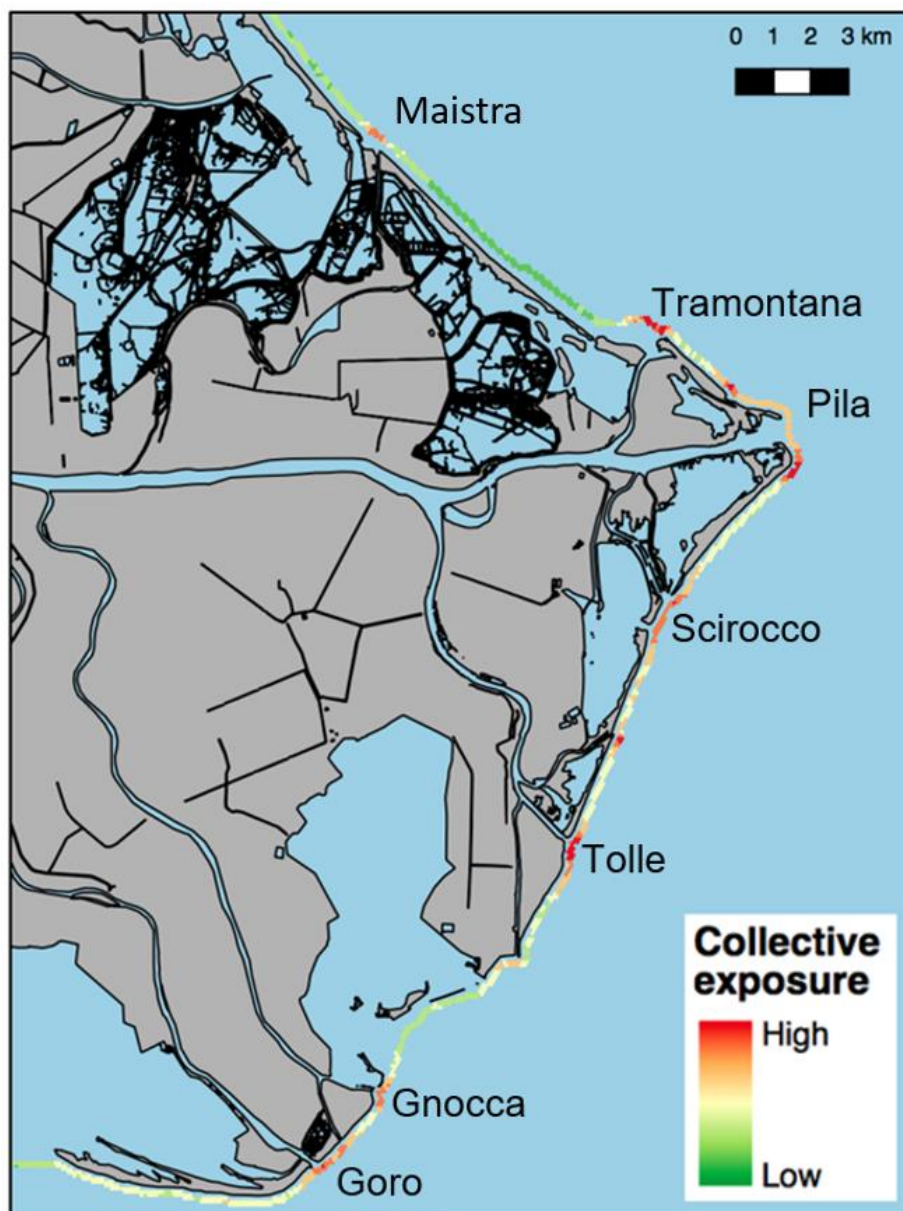
Figure 11: Composite hexagon (100 m) map of SPM time series, colored by summed daily similarity values to river water. High rates of river plume influence (red) are observed at all five major river mouths and the two Busa, Tramontana and Scirocco, around Po di Pila. Low river plume influence (green) can be observed along the northern coast of the delta.

Model validation results

Standard difference comparison between L8 and S2 images revealed a slight sensor bias, in that detected L8 SPM values tended to be slightly (< 2 mg/L) less than detected S2 SPM values. This amount represented less than 2% of the SPM range measured in the field (Table 1) and was thus taken to be negligible. No significant relationship was found when comparing the *in situ* beach sediment microplastic concentrations to the nearest hydrodynamic model grid cell ($p > 0.10$ for Pearson's r and Spearman's ρ). Removal of beach locations that were under more influence from beach tourism and nearby

aquaculture (namely Caleri, Levante, Boccasette and Barricata) resulted in a stronger correlation: Pearson's r = 0.79 and Spearman's ρ = 0.80 (p < 0.07 in both cases). Comparison of *in situ* beach sediment microplastic concentrations with the nearest remote sensing model 30 m hexagon revealed a moderate negative correlation, with Pearson's r = -0.58 (p = 0.05). No significant correlation was found at the 100 m hexagon resolution. Focusing the comparison to beaches with lesser influence from beach tourism and nearby aquaculture did not reveal an improved correlation. Removal of the styrene polymer group from the *in situ* beach sediment microplastic concentrations was also considered, given that styrene polymers is both highly buoyant in its foamed form and thus very susceptible to windage during transport as well as potential higher susceptibility for further particle fractionation during beach sediment lab processing. Despite these considerations, removal of one of the top three contributing polymer groups to *in situ* beach sediment microplastic concentrations was not found to provide any further model improvement.

Comparison between the two models is depicted in Figure 12, where the normalized remote sensing exposure map is shows directly next to the hydrodynamic model accumulation map (Figure 12a). General tendencies for lower normalized values along the coastline north of Pila di Maistra and south of Lido di Volano were similar between the two model results. Strong river mouth signal from Pila, the southern Tolle, Gnocca and Goro were also evident in both maps. Dissimilates were most evident for the river mouths Maistra, Tramontana and Scirocco, where a strong signal was registered by the remote sensing model but not by the hydrodynamic model. In Figure 12b, the difference comparison of the normalized values (hydrodynamic normalized values, HD_{norm}, minus remote sensing normalized values, RS_{norm}) are displayed as a histogram aligned along the latitudinal axis. The comparison was made along the full overlap extent of both maps and the distribution is indicated in Figure 12b with the gray shaded areas (one and two standard deviations). A slight positive bias is observed, meaning that the HD_{norm} values tend to be higher than the RS_{norm} values, with 95% of all values lying between -0.07 and 0.49. Areas of exceptional variation, indicated by bars lying outside the shaded gray area, were notably the coastline located between Pila and Scirocco and between the northern and central Tolle mouths.
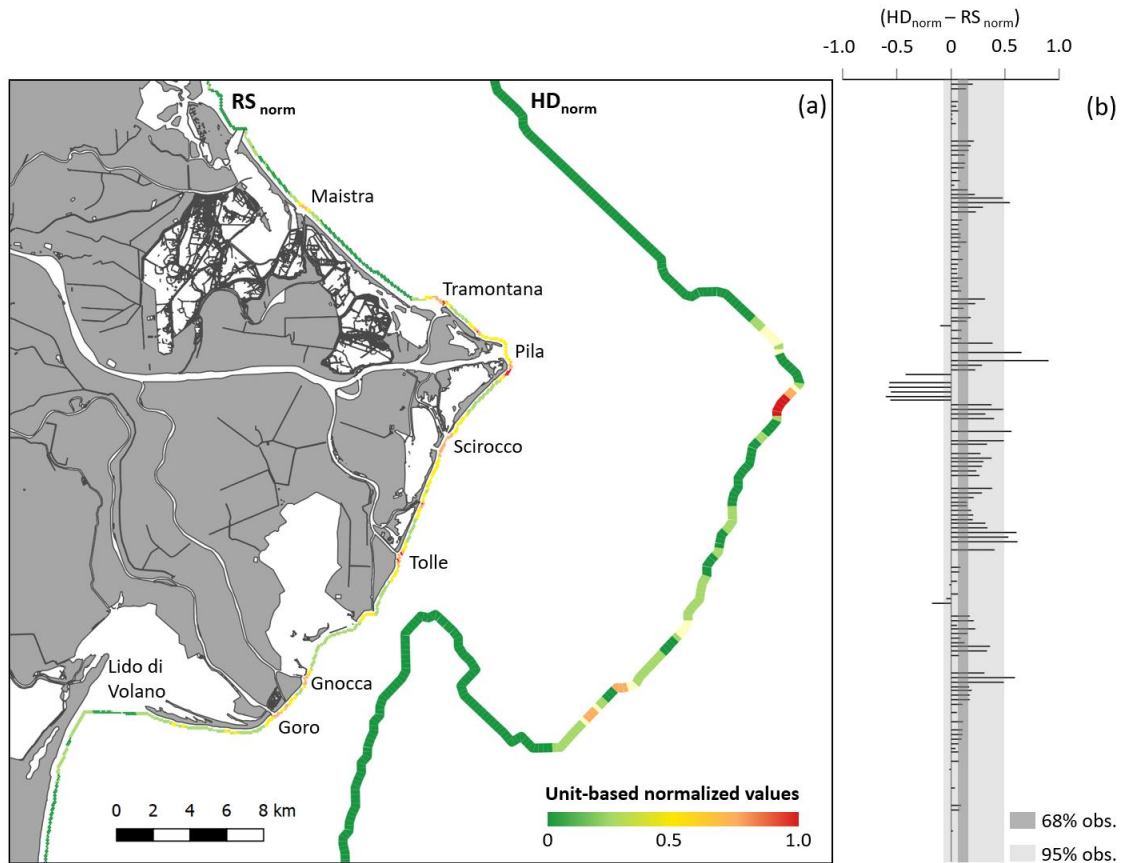
Figure 12: (a) Remote sensing hexagon-binned (100 m) exposure map (left) next to hydrodynamic model accumulation map (right), both datasets have been unit-based normalized (green low to red high). (b) Difference normalized hydrodynamic model (HD_{norm}) to normalized remote sensing model (RS_{norm}), aligned along the latitudinal axis. Percentage all observations (obs.) at one standard deviation (1-σ, 68%, dark gray) or two (2-σ, 95%, light gray) is indicated.

Discussion

Some of the highest *in situ* water microplastic measurements were found along the outer edge of the Po river plume, which suggests that either microplastic concentrations in the open Adriatic are at least comparable with those from the river, or that there are local accumulation processes occurring along the front between fresh river water and much higher salinity ocean water. Given that rivers are considered one of the main sources of plastic debris to the ocean (Jambeck et al., 2015; Lebreton et al., 2017) together with evidence that the Adriatic Sea is a highly dissipative system (Horvat, 2015), the latter hypothesis is more likely. Furthermore, the concentrations found in this study are an order of magnitude higher than values measured by Suaria et al. (2016) in the open Adriatic Sea. Using the median *in situ* measured microplastic concentration from this study together with average Po river discharge (1500 m³/s) and estimates of microplastic particle count to weight in the Adriatic (1.68 to 3 mg/particle; Suaria et al., 2016; van der Wal et al., 2015; Vianello et al., 2015), a rough estimate of floating microplastic released

by the Po River ranges between 1.7 and 3.1 tonnes per day. This translates to between 636 and 1,135 tonnes/yr, coming close to the estimates of 1,349 tonnes/yr by Liubartseva et al. (2016).

Very low *in situ* water microplastic concentrations were found for the Po di Maistra and delle Tolle mouths, as well as the Busa di Scirocco. Two of these river mouths, namely Maistra and Scirocco, were observed to also have low river plume influence from the remote sensing accumulation map. Maistra is expected to have the smallest outflow of all river mouths (Correggiari et al., 2005), and was thus also found to have the smallest impact from the ocean current accumulation modelling (Figure 5). The low *in situ* water microplastic concentration measurement from Po delle Tolle is less easily clarified, as this mouth was found to have a substantial influence by both the ocean current and remote sensing accumulation models. There was also a discrepancy between the measured *in situ* concentrations from the middle Tolle mouth and before the Tolle arm divides into three. This suggests that further accumulation processes may be occurring within the Tolle sub-arm which have not been captured by the model , and thus warrants further investigation than was feasible within this study.

The top three contributing polymer types from the sediment microplastic concentrations were PE, styrene and PP, in step with general trends observed in both the Po River (van der Wal et al., 2015) and the Mediterranean Sea (Suaria et al., 2016) as well as coastal (Zhang, 2017) and global oceans (Andrady, 2017). PE and PP make up between 45-50% of total global plastic production (PlasticsEurope, 2016). Higher occurrence of other plastic types, especially the heavier polymers such as EVOH, PVAL, PET (polyethylene terephthalate) and PVC (polyvinylchloride), were found at Caleri, Levante and Pila North 2 (Figure 2 and Table 2). Caleri in particular was found to have the most extreme microplastic concentration, exceeding the measurement by Munari et al. (2017) of 21.68 particles/DW kg at Volano , just south of the Po Delta. It is important to note that a possible explanation for this could be different sampling locations, as this study sampled the extreme high tide line in contrast to the most recent high tide line. Our measurements were lower than those made in the Venice Lagoon (672-2175 particles/DW kg; Vianello et al., 2013), although again it should be noted that smaller size classes were under investigation. It further has been suggested that the lagoon serves as neither a sink nor a source of anthropogenic litter (Carlson et al., 2017). The two northernmost beaches surveyed in this study (Caleri and Levante) were located close to either a public parking lot or a harbor. Heavier particles are known to be transported

more slowly than particles which are less dense than surrounding seawater (Cable et al., 2017), which include the plastic types EVOH, PVAL, PET and PVC in their virgin form. This suggests that the higher concentration rates more likely result from local sources, rather than longer distance transportation by the Po river plume or other Adriatic currents.

The ocean current modelling results suggest that surface currents play a more deciding role in determining beaching rates, with the number of particles being released by the river only semi-coupled to beach accumulation. Surface currents in the northern Adriatic is determined by wind regime and freshwater influx, the Po river being the main contributor (Falcieri et al., 2014). VMP tracks from different river mouths revealed beaching rates of up to 18% for all modelled river mouths, with the exception of the southernmost mouth of Po di Goro. This is a result of the Goro freshwater plume likely being held closer to shoreline by the other plumes, thus allowing plume water to interact with the coastline for a longer period of time. For the other river mouths, VMP beaching was found to occur within 10 days following release, and beaching rate estimates suggests that over 80% of the microplastic particles being released by the Po River are being dispersed to the open Adriatic system.

Coastal exposure modelling using SPM derived from remote sensing images was able to well capture the signal of sediment heavy river plume waters spreading along the coastline (Figure 10 and Figure 11). Plume exposure was found to be highest locally around the five main river mouths (Maistra, Pila, Tolle, Gnocca and Goro), as well as by side channels (Scirocco, Tramontana). Different amounts of river plume exposure were determined for the three arms of the Tolle river mouth, with the highest signal coming from the middle arm and the lowest from the southern arm. Evidence of an extra river mouth with strong outflow between Tramontana and Pila from the remote sensing analysis follows observations made while collecting the field data. The Po della Pila mouth is supposed to transport over 60% of the entire river discharge (Correggiari et al., 2005), but based on the SPM exposure map, this river mouth appears to be on par with the effects from the Po delle Tolle and Busa di Tramontana. A persistent sand bank was observed at the opening of this river mouth both in the remote sensing images and during sampling in the field. In images taken during high SPM events, it is clear that flow out of Po della Pila is being split into a northern and southern portion after encountering this sand bar. If flow is indeed being slowed out of Po della Pila by the presence of this sand bar, this would provide a mechanism for why flow is so high out of the Busa di

Tramontana and the unnamed outlet just south of Tramontana. Although this can only be definitively tested with *in situ* hydrodynamic measurements, the potential of using remote sensing SPM images for identifying fine-scale river mouth dynamic patterns is nevertheless well demonstrated here. The time series was able to capture multiple acquisitions of Bora wind events with low river discharge and one instance with high river discharge. In all events, the river plume is observed to stay closer to the Italian coastline with Bora wind, following results and model predictions made by Falcieri et al. (2014). This is in stark contrast to the situation observed with Scirocco plus high discharge, where the river plume can be observed to extend further east and north than for either of the Bora event images (Figure 10). River plume form during Mistral events appear to be more strongly controlled by river discharge than wind regime. The relationship between wind regime and freshwater outflow on northern Adriatic circulation patterns is complex, but remote sensing images of the river plume can certainly serve as a useful tool for testing hypotheses.

Validation of both accumulation models against all *in situ* measurements did not produce a significant relationship. This is likely due to additional microplastic processes (such as biofouling or flocculation) and sources, outside of the Po river water, which were not included in either model. Another factor to acknowledge is the assumption of beaching occurring after a particle passes within 250 m of the coastline, representing a massive simplification of nearshore currents that was necessary with the given modelling tools. A slightly significant correlation was found between the ocean current accumulation map and *in situ* samples from beaches which were only accessible by boat and not located next to a large harbor. An inverse relationship between amount of beach litter and distance to nearest parking lot has already been established in the Adriatic (Munari et al., 2017), suggesting that beach tourism poses a significant plastic litter source not included in the models. The Po Delta is a protected area, and while there exists much beach tourism, so do also laudable volunteer beach clean-up activities from NGOs (such as the WWF), the locations of which were necessarily avoided during field sampling as best as possible. The remote sensing river plume exposure model was not found to have a significant relationship with the *in situ* samples but was very useful in identifying which river mouths were significant outflow contributors during the simulation period. This information can be useful in the set-up of future ocean current models of the Po Delta. A number of factors not incorporated into either the ocean current or the remote sensing model may largely explain the missing correlation. Refuse

resulting from the major shipping corridors which cross the Adriatic are posited to account for 20% of all marine plastic litter introduced each year to the sea and the Po river for only 13.5% thereof (Liubartseva et al., 2016). Windage of particles was not accounted for in the ocean current model, which can provide drift speeds up to 25% larger than the current speed (Chubarenko et al., 2016). After particles become beached, wind transportation may move particles laterally or further inland (Munari et al., 2016). Microplastic particle aging within the marine environment was also not included, including processes of biofouling, further fragmentation, flocculation and aggregation, all which are recognized as important dynamic parameters influencing residence times and transportation pathways (Zhang, 2017). Seasonality was accounted for in the ocean current model through changing the amount of VMP released dependent upon Po river outflow, but the concentration of microplastic particles was held constant during the entire modelling period. It has been established that river mouth concentrations of microplastic particles can vary by up to three orders of magnitude at different times of the year (Lebreton et al., 2017) and that storm water runoff events can significantly increase river mouth microplastic load (Zhang, 2017). Beaching in this study's ocean current model follows simplifying assumptions made in other studies (Lebreton et al., 2012; Politikos et al., 2017), since the mechanisms controlling onshore-offshore transport of microplastic particles remain unclear (Critchell et al., 2015; Hardesty et al., 2017; Hinata et al., 2017; Moreira et al., 2016). Despite this, these mechanisms likely play a driving role in determining small-scale and temporal variation in sediment microplastic deposition rates (Carlson et al., 2017; Hinata et al., 2017; Schulz et al., 2017; Zhang, 2017). Artefacts may also be introduced to the correlation through the *in situ* sediment sampling scheme. In an effort to circumvent potential temporal variability, the extreme high tide line was chosen for the field sampling over the most recent high tide line. Nevertheless, we only considered one strand line, which was sampled on only one date and used pooling of subsamples to compensate for small-scale variability.

There remain many uncertainties still in our understanding of the transportation and accumulation mechanisms of microplastics (Hardesty et al., 2017) and with this study we offer some insight into these mechanisms. From the hydrodynamic modelling, we see that particles which do not beach within the first 10 days (over 80% of all VMP emitted by the Po river) are transported away from the coastline. The hydrodynamic model also offers a continual track of VMP transportation and could be used to study VMP distribution in the open sea. In order to do this, changes in microplastic characteristics

with time should be included into the Lagrangian model physics. The remote sensing model presents snapshots of surface river plume form at a finer spatial resolution over a larger area than possible with current ocean current models. River plume exposure during the modelling period could be well captured but this is difficult to translate to actual microplastic accumulation rates. Model assimilation of remote sensing data into ocean current simulation models has begun to gain traction in other oceanographic modelling areas (Miyazawa et al., 2013; Stroud et al., 2009; Zhang et al., 2014), with up to 40% improvements in model forecast root square error. Hardesty et al. (2017) have already suggested the great improvements possible to our understanding of microplastic transportation pathways through integrating simulation model and empirical observations.

Deeper understanding of microplastic sources, pathways and accumulation areas is intrinsic to our ability to mitigate introduction of this pollutant to limnic and marine systems as well as organize clean-up activities. International agreements are already in place forbidding deposition of litter into the Mediterranean marine environment (Mistri et al., 2017; Munari et al., 2016), yet despite these steps this enclosed sea continues to have particularly high concentrations of marine debris (Cozar et al., 2015; Suaria et al., 2016). Other modelling efforts within the Adriatic suggest that land-based sources of marine litter contribute the majority of marine litter entry into the sea each year (Munari et al., 2017). National borders are not a component of marine plastic debris transportation pathway mechanisms and finding middle ground in national agendas to support concerted legislation efforts are difficult. *In situ* microplastic sampling and sample processing is costly, thus modelling offers a methodology for upscaling point measurements to larger areas than could be feasibly sampled (Hardesty et al., 2017). The idea to use sediment transportation models to deepen our understanding of microplastic transportation in smaller enclosed waterways has been suggested by multiple authors (Zhang, 2017, and references therein). Freshwater systems, in particular rivers, have been slower to receive the same microplastic research attention as attributed to marine systems (Wagner et al., 2014). Evidence exists that even low-density populations can still create heavy consumer plastic pollution (Free et al., 2014), underlining the importance of being able to efficiently and correctly locate source locations so that appropriate remediation actions can be taken.

Conclusions and outlook

In this study, microplastic accumulation exposure over one and half years along the Adriatic coastline was modelled using two different approaches: via a Lagrangian particle tracking sub-model, fed by modeled ocean currents, and remote sensing of sediment heavy river plume waters. *In situ* sampling of both Po river and Adriatic Sea waters revealed microplastic concentrations up to 76 particles/m³, and beach sampling revealed concentrations up to 78.8 particles/DW kg. The ocean current approach was able to identify differing beaching rates between various river mouths and suggested that particle beaching mostly occurred within the first 10 days of release. Po river emitted particles that were moved offshore remained offshore, likely due to the continual freshwater input creating water density boundaries that inhibit westward transport. Especially the Po di Goro mouth was identified as effecting higher beaching rates over a much longer stretch of coastline. The sediment remote sensing approach was able to well represent river mouth relative strength, such as the relatively small contribution from the southernmost Po delle Tolle river arm or the much larger contribution of Busa di Tramontana in river outflow. Microplastic accumulation exposure maps were constructed from both approaches, which were found to be similar to one another but were not found to have a significant relationship to *in situ* beach sampling. This relationship changed when the beaches that were closer to public parking lots and harbors were removed, suggesting that microplastic sources which were not included in either modelling approach are also large contributors to beach microplastic accumulation.

Plastic debris has gained recognition as a severe problem at an international level, as demonstrated through United Nations reports (UNEP, 2016, 2015, 2014) and legislation regarding microplastics, such as the European Union Water Framework Directive (Directive 2000/60/EC) and the Marine Strategy Framework Directive (Directive 2008/56/EC). Marine litter, including plastic debris and microplastics, is directly addressed by the Mediterranean Action Plan (MAP) under the Barcelona Convention, with goals by the year 2020 to reduce top pollution sources by 80% and instate monitoring activities through the Horizon 2020 initiative. At the same time, consumption of plastic goods per capita continues to increase globally (Andrady, 2017), with North Americans and Western Europeans consuming up to 140 kg plastic goods in 2015, up 40% as compared to eight years earlier (Lebreton et al., 2012). Methods for identifying marine debris sources and forecasting accumulation areas have already been put forward as a method to reduce the cost and optimize the effort of remediation activities (Krelling

et al., 2017; UNEP, 2016). This study demonstrates the strengths and weaknesses of two separate modelling approaches, providing further tools aiming to answer the suggestion of Hardesty et al. (2017) to develop multipart solutions which can be applied at both local and regional scales to effect change.

Acknowledgements

References

Andersen, H.-E., McGaughey, R.J., Reutebuch, S.E., 2005. Estimating forest canopy fuel parameters using LIDAR data. Remote Sensing of Environment 94 (4), 441–449. 10.1016/j.rse.2004.10.013.

Andrady, A.L., 2017. The plastic in microplastics: A review. Marine Pollution Bulletin 119 (1), 12–22. 10.1016/j.marpolbul.2017.01.082.

Artegiani, A., Paschini, E., Russo, A., Bregant, D., Raicich, F., Pinardi, N., 1997a. The Adriatic Sea General Circulation. Part I: Air-Sea Interactions and Water Mass Structure. J. Phys. Oceanogr. 27 (8), 1492–1514. 10.1175/1520-0485(1997)027<1492:TASGCP>2.0.CO;2.

Artegiani, A., Paschini, E., Russo, A., Bregant, D., Raicich, F., Pinardi, N., 1997b. The Adriatic Sea General Circulation. Part II: Baroclinic Circulation Structure. J. Phys. Oceanogr. 27 (8), 1515–1532. 10.1175/1520-0485(1997)027<1515:TASGCP>2.0.CO;2.

Azzarello, M.Y., van Vleet, E.S., 1987. Marine birds and plastic pollution. Mar. Ecol. Prog. Ser. 37, 295–303. 10.3354/meps037295.

Besseling, E., Foekema, E.M., van Franeker, J.A., Leopold, M.F., Kühn, S., Bravo Rebolledo, E.L., Heße, E., Mielke, L., IJzer, J., Kamminga, P., Koelmans, A.A., 2015. Microplastic in a macro filter feeder: Humpback whale Megaptera novaeangliae. Marine Pollution Bulletin 95 (1), 248–252. 10.1016/j.marpolbul.2015.04.007.

Bignami, F., Sciarra, R., Carniel, S., Santoleri, R., 2007. Variability of Adriatic Sea coastal turbid waters from SeaWiFS imagery. J. Geophys. Res. 112 (C3). 10.1029/2006JC003518.

Bolaños, R., Sørensen, J.V.T., Benetazzo, A., Carniel, S., Sclavo, M., 2014. Modelling ocean currents in the northern Adriatic Sea. Continental Shelf Research 87, 54–72.

Boldrin, A., Carniel, S., Giani, M., Marini, M., Bernardi Aubry, F., Campanelli, A., Grilli, F., Russo, A., 2009. Effects of bora wind on physical and biogeochemical properties of stratified waters in the northern Adriatic. J. Geophys. Res. 114 (C8), 1492. 10.1029/2008JC004837.

Booij, N., Ris, R.C., Holthuijsen, L.H., 1999. A third-generation wave model for coastal regions: 1. Model description and validation. Journal of Geophysical Research: Oceans 104, 7649–7666.

Bouwman, H., Evans, S.W., Cole, N., Yive, Nee Sun Choong Kwet, Kylin, H., 2016. The flip-or-flop boutique: Marine debris on the shores of St Brandon's rock, an isolated tropical atoll in the Indian Ocean. Marine Environmental Research 114, 58–64.

Brovelli, M.A., Crespi, M., Fratarcangeli, F., Giannone, F., Realini, E., 2008. Accuracy assessment of high resolution satellite imagery orientation by leave-one-out method. ISPRS Journal of Photogrammetry and Remote Sensing 63 (4), 427–440. 10.1016/j.isprsjprs.2008.01.006.

Browne, M.A., Galloway, T.S., Thompson, R.C., 2010. Spatial patterns of plastic debris along Estuarine shorelines. Environmental science & technology 44 (9), 3404–3409. 10.1021/es903784e.

Brunner, K., Kukulka, T., Proskurowski, G., Law, K.L., 2015. Passive buoyant tracers in the ocean surface boundary layer: 2. Observations and simulations of microplastic marine debris. J. Geophys. Res. Oceans 120 (11), 7559–7573. 10.1002/2015JC010840.

Cable, R.N., Beletsky, D., Beletsky, R., Wigginton, K., Locke, B.W., Duhaime, M.B., 2017. Distribution and Modeled Transport of Plastic Pollution in the Great Lakes, the World's Largest Freshwater Resource. Front. Environ. Sci. 5, 10377. 10.3389/fenvs.2017.00045.

Campbell, J.W., O'Reilly, J.E., 2006. Metrics for quantifying the uncertainty in a chlorophyll Algorithm: Explicit equations and examples using the OC4.v4 algorithm and NOMAD data, 15 pp.

Carlson, D.F., Suaria, G., Aliani, S., Fredj, E., Fortibuoni, T., Griffa, A., Russo, A., Melli, V., 2017. Combining Litter Observations with a Regional Ocean Model to Identify Sources and Sinks of Floating Debris in a Semi-enclosed Basin: The Adriatic Sea. Front. Mar. Sci. 4, 1–16. 10.3389/fmars.2017.00078.

Carniel, S., Benetazzo, A., Bonaldo, D., Falcieri, F.M., Miglietta, M.M., Ricchi, A., Sclavo, M., 2016. Scratching beneath the surface while coupling atmosphere, ocean and waves: Analysis of a dense water formation event. Ocean Modelling 101, 101–112. 10.1016/j.ocemod.2016.03.007.

Carpenter, E.J., Smith, K.L., 1972. Plastics on the Sargasso Sea Surface. Science 175 (4027), 1240–1241. 10.1126/science.175.4027.1240.

Chubarenko, I., Bagaev, A., Zobkov, M., Esiukova, E., 2016. On some physical and dynamical properties of microplastic particles in marine environment. Marine Pollution Bulletin 108 (1-2), 105–112. 10.1016/j.marpolbul.2016.04.048.

Cole, M., Lindeque, P., Fileman, E., Halsband, C., Galloway, T.S., 2015. The impact of polystyrene microplastics on feeding, function and fecundity in the marine copepod Calanus helgolandicus. Environmental science & technology 49 (2), 1130–1137. 10.1021/es504525u.

Collard, F., Gilbert, B., Compère, P., Eppe, G., Das, K., Jauniaux, T., Parmentier, E., 2017. Microplastics in livers of European anchovies (Engraulis encrasicolus, L.). Environmental pollution (Barking, Essex : 1987). 10.1016/j.envpol.2017.07.089.

Colton, J.B., Burns, B.R., Knapp, F.D., 1974. Plastic particles in surface waters of the northwestern atlantic. Science 185 (4150), 491–497. 10.1126/science.185.4150.491.

Correggiari, A., Cattaneo, A., Trincardi, F., 2005. The modern Po Delta system: Lobe switching and asymmetric prodelta growth. Marine Geology 222-223, 49–74. 10.1016/j.margeo.2005.06.039.

Cozar, A., Sanz-Martín, M., Martí, E., Ignacio González-Gordillo, J., Ubeda, B., Gálvez, J.Á., Irigoien, X., Duarte, C.M., 2015. Plastic Accumulation in the Mediterranean Sea. Concentrations of floating plastic debris in the Mediterranean Sea measured during MedSeA-2013 cruise. PloS one 10 (4), e0121762. 10.1594/PANGAEA.842054.

Cózar, A., Echevarría, F., González-Gordillo, J.I., Irigoien, X., Ubeda, B., Hernández-León, S., Palma, A.T., Navarro, S., García-de-Lomas, J., Ruiz, A., Fernández-de-Puelles, M.L., Duarte, C.M., 2014. Plastic debris in the open ocean. Proceedings of the National Academy of Sciences of the United States of America 111 (28), 10239–10244. 10.1073/pnas.1314705111.

Cozzi, S., Giani, M., 2011. River water and nutrient discharges in the Northern Adriatic Sea: Current importance and long term changes. Continental Shelf Research 31 (18), 1881–1893. 10.1016/j.csr.2011.08.010.

Critchell, K., Grech, A., Schlaefer, J., Andutta, F.P., Lambrechts, J., Wolanski, E., Hamann, M., 2015. Modelling the fate of marine debris along a complex shoreline: Lessons from the Great Barrier Reef. Estuarine, Coastal and Shelf Science 167, 414–426. 10.1016/j.ecss.2015.10.018.

Dekker, A.G., 1993. Detection of optical water quality parameters for eutrophic waters by high resolution remote sensing. Proefschrift Vrije Universiteit Amsterdam, Amsterdam, The Netherlands, 237 pp.

Derraik, J.G.B., 2002. The pollution of the marine environment by plastic debris: A review. Marine Pollution Bulletin 44, 842–852.

Desforges, J.-P.W., Galbraith, M., Ross, P.S., 2015. Ingestion of microplastics by zooplankton in the Northeast Pacific Ocean. Archives of environmental contamination and toxicology 69 (3), 320–330. 10.1007/s00244-015-0172-5.

Devriese, L.I., van der Meulen, M.D., Maes, T., Bekaert, K., Paul-Pont, I., Frère, L., Robbens, J., Vethaak, A.D., 2015. Microplastic contamination in brown shrimp (Crangon crangon, Linnaeus 1758) from coastal waters of the Southern North Sea and Channel area. Marine Pollution Bulletin 98 (1-2), 179–187. 10.1016/j.marpolbul.2015.06.051.

Doxaran, D., Froidefond, J.-M., Lavender, S., Castaing, P., 2002. Spectral signature of highly turbid waters: Application with SPOT data to quantify suspended particulatematter concentrations. Remote Sensing of Environment 81, 149–161.

Dris, R., Imhof, H., Sanchez, W., Gasperi, J., Galgani, F., Tassin, B., Laforsch, C., 2015. Beyond the ocean: Contamination of freshwater ecosystems with (micro-)plastic particles. Environ. Chem. 12 (5), 539. 10.1071/EN14172.

Duhec, A.V., Jeanne, R.F., Maximenko, N., Hafner, J., 2015. Composition and potential origin of marine debris stranded in the Western Indian Ocean on remote Alphonse Island, Seychelles. Marine Pollution Bulletin 96 (1-2), 76–86. 10.1016/j.marpolbul.2015.05.042.

Eriksen, M., Lebreton, L.C.M., Carson, H.S., Thiel, M., Moore, C.J., Borerro, J.C., Galgani, F., Ryan, P.G., Reisser, J., 2014. Plastic pollution in the world's oceans: More than 5 trillion plastic pieces weighing over 250,000 tons afloat at sea. PloS one 9 (12), e111913. 10.1371/journal.pone.0111913.

Eriksson, C., Burton, H., 2003. Origins and Biological Accumulation of Small Plastic Particles in Fur Seals from Macquarie Island. Ambio 32 (6), 380. 10.1639/0044-7447(2003)032[0380:OABAOS]2.0.CO;2.

Falcieri, F.M., Benetazzo, A., Sclavo, M., Russo, A., Carniel, S., 2014. Po River plume pattern variability investigated from model data. Continental Shelf Research 87, 84–95. 10.1016/j.csr.2013.11.001.

Fargion, G.S., Mueller, J.L., 2000. Ocean Optics Protocols for Satellite Ocean Color Sensor Validation, Revision 2: Sensor Intercomparison and Merger for Biological and Interdisciplinary Ocean Studies (SIMBIOS) Project Technical Memoranda. NASA/TM-2000-209966/REV2, Rept-2000-04041-0/REV2, NAS 1.15:209966/REV2. NASA, NASA Goddard Space Flight Center, Greenbelt, MD, USA, 194 pp. https://ntrs.nasa.gov/search.jsp?R=20000097063.

Fazey, F.M., Ryan, P.G., 2016. Biofouling on buoyant marine plastics: An experimental study into the effect of size on surface longevity. Environmental Pollution 210, 354–360.

Free, C.M., Jensen, O.P., Mason, S.A., Eriksen, M., Williamson, N.J., Boldgiv, B., 2014. High-levels of microplastic pollution in a large, remote, mountain lake. Marine Pollution Bulletin 85 (1), 156–163. 10.1016/j.marpolbul.2014.06.001.

G7 Germany, 2015. Leaders' Declaration G7 Summit, 7-8 June 2015. G7 Germany, Schloss Elmau, Germany, 23 pp.

Galgani, F., Hanke, G., Werner, S., Oosterbaan, L., Nilsson, P., Fleet, D., Kinsey, S., Thompson, R.C., van Franeker, J., Vlachogianni, T., Scoullos, M., Veiga, J.M., Palatinus, A., Matiddi, M., Maes, T., Korpinen, S., Budziak, A., Leslie, H., Gago, J.,

Liebezeit, G., 2013. Guidance on monitoring of marine litter in European seas: A guidance document within the Common Implementation Strategy for the Marine Strategy Framework Directive. Publications Office of the European Union, Luxembourg, 1 online resource (124.

Galgani, F., Pham, C.K., Reisser, J., 2017. Editorial: Plastic Pollution. Front. Mar. Sci. 4, e1600582. 10.3389/fmars.2017.00307.

GESAMP, 2016. Sources, fate and effects of microplastics in the marine environment: part two of a global assessment. Rep. Stud. GESAMP 93. IMO, FAO, UNESCO-IOC, UNIDO, WMO, IAEA, UN, UNEP, UNDP Joint Group of Experts on the Scientific Aspects of Marine Environmental Protection, Rome, Italy, 221 pp.

Haidvogel, D.B., Arango, H., Budgell, W.P., Cornuelle, B.D., Curchitser, E., Di Lorenzo, E., Fennel, K., Geyer, W.R., Hermann, A.J., Lanerolle, L., Levin, J., McWilliams, J.C., Miller, A.J., Moore, A.M., Powell, T.M., Shchepetkin, A.F., Sherwood, C.R., Signell, R.P., Warner, J.C., Wilkin, J., 2008. Ocean forecasting in terrain-following coordinates: formulation and skill assessment of the Regional Ocean Modeling System. Journal of Computational Physics 227, 3595–3624.

Hardesty, B.D., Harari, J., Isobe, A., Lebreton, L., Maximenko, N., Potemra, J., van Sebille, E., Vethaak, A.D., Wilcox, C., 2017. Using Numerical Model Simulations to Improve the Understanding of Micro-plastic Distribution and Pathways in the Marine Environment. Front. Mar. Sci. 4, 30. 10.3389/fmars.2017.00030.

Heim, B., 2005. Qualitative and Quantitative Analyses of Lake Baikal's Surface-Waters Using Ocean Colour Satellite Data (SeaWiFS). doctoral, 142 pp.

Hermabessiere, L., Dehaut, A., Paul-Pont, I., Lacroix, C., Jezequel, R., Soudant, P., Duflos, G., 2017. Occurrence and effects of plastic additives on marine environments and organisms: A review. CHEMOSPHERE. 10.1016/j.chemosphere.2017.05.096.

Hinata, H., Mori, K., Ohno, K., Miyao, Y., Kataoka, T., 2017. An estimation of the average residence times and onshore-offshore diffusivities of beached microplastics based on the population decay of tagged meso- and macrolitter. Marine Pollution Bulletin 122 (1-2), 17–26. 10.1016/j.marpolbul.2017.05.012.

Hoffman, M.J., Hittinger, E., 2017. Inventory and transport of plastic debris in the Laurentian Great Lakes. Marine Pollution Bulletin 115 (1-2), 273–281. 10.1016/j.marpolbul.2016.11.061.

Horvat, P. (Ed.), 2015. MICRO 2015: Seminar on Microplastics Issues, 54 pp.

Imhof, H.K., Ivleva, N.P., Schmid, J., Niessner, R., Laforsch, C., 2013. Contamination of beach sediments of a subalpine lake with microplastic particles. Current biology : CB 23 (19), 8. 10.1016/j.cub.2013.09.001.

IOC, SCOR, 1994. Protocols for the Joint Global Ocean Flux Study (JGOFS) core measurements. IOC Manuals and Guides No. 29, 181 pp.

Jambeck, J.R., Geyer, R., Wilcox, C., Siegler, T.R., Perryman, M., Andrady, A., Narayan, R., Law, K.L., 2015. Plastic waste inputs from land into the ocean. Science (New York, N.Y.) 347 (6223), 768–771. 10.1126/science.1260352.

Jørgensen, P.V., 1999. Standard CZCS Case 1 algorithms in Danish coastal waters. International Journal of Remote Sensing 20 (7), 1289–1301. 10.1080/014311699212731.

Karami, A., Golieskardi, A., Choo, C.K., Larat, V., Karbalaei, S., Salamatinia, B., 2017a. Microplastic and mesoplastic contamination in canned sardines and sprats. The Science of the total environment 612, 1380–1386. 10.1016/j.scitotenv.2017.09.005.

Karami, A., Golieskardi, A., Keong Choo, C., Larat, V., Galloway, T.S., Salamatinia, B., 2017b. The presence of microplastics in commercial salts from different countries. Scientific reports 7, 46173. 10.1038/srep46173.

106

Kooi, M., Reisser, J., Slat, B., Ferrari, F.F., Schmid, M.S., Cunsolo, S., Brambini, R., Noble, K., Sirks, L.-A., Linders, T.E.W., Schoeneich-Argent, R.I., Koelmans, A.A., 2016. The effect of particle properties on the depth profile of buoyant plastics in the ocean. Scientific reports 6. 10.1038/srep33882.

Krelling, A.P., Souza, M.M., Williams, A.T., Turra, A., 2017. Transboundary movement of marine litter in an estuarine gradient: Evaluating sources and sinks using hydrodynamic modelling and ground truthing estimates. Marine Pollution Bulletin 119 (1), 48–63. 10.1016/j.marpolbul.2017.03.034.

Law, K.L., Morét-Ferguson, S.E., Goodwin, D.S., Zettler, E.R., Deforce, E., Kukulka, T., Proskurowski, G., 2014. Distribution of surface plastic debris in the eastern Pacific Ocean from an 11-year data set. Environmental science & technology 48 (9), 4732–4738. 10.1021/es4053076.

Law, K.L., Thompson, R.C., 2014. Oceans. Microplastics in the seas. Science (New York, N.Y.) 345 (6193), 144–145. 10.1126/science.1254065.

Lebreton, L.C.M., van der Zwet, J., Damsteeg, J.-W., Slat, B., Andrady, A., Reisser, J., 2017. River plastic emissions to the world's oceans. Nature communications 8, 15611. 10.1038/ncomms15611.

Lebreton, L.C.-M., Greer, S.D., Borrero, J.C., 2012. Numerical modelling of floating debris in the world's oceans. Marine Pollution Bulletin 64 (3), 653–661. 10.1016/j.marpolbul.2011.10.027.

Lett, C., Verley, P., Mullon, C., Parada, C., Brochier, T., Pierrick, P., Balnke, B., 2008. A lagrangian tool for modelling ichthyoplankton dynamics. Environmental Modelling and Software 23, 1210–1214.

Lindell, T., Pierson, D., Premazzi, G., Zilioli, E. (Eds.), 1999. Manual for monitoring European lakes using remote sensing techniques. Off. for Off. Publ. of the Europ. Communities, Luxembourg, 161 pp.

Liubartseva, S., Coppini, G., Lecci, R., Creti, S., 2016. Regional approach to modeling the transport of floating plastic debris in the Adriatic Sea. Marine Pollution Bulletin 103 (1-2), 115–127. 10.1016/j.marpolbul.2015.12.031.

Löder, M.G.J., Gerdts, G., 2015. Methodology Used for the Detection and Identification of Microplastics—A Critical Appraisal, in: Bergmann, M., Gutow, L., Klages, M. (Eds.), Marine Anthropogenic Litter. Springer International Publishing, Cham, pp. 201–227.

Löder, M.G.J., Imhof, H.K., Ladehoff, M., Löschel, L.A., Lorenz, C., Mintenig, S., Piehl, S., Primpke, S., Schrank, I., Laforsch, C., Gerdts, G., 2017. Enzymatic Purification of Microplastics in Environmental Samples. Environmental science & technology 51 (24), 14283–14292. 10.1021/acs.est.7b03055.

Löder, M.G.J., Kuczera, M., Mintenig, S., Lorenz, C., Gerdts, G., 2015. Focal plane array detector-based micro-Fourier-transform infrared imaging for the analysis of microplastics in environmental samples. Environ. Chem. 12 (5), 563. 10.1071/EN14205.

Mani, T., Hauk, A., Walter, U., Burkhardt-Holm, P., 2015. Microplastics profile along the Rhine River. Scientific reports 5, 17988. 10.1038/srep17988.

Mausra, J., Baker, J., Foster, G., Arthur, C., 2015. Laboratory methods for the analysis of microplastics in the marine environment: Recommendations for quantifying synthetic particles in waters and sediments Technical Memorandum NOS-OR&R-48. NOAA Marine Debris Program, NOAA Marine Debris Division, Silver Spring, MD, USA, 39 pp.

Michaelsen, J., 1987. Cross-validation in statistical climate forecast models. Journal of Climate and Applied Meteorology 26, 1589–1600.

Mistri, M., Infantini, V., Scoponi, M., Granata, T., Moruzzi, L., Massara, F., Donati, M. de, Munari, C., 2017. Small plastic debris in sediments from the Central Adriatic Sea: Types, occurrence and distribution. Marine Pollution Bulletin 124 (1), 435–440. 10.1016/j.marpolbul.2017.07.063.

Miyazawa, Y., Murakami, H., Miyama, T., Varlamov, S.M., Guo, X., Waseda, T., Sil, S., 2013. Data Assimilation of the High-Resolution Sea Surface Temperature Obtained from the Aqua-Terra Satellites (MODIS-SST) Using an Ensemble Kalman Filter. Remote Sensing 5 (6), 3123–3139. 10.3390/rs5063123.

Mobley, C.D., 1999. Estimation of the remote-sensing reflectance from above-surface measurements. Appl. Opt. 38 (36), 7442. 10.1364/AO.38.007442.

Moore, C.J., Lattin, G.L., Zellers, A.F., 2011. Quantity and type of plastic debris flowing from two urban rivers to coastal waters and beaches of Southern California. RGCI 11 (1), 65–73. 10.5894/rgci194.

Moreira, F.T., Prantoni, A.L., Martini, B., Abreu, M.A. de, Stoiev, S.B., Turra, A., 2016. Small-scale temporal and spatial variability in the abundance of plastic pellets on sandy beaches: Methodological considerations for estimating the input of microplastics. Marine Pollution Bulletin 102 (1), 114–121. 10.1016/j.marpolbul.2015.11.051.

Munari, C., Corbau, C., Simeoni, U., Mistri, M., 2016. Marine litter on Mediterranean shores: Analysis of composition, spatial distribution and sources in north-western Adriatic beaches. Waste management (New York, N.Y.) 49, 483–490. 10.1016/j.wasman.2015.12.010.

Munari, C., Scoponi, M., Mistri, M., 2017. Plastic debris in the Mediterranean Sea: Types, occurrence and distribution along Adriatic shorelines. Waste management (New York, N.Y.) 67, 385–391. 10.1016/j.wasman.2017.05.020.

Ogata, Y., Takada, H., Mizukawa, K., Hirai, H., Iwasa, S., Endo, S., Mato, Y., Saha, M., Okuda, K., Nakashima, A., Murakami, M., Zurcher, N., Booyatumanondo, R., Zakaria, M.P., Le Dung, Q., Gordon, M., Miguez, C., Suzuki, S., Moore, C., Karapanagioti, H.K., Weerts, S., McClurg, T., Burres, E., Smith, W., van Velkenburg, M., Lang, J.S., Lang, R.C., Laursen, D., Danner, B., Stewardson, N., Thompson, R.C., 2009. International Pellet Watch: global monitoring of persistent organic pollutants (POPs) in coastal waters. 1. Initial phase data on PCBs, DDTs, and HCHs. Marine Pollution Bulletin 58 (10), 1437–1446. 10.1016/j.marpolbul.2009.06.014.

Peduzzi, A., Wynne, R.H., Fox, T.R., Nelson, R.F., Thomas, V.A., 2012. Estimating leaf area index in intensively managed pine plantations using airborne laser scanner data. Forest Ecology and Management 270, 54–65. 10.1016/j.foreco.2011.12.048.

PlasticsEurope, 2014. Plastics – the Facts 2014. An analysis of European plastics production, demand and waste data. PlasticsEurope, 33 pp.

PlasticsEurope, 2016. Plastics – the Facts 2016. An analysis of European plastics production, demand and waste data. PlasticsEurope, 38 pp. http://www.plasticseurope.org/Document/plastics---the-facts-2016-15787.aspx?Page=DOCUMENT&FolID=2.

Politikos, D.V., Ioakeimidis, C., Papatheodorou, G., Tsiaras, K., 2017. Modeling the Fate and Distribution of Floating Litter Particles in the Aegean Sea (E. Mediterranean). Front. Mar. Sci. 4, 8. 10.3389/fmars.2017.00191.

Poulain, P.-M., 2001. Adriatic Sea surface circulation as derived from drifter data between 1990 and 1999. Journal of Marine Systems 29 (1-4), 3–32. 10.1016/S0924-7963(01)00007-0.

R Core Team, 2016. R: A language and environment for statistical computing. R Foundation for Statistical Computing, Vienna, Austria.

Rios, L.M., Moore, C., Jones, P.R., 2007. Persistent organic pollutants carried by synthetic polymers in the ocean environment. Marine Pollution Bulletin 54 (8), 1230–1237. 10.1016/j.marpolbul.2007.03.022.

Romeo, T., Pietro, B., Peda, C., Consoli, P., Andaloro, F., Fossi, M.C., 2015. First evidence of presence of plastic debris in stomach of large pelagic fish in the Mediterranean Sea. Marine Pollution Bulletin 95 (1), 358–361. 10.1016/j.marpolbul.2015.04.048.

Runge, C., 1895. Ueber die numerische Auflösung von Differentialgleichungen. Math. Ann. 46 (2), 167–178. 10.1007/BF01446807.

Schirinzi, G.F., Pérez-Pomeda, I., Sanchís, J., Rossini, C., Farré, M., Barceló, D., 2017. Cytotoxic effects of commonly used nanomaterials and microplastics on cerebral and epithelial human cells. Environmental research 159, 579–587. 10.1016/j.envres.2017.08.043.

Schmidt, L.K., Bochow, M., Imhof, K.H., Oswald, S., in review. Multi-temporal surveys for microplastic particles enabled by a novel and fast application of SWIR imaging spectroscopy – Study of an urban watercourse traversing the city of Berlin, Germany. Environmental Pollution.

Schulz, M., van Loon, W., Fleet, D.M., Baggelaar, P., van der Meulen, E., 2017. OSPAR standard method and software for statistical analysis of beach litter data. Marine Pollution Bulletin 122 (1-2), 166–175. 10.1016/j.marpolbul.2017.06.045.

Seltenrich, N., 2015. New link in the food chain? Marine plastic pollution and seafood safety. Environmental health perspectives 123 (2), A34-41. 10.1289/ehp.123-A34.

Sheavly, S.B., Register, K.M., 2007. Marine Debris & Plastics: Environmental Concerns, Sources, Impacts and Solutions. J Polym Environ 15 (4), 301–305. 10.1007/s10924-007-0074-3.

Simeoni, U., Corbau, C., 2009. A review of the Delta Po evolution (Italy) related to climatic changes and human impacts. Geomorphology 107 (1-2), 64–71. 10.1016/j.geomorph.2008.11.004.

Steppeler, J., Doms, G., Schattler, U., Bitzer, H.W., Gassmann, A., Damrath, U., Gregoric, G., 2003. Meso-gamma scale forecasts using the nonhydrostatic model LM. Meteorol. Atmos. Phys. 82, 75–96.

Stroud, J.R., Lesht, B.M., Schwab, D.J., Beletsky, D., Stein, M.L., 2009. Assimilation of satellite images into a sediment transport model of Lake Michigan. Water Resour. Res. 45 (2), 202. 10.1029/2007WR006747.

Suaria, G., Avio, C.G., Mineo, A., Lattin, G.L., Magaldi, M.G., Belmonte, G., Moore, C.J., Regoli, F., Aliani, S., 2016. The Mediterranean Plastic Soup: synthetic polymers in Mediterranean surface waters. Scientific reports 6. 10.1038/srep37551.

Thompson, R.C., Swan, S.H., Moore, C.J., Vom Saal, F.S., 2009. Our plastic age. Philosophical transactions of the Royal Society of London. Series B, Biological sciences 364 (1526), 1973–1976. 10.1098/rstb.2009.0054.

Turra, A., Manzano, A.B., Dias, R.J.S., Mahiques, M.M., Barbosa, L., Balthazar-Silva, D., Moreira, F.T., 2014. Three-dimensional distribution of plastic pellets in sandy beaches: Shifting paradigms. Scientific reports 4, 4435. 10.1038/srep04435.

UNEP, 2014. Valuing plastic: The business case for measuring, managing and disclosing plastic use in the consumer goods industry. UNEP, Nairobi, Kenya, 115 pp.

UNEP, 2015. Programme Performance Report, 2014-2015. UNEP, 52 pp.

UNEP, 2016. Marine plastic debris and microplastics – Global lessons and research to inspire action and guide policy change. United Nations Environment Programme, Nairobi, Kenya, 274 pp.

UNESCO, 1994. Protocols for the Joint Global Ocean Flux Study (JGOFS) core measurements. UNESCO Publ. No 29. IOC Manuals and Guides, Paris, France. http://unesdoc.unesco.org/images/0009/000997/099739eo.pdf.

van Cauwenberghe, L., Janssen, C.R., 2014. Microplastics in bivalves cultured for human consumption. Environmental pollution (Barking, Essex: 1987) 193, 65–70. 10.1016/j.envpol.2014.06.010.

van der Wal, M., van der Meulen, M., Tweehuijsen, G., Peterlin, M., Palatinus, A., Viršek, M.K., Coscia, L., Kržan, A., 2015. SFRA0025: Identification and Assessment of Riverine Input of (Marine) Litter. Eunomia Research & Consulting, 208 pp.

van Sebille, E., Wilcox, C., Lebreton, L., Maximenko, N., Hardesty, B.D., van Franeker, J.A., Eriksen, M., Siegel, D., Galgani, F., Law, K.L., 2015. A global inventory of small floating plastic debris. Environ. Res. Lett. 10 (12), 124006. 10.1088/1748-9326/10/12/124006.

Vanhellemont, Q., Ruddick, K., 2014. Turbid wakes associated with offshore wind turbines observed with Landsat 8. Remote Sensing of Environment 145, 105–115. 10.1016/j.rse.2014.01.009.

Vanhellemont, Q., Ruddick, K., 2015. Advantages of high quality SWIR bands for ocean colour processing: Examples from Landsat-8. Remote Sensing of Environment 161, 89–106. 10.1016/j.rse.2015.02.007.

Vianello, A., Acri, F., Aubry, F.B., Boldrin, A., Camatti, E., Da Rosa, L., Marceta, T., Moschino, V., 2015. Occurrence and distribution of floating microplastics in the North Adriatic Sea: Preliminary results, in: MICRO 2015 seminar. MICRO 2015, Piran, Slovenia. May 2015.

Vianello, A., Boldrin, A., Guerriero, P., Moschino, V., Rella, R., Sturaro, A., Da Ros, L., 2013. Microplastic particles in sediments of Lagoon of Venice, Italy: First observations on occurrence, spatial patterns and identification. Estuarine, Coastal and Shelf Science 130, 54–61. 10.1016/j.ecss.2013.03.022.

Wagner, M., Scherer, C., Alvarez-Muñoz, D., Brennholt, N., Bourrain, X., Buchinger, S., Fries, E., Grosbois, C., Klasmeier, J., Marti, T., Rodriguez-Mozaz, S., Urbatzka, R., Vethaak, A.D., Winther-Nielsen, M., Reifferscheid, G., 2014. Microplastics in freshwater ecosystems: What we know and what we need to know. Environmental sciences Europe 26 (1), 12. 10.1186/s12302-014-0012-7.

Warner, J.C., Armstrong, B., He, R., Zambon, J.B., 2010. Development of a coupled ocean–atmosphere–wave–sediment transport (COAWST) modeling system. Ocean Modelling 35, 230–244.

Warner, J.C., Sherwood, C.R., Signell, R.P., Harris, C.K., Arango, H.G., 2008. Development of a three-dimensional, regionl coupled wave, current, and sediment-transport model. Computers & Geosciences 34, 1284–1306.

Zbyszewski, M., Corcoran, P.L., 2011. Distribution and Degradation of Fresh Water Plastic Particles Along the Beaches of Lake Huron, Canada. Water Air Soil Pollut 220 (1-4), 365–372. 10.1007/s11270-011-0760-6.

Zhang, H., 2017. Transport of microplastics in coastal seas. Estuarine, Coastal and Shelf Science 199, 74–86. 10.1016/j.ecss.2017.09.032.

Zhang, K., Gong, W., Lv, J., Xiong, X., Wu, C., 2015. Accumulation of floating microplastics behind the Three Gorges Dam. Environmental pollution (Barking, Essex: 1987) 204, 117–123. 10.1016/j.envpol.2015.04.023.

Zhang, P., Wai, O., Chen, X., Lu, J., Tian, L., 2014. Improving Sediment Transport Prediction by Assimilating Satellite Images in a Tidal Bay Model of Hong Kong. Water 6 (3), 642–660. 10.3390/w6030642.

Zhang, W., Zhang, S., Wang, J., Wang, Y., Mu, J., Wang, P., Lin, X., Ma, D., 2017. Microplastic pollution in the surface waters of the Bohai Sea, China. Environmental pollution (Barking, Essex: 1987) 231 (Pt 1), 541–548. 10.1016/j.envpol.2017.08.058.

General discussion

This thesis demonstrates how remote sensing systems can serve as a tool to provide monitoring information over large areas. Chapters 1 and 2 concentrate on peatland fires in Southeast Asia, while chapter 3 focuses on turning boat-based measurements of a river plume into a coastal microplastic accumulation map. The research fields of fire occurrence and aquatic plastic pollution are largely unrelated, but both are challenged with similar issues in being able to effectively monitor large areas which range from thousands up to millions of square kilometers. Both active burning fires and water pollution dispersal present dynamic systems that inherently change rapidly over a short time periods. This is what in part makes collection of representative *in situ* ground points often untenable, since it is difficult to collect sufficient samples within a period of time small enough relative to the rate of change of the process being studied.

For large fire events in Indonesia, collection of more ground measurements is difficult due to little to no infrastructure in much of this massive country. Together, the islands of Java and Sumatra hold a little over ¾ of the nation's population (261 million), while representing only circa 30 % of the nation's landmass. Most areas in Indonesia are not heavily populated, with development efforts in these rural places over the last decades being sporadic and at times misguided. The current government has shown concrete signs of support for sustainable development, such as the two-year Peat Prize competition aiming to develop a more accurate and faster way to map peatlands or the 2011 legislation placing a moratorium on new concession licenses, but enforcement remains an issue. Fire control managers are more likely to be concentrated in offices in Jakarta than spread regionally throughout the country. Ground measurements are additionally dangerous along a quick-moving active fire line. It is difficult for foreign researchers interested in making ground measurements to respond quickly to an active fire event due to the difficulties of expediently obtaining a research visa for the country. Ground measurements are few, usually located only with a specific region, and often carried out by different groups, thus resulting in not being coordinated with one another. Thermal remote sensing of fires dates back to the beginning of publicly available global satellite dataset, such as Landsat (available back to 1972) and MODIS (operational data available as of 2000). While both these datasets offer the unique benefit of long time series data, their sensor limitations in comparison to newer technologies are laid out in chapters 1 and 2.

Ground measurement of *in situ* microplastic concentrations in a river plume system are also limited. With a single four-person team, it is possible to take between six to eight measurement points within one day. Repeated sampling from one date to another showed sizeable variation in measurement microplastic concentrations at a particular location (see Figure 2 in chapter 3). The coastal river plume system is influenced by tidal fluctuation, changes in wind, wave activity, and shifts over the day in river outflow. We observed in the field how freshwater river plumes would change their position along the coastline by over 100 m within less than a half an hour, clearly demonstrating what is meant by a highly dynamic spatial-temporal system. This could in part be ameliorated through making concurrent measurements from multiple boats, but this would on the one hand multiply campaign costs and on the other hand introduce potential new error sources for measurement differences between the teams. Remote sensing will always only be able to provide a snapshot of this dynamic system but over a large area, thus being able to partially overcome the spatial if not the temporal aspects of the system. The ocean modelling on the other hand is better able to address both the spatial and the temporal aspects, its only downside being that the modelled currents are only so good as our understanding of the various forces (wind, tide, freshwater input, waves, bathymetry) shaping the hydrodynamics. Both these methods, remote sensing and ocean current modelling, present tools for upscaling *in situ* point measurements that would alone present much difficulty properly capturing the dynamic system of a coastal river plume.

Benefits and constraints for fire detection and biomass burning

MODIS continues to be regarded as the main workhorse for worldwide fire detection, which is partially understandable given its four times daily acquisitions of the globe (both day and night images by each Aqua and Terra platforms) and a dataset that stretches back to cover over 15 years. Chapter 1 is not the first study to demonstrate the benefits of more sensitive satellite sensor systems to detect active fire events, but the new sensor aboard the TET-1 satellite, providing an improvement in circa double the amount of active fire detection, provides a strong argument against the continued use of MODIS for active fire detection over tropical Indonesia. The importance of the tropical peatlands contained within this country for the global climate are well explained in both chapters 1 and 2, thus it would be logical to use the most accurate and precise technology available to monitor this region. TET-1 was joined in 2016 by BIROS and data is available upon request from the German Remote Sensing Data Center. A multi-platform system reduces

time between acquisitions, which could help ameliorate the discrepancy to burned area estimates discussed in chapter 1. A future goal for the DLR FireBird mission should be increased availability of data on distribution platforms such as those used by the EOS, Landsat and Sentinel missions. Chapter 1 also makes clear the potential of TET-1 data for efficiently focusing firefighting activities on fires while they are still small, before they can form fire lines tens of kilometers long.

Chapter 2 demonstrates the use of an active sensing SAR system, Sentinel-1, to detect burned areas without the dependency of waiting for a smoke- and cloud-free acquisition. Fires are stopped in Indonesia by the onset of the rainy season, which is characterized by months of continual cloud cover over much of the country. Tropical vegetation, such as sedges and ferns, regrow quickly after fire events and can mask the VNIR burned area signal (Siegert et al., 2000; Siegert and Hoffmann, 2000), clearly exemplifying the benefits of utilizing a technology able to detect burned area in close to real-time. The established SAR methodology from chapter 2 will allow immediate response to the next large fire event and thus be able to provide much more accurate estimates of burned area to calculations of emissions impact for the global climate. SAR-based emissions estimates can in turn be utilized to check emissions estimates from atmospheric remote sensing methodologies.

Coastal accumulation of microplastic determined with different models

In chapter 3, a remote sensing methodology was used to determine exposure to microplastics ladened river plume water along a coastline in the northern Adriatic Sea. The resulting exposure map was found to be similar in pattern to an operative ocean current model, although some differences could be determined. The remote sensing model was most useful for determining river mouth flow dynamic patterns that were not included in the development of the ocean current model. The ocean current model was able to more fully capture the pathway of microplastic particles leaving the river mouth and then spreading into the Adriatic Sea, allowing for estimates of beaching rates, time till beaching, and numeric accumulation estimates along the coastline.

Comparison of both model results to *in situ* beach sediment measurements proved unsuccessful, but this likely does not solely stem from issues with the modelling assumptions. Background microplastic pollution from the Adriatic was not accounted for in either model. Plastic debris is most probably also being introduced from beach tourism as well as fishing and aquaculture activities within nearby lagoons. This debris degrades

into smaller and smaller pieces over time, and can be transported further through wind along the beach. Such processes were outside of the scope of either model. As microplastic is transported through an aquatic environment, processes such as biofouling and flocculation change particle characteristics, potentially causing particles to sink faster. These processes still contain many unanswered research questions and were thus also not accounted for in either model. Many of these processes cannot be accounted for in the purely remote sensing methodology presented here. In the discussion of chapter 3, model assimilation as a method to allow for incorporating the benefits of both systems into one was discussed. In this method, remote sensing images of water parameters are implemented to continually recalibrate the ocean model against reality. This method has been found to greatly improve ocean current model accuracy (Stroud et al., 2009; Zhang et al., 2014) and presents an attractive next step for microplastic modelling in front of the Po Delta.

Direction of future research

Within this thesis, I have demonstrated how remote sensing systems can be used as a tool to gain large scale coverage information of natural catastrophes resulting from anthropogenic activities over both land (section I) and water (section II). Chapter 1 shows how a cutting-edge fire detection system provides much improved fire area estimation and enhanced information on fire dynamics that previously possible. The SAR methodology laid out in chapter 2 indicates great improvement in close to real-time burned area detection. An often-cited critic of a SAR burned area methodology is that other processes (such as logging) can be responsible for changes in surface roughness. By combining the strengths of more accurate fire detection using the FireBird satellites together with the independence from cloud- and smoke-conditions offered by a SAR methodology, this critic can be addressed directly. A positively identified fire event supports the conclusion that SAR-sensed changes in surface roughness are due to burning processes. The FireBird mission currently flies two satellites, TET-1 and BIROS, and plans are being discussed between international space agencies to increase that number. The Sentinel-1 mission also currently contains two satellites and the development contract of the next two was signed December 2015. More sensor platforms result in further decrease in time between acquisitions, and thus offer a powerful system to provide essential information for development of a comprehensive fire monitoring system to address the recurrent issue of large fire disasters in Indonesia.

Section II of this thesis focused upon the issue of aquatic plastic debris as it leaves a river to enter the open ocean or become stranded along the coastline. A remote sensing model of coastline exposure to river-based microplastic provided similar information as an ocean current, Lagrangian tracking model of coastline accumulation. Weaknesses of both models were identified: the remote sensing model being unable to provide numeric accumulation rates and the ocean current model being based on river mouth dynamics that contradicted that which was observed in the remote sensing SPM images. Model assimilation, where remote sensing images are used to continually recalibrate ocean current modelling in the complex nearshore environment, presents a very attractive next step to overcome these identified weaknesses. An up to 40% improvement in modelling accuracy of the Po River plume in the North Adriatic would prove useful to many other research sectors outside of plastic debris monitoring, such as bottom sediment movement models, shipping navigation or marine species dispersal patterns.

These three chapters provide remote sensing tools to address large environmental issues resulting from anthropogenic activities. Mankind is facing a point in its history where we have become powerful enough to influence the global environment that we depend on for our survival. Exactly how our activities influence the environment are some of the strongest non-military political strife topics of modern times. One thing is for certain, millions of people, ranging from places such as South Pacific islands disappearing under a rising ocean or hurricane ravaged coastlines along North America or even in a German supermarket feeling unsure if it is still safe to enjoy a can of sardines, are being forced to realize that our globe is changing and question our role in creating this new reality. The tools presented in this thesis offer information to help better understand some of these environmental issues. How (for the optimists) or if (for the pessimists) mankind can use this information to improve our collective welfare remains an open question.

References

Andrady, A.L., 2017. The plastic in microplastics: A review. Marine Pollution Bulletin 119 (1), 12–22. 10.1016/j.marpolbul.2017.01.082.

Barber, C.V., Schweithelm, J., 2000. Trial by Fire: Forest Fires and Forestry Policy in Indonesia's Era of Crisis and Reform. World Resources Institute Forest Frontiers Initiative, Washington, DC, 76 pp.

Bjerknes, J., 1966. A possible response of the atmospheric Hadley circulation to equatorial anomalies of ocean temperature. Tellus 18 (4), 820–829. 10.1111/j.2153-3490.1966.tb00303.x.

Bjerknes, J., 1969. Atmospheric teleconnections from the equatorial Pacific. Monthly Weather Review 97 (3), 163-172.

Cashin, P., Mohaddes, K., Raissi, M., 2015. Fair Weather or Foul? The Macroeconomic Effects of El Niño. International Monetary Fund, Washington, D.C, 30 pp.

Church, J.A., White, N.J., 2011. Sea-level rise from the late 19th to the early 21st century. Surveys in Geophysics 32 (4-5), 585–602. 10.1007/s10712-011-9119-1.

Cole, M., Lindeque, P., Fileman, E., Halsband, C., Galloway, T.S., 2015. The impact of polystyrene microplastics on feeding, function and fecundity in the marine copepod Calanus helgolandicus. Environmental Science & Technology 49 (2), 1130–1137. 10.1021/es504525u.

Cózar, A., Echevarría, F., González-Gordillo, J.I., Irigoien, X., Ubeda, B., Hernández-León, S., Palma, A.T., Navarro, S., García-de-Lomas, J., Ruiz, A., Fernández-de-Puelles, M.L., Duarte, C.M., 2014. Plastic debris in the open ocean. Proceedings of the National Academy of Sciences of the United States of America 111 (28), 10239–10244. 10.1073/pnas.1314705111.

Derraik, J.G.B., 2002. The pollution of the marine environment by plastic debris: A review. Marine Pollution Bulletin 44, 842–852.

Di Mauro, R., Kupchik, M.J., Benfield, M.C., 2017. Abundant plankton-sized microplastic particles in shelf waters of the northern Gulf of Mexico. Environmental Pollution 230, 798–809. 10.1016/j.envpol.2017.07.030.

Donner, S.D., 2009. Coping with commitment: Projected thermal stress on coral reefs under different future scenarios. PLOS One 4 (6), e5712. 10.1371/journal.pone.0005712.

Donohue, M.J., Boland, R.C., Sramek, C.M., Antonelis, G.A., 2001. Derelict fishing gear in the Northwestern Hawaiian Islands: Diving surveys and debris removal in 1999 confirm threat to coral reef ecosystems. Marine Pollution Bulletin 42 (12), 1301–1312.

Eriksen, M., Lebreton, L.C.M., Carson, H.S., Thiel, M., Moore, C.J., Borerro, J.C., Galgani, F., Ryan, P.G., Reisser, J., 2014. Plastic Pollution in the World's Oceans: More than 5 Trillion Plastic Pieces Weighing over 250,000 Tons Afloat at Sea. PLOS One 9 (12), e111913. 10.1371/journal.pone.0111913.

FAO, 1997. Farmers brace for extreme weather conditions as El Niño effect hits Latin America and Australia. Food and Agriculture Organization of the United Nations. http://www.fao.org/News/1997/970904-e.htm. Accessed 13 February 2018.

FAO, 2013. FAO Statistical Yearbook 2013: World Food and Agriculture, 1 online resource (307 pages).

FAO, 2014. The State of World Fisheries and Aquaculture: Opportunities and Challenges. Food and Agriculture Organization of the United Nations, Rome, Italy, xv, 223.

G7 Germany, 2015. Leaders' Declaration G7 Summit, 7-8 June 2015. G7 Germany, Schloss Elmau, Germany, 23 pp.

Galgani, F., Hanke, G., Werner, S., Oosterbaan, L., Nilsson, P., Fleet, D., Kinsey, S., Thompson, R.C., van Franeker, J., Vlachogianni, T., Scoullos, M., Veiga, J.M., Palatinus, A., Matiddi, M., Maes, T., Korpinen, S., Budziak, A., Leslie, H., Gago, J., Liebezeit, G., 2013. Guidance on Monitoring of Marine Litter in European Seas. Publications Office of the European Union, Luxembourg, 1 online resource (124.

Galgani, F., Pham, C.K., Reisser, J., 2017. Editorial: Plastic Pollution. Frontiers in Marine Science 4, e1600582. 10.3389/fmars.2017.00307.

Gaveau, D.L.A., Salim, M.A., Hergoualc'h, K., Locatelli, B., Sloan, S., Wooster, M., Marlier, M.E., Molidena, E., Yaen, H., DeFries, R., Verchot, L., Murdiyarso, D., Nasi, R., Holmgren, P., Sheil, D., 2014. Major atmospheric emissions from peat fires in Southeast Asia during non-drought years: Evidence from the 2013 Sumatran fires. Scientific Reports 4, 6112. 10.1038/srep06112.

GESAMP, 2016. Sources, Fate and Effects of Microplastics in the Marine Environment: Part 2 of a Global Assessment. Rep. Stud. GESAMP 93. IMO, FAO, UNESCO-IOC, UNIDO, WMO, IAEA, UN, UNEP, UNDP Joint Group of Experts on the Scientific Aspects of Marine Environmental Protection, Rome, Italy, 221 pp.

Geyer, R., Jambeck, J.R., Law, K.L., 2017. Production, use, and fate of all plastics ever made. Science Advances 3 (7), e1700782. 10.1126/sciadv.1700782.

Goldstein, J., 2016. Carbon Bomb: Indonesia's Failed Mega Rice Project. Rachel Carson Center for Environment and Society. http://www.environmentandsociety.org/arcadia/carbon-bomb-indonesias-failed-mega-rice-project.

Halpert, M.S., Ropelewski, C.F., 1992. Surface temperature patterns associated with the Southern Oscillation. Journal of Climate 5, 577–593.

Hernandez, E., Nowack, B., Mitrano, D.M., 2017. Polyester textiles as a source of microplastics from households: A mechanistic study to understand microfiber release during washing. Environmental Science & Technology 51 (12), 7036–7046. 10.1021/acs.est.7b01750.

Huang, B., L'Heureux, M., Hu, Z.-Z., Zhang, H.-M., 2016. Ranking the strongest ENSO events while incorporating SST uncertainty. Geophysical Research Letters 43 (17), 9165–9172. 10.1002/2016GL070888.

Hulme, P.E., 2005. Adapting to climate change: Is there scope for ecological management in the face of a global threat? Journal of Applied Ecology 42 (5), 784–794. 10.1111/j.1365-2664.2005.01082.x.

IPCC, 2014. Climate Change 2014: Synthesis Report. Contribution of Working Groups I, II and III to the Fifth Assessment Report of the Intergovernmental Panel on Climate Change. IPCC, Geneva, Switzerland, 32 pp. http://www.ipcc.ch/report/ar5/syr/.

Jambeck, J.R., Geyer, R., Wilcox, C., Siegler, T.R., Perryman, M., Andrady, A., Narayan, R., Law, K.L., 2015. Plastic waste inputs from land into the ocean. Science 347 (6223), 768–771. 10.1126/science.1260352.

Karami, A., Golieskardi, A., Choo, C.K., Larat, V., Karbalaei, S., Salamatinia, B., 2018. Microplastic and mesoplastic contamination in canned sardines and sprats. Science of the Total Environment 612, 1380–1386. 10.1016/j.scitotenv.2017.09.005.

120

Kooi, M., Reisser, J., Slat, B., Ferrari, F.F., Schmid, M.S., Cunsolo, S., Brambini, R., Noble, K., Sirks, L.-A., Linders, T.E.W., Schoeneich-Argent, R.I., Koelmans, A.A., 2016. The effect of particle properties on the depth profile of buoyant plastics in the ocean. Scientific Reports 6, 33882. 10.1038/srep33882.

Lebreton, L.C.M., van der Zwet, J., Damsteeg, J.-W., Slat, B., Andrady, A., Reisser, J., 2017. River plastic emissions to the world's oceans. Nature Communications 8, 15611. 10.1038/ncomms15611.

Lebreton, L.C.-M., Greer, S.D., Borrero, J.C., 2012. Numerical modelling of floating debris in the world's oceans. Marine Pollution Bulletin 64 (3), 653–661. 10.1016/j.marpolbul.2011.10.027.

Lechner, A., Keckeis, H., Lumesberger-Loisl, F., Zens, B., Krusch, R., Tritthart, M., Glas, M., Schludermann, E., 2014. The Danube so colourful: A potpourri of plastic litter outnumbers fish larvae in Europe's second largest river. Environmental Pollution 188, 177–181. 10.1016/j.envpol.2014.02.006.

Mani, T., Hauk, A., Walter, U., Burkhardt-Holm, P., 2015. Microplastics profile along the Rhine River. Scientific Reports 5, 17988. 10.1038/srep17988.

Margono, B.A., Potapov, P.V., Turubanova, S., Stolle, F., Hansen, M.C., 2014. Primary forest cover loss in Indonesia over 2000–2012. Nature Climate Change 4 (8), 730–735. 10.1038/nclimate2277.

Marlier, M.E., DeFries, R.S., Kim, P.S., Koplitz, S.N., Jacob, D.J., Mickley, L.J., Myers, S.S., 2015. Fire emissions and regional air quality impacts from fires in oil palm, timber, and logging concessions in Indonesia. Environmental Research Letters 10 (8), 85005. 10.1088/1748-9326/10/8/085005.

Muraleedharan, T.R., Radojevic, M., Waugh, A., Caruana, A., 2000. Emissions from the combustion of peat: An experimental study. Atmospheric Environment 34 (18), 3033–3035. 10.1016/S1352-2310(99)00512-9.

Normile, D., 2016. El Niño's warmth devastating reefs worldwide. Science. 10.1126/science.aaf9845.

Page, S.E., Hooijer, A., 2016. In the line of fire: The peatlands of Southeast Asia. Philosophical Transactions of the Royal Society of London. Series B, Biological Sciences 371 (1696). 10.1098/rstb.2015.0176.

Pichel, W.G., Churnside, J.H., Veenstra, T.S., Foley, D.G., Friedman, K.S., Brainard, R.E., Nicoll, J.B., Zheng, Q., Clemente-Colón, P., 2007. Marine debris collects within the North Pacific Subtropical Convergence Zone. Marine Pollution Bulletin 54 (8), 1207–1211. 10.1016/j.marpolbul.2007.04.010.

PlasticsEurope, 2014. Plastics - the Facts 2014. An analysis of European plastics production, demand and waste data. PlasticsEurope, 33 pp.

PlasticsEurope, 2016. Plastics - the Facts 2016. An analysis of European plastics production, demand and waste data. PlasticsEurope, 38 pp. http://www.plasticseurope.org/Document/plastics---the-facts-2016-15787.aspx?Page=DOCUMENT&FolID=2.

Ropelewski, C.F., Halpert, M.S., 1987. Global and regional scale precipitation patterns associated with the El Niño/Southern Oscillation. Monthly Weather Review 115 (8), 1606–1626. 10.1175/1520-0493(1987)115<1606:GARSPP>2.0.CO;2.

Sheavly, S.B., Register, K.M., 2007. Marine debris & plastics: Environmental concerns, sources, impacts and solutions. Journal of Polymers and the Environment 15 (4), 301–305. 10.1007/s10924-007-0074-3.

Siegert, F., Hoffmann, A.A., 2000. The 1998 forest fires in East Kalimantan (Indonesia): A quantitative evaluation using high resolution, multitemporal ERS-2 SAR images and NOAA-AVHRR hotspot data. Remote Sensing of Environment 72, 64–77.

Siegert, F., Hoffmann, A.A., Kuntz, S., 2000. Comparison of ATSR and NOAA-AVHRR hotspot data acquired during an exceptional fire event in Kalimantan (Indonesia). European Space Agency (Special Publication) 479, 122–128.

Siegert, F., Ruecker, G., Hinrichs, A., Hoffmann, A.A., 2001. Increased damage from fires in logged forests during droughts caused by El Niño. Nature 414 (6862), 437–440. 10.1038/35106547.

Simorangkir, D., 2006. Fire use: Is it really the cheaper land preparation method for large-scale plantations? Mitigation and Adaptation Strategies for Global Change 12 (1), 147–164. 10.1007/s11027-006-9049-2.

Stroud, J.R., Lesht, B.M., Schwab, D.J., Beletsky, D., Stein, M.L., 2009. Assimilation of satellite images into a sediment transport model of Lake Michigan. Water Resources Research 45 (2), 202. 10.1029/2007WR006747.

Thompson, R.C., Swan, S.H., Moore, C.J., Vom Saal, F.S., 2009. Our plastic age. Philosophical Transactions of the Royal Society of London. Series B, Biological Sciences 364 (1526), 1973–1976. 10.1098/rstb.2009.0054.

Tomczak, M., Godfrey, J.S. (Eds.), 1994. Regional Oceanography: An Introduction. Elsevier Science, Burlington, 437 pp.

Trenberth, K.E., 2002. Evolution of El Niño–Southern Oscillation and global atmospheric surface temperatures. Journal of Geophysical Research 107 (D8), 2044. 10.1029/2000JD000298.

UNEP, 2014. Valuing Plastic: The Business Case for Measuring, Managing and Disclosing Plastic Use in the Consumer Goods Industry. UNEP, Nairobi, Kenya, 115 pp.

UNEP, 2016. Marine Plastic Debris and Microplastics: Global Lessons and Research to Inspire Action and Guide Policy Change. United Nations Environment Programme, Nairobi, Kenya, 274 pp.

van Sebille, E., Wilcox, C., Lebreton, L., Maximenko, N., Hardesty, B.D., van Franeker, J.A., Eriksen, M., Siegel, D., Galgani, F., Law, K.L., 2015. A global inventory of small floating plastic debris. Environmental Research Letters 10 (12), 124006. 10.1088/1748-9326/10/12/124006.

Walker, G.T., 1924. Correlation in seasonal variations of weather. IX. A further study of world weather. Memoirs of the Indian Meteorological Department (24), 275–332.

WHOI, 1986. 1982-1983 El Niño: The worst there ever was. Woods Hole Oceanographic Institution. http://www.whoi.edu/science/B/people/kamaral/1982-1983ElNino.html. Accessed 13 February 2018.

World Bank, 2015. Indonesia Economic Quarterly: Reforming Amid Uncertainty. World Bank Group. http://pubdocs.worldbank.org/en/844171450085661051/IEQ-DEC-2015-ENG.pdf.

WWF-Indonesia Sebangau Project, 2012. Rewetting of Tropical Peat Swamp Forest in Sebangau National Park, Central Kalimantan, Indonesia. Sebangau National Park Office, in partnership with WWF Indonesia and WWF Germany, 125 pp. https://s3.amazonaws.com/CCBA/Projects/Rewetting_of_Tropical_Peat_Swamp_Forest_in_Sebangan_National_Park/SNP+Peat+Rewettting+Project+-+CCB+PDD+-+V01.pdf.pdf.

Zhang, H., 2017. Transport of microplastics in coastal seas. Estuarine, Coastal and Shelf Science 199, 74–86. 10.1016/j.ecss.2017.09.032.

Zhang, P., Wai, O., Chen, X., Lu, J., Tian, L., 2014. Improving sediment transport prediction by assimilating satellite images in a tidal bay model of Hong Kong. Water 6 (12), 642–660. 10.3390/w6030642.

Zhang, Q., Guan, Y., Yang, H., 2008. ENSO amplitude change in observation and coupled models. Advances in Atmospheric Sciences 25 (3), 361–366. 10.1007/s00376-008-0361-5.

Curriculum Vitae

Name	Elizabeth Catherine Atwood (born 14th September 1982, in Palo Alto, CA, USA)
Current address	Bacherstraße 20, 81539 Munich, Germany
Nationality	American
Language skills	English (mother tongue), German (fluent), Spanish (basic), French (basic)

Higher education	
since 09/2014	Doctoral studies in the group of Prof Dr Florian Siegert, GeoBio Center, LMU Munich Faculty of Biology, Martinsried, Germany
	Thesis title: "Remote sensing data as a tool to monitor and mitigate natural catastrophes resulting from anthropogenic activities: Case studies over land and water"
09/2007 – 03/2010	Master's studies (M.Sc.) in the program "Quantitative Ecology & Resource Management" (QERM) at the University of Washington, Seattle, WA, USA
	Master's thesis title: "Mesoscale eddies and ichthyoplankton community composition and abundance in the Gulf of Alaska"
09/2000 – 06/2005	Bachelor's studies (double major) at the University of California, Santa Cruz, CA, USA
	Bachelor's degree in Mathematics (B.A. 2004): "Gödel's Incompleteness Theorem"
	Bachelor's degree in Marine Biology (B.Sc. Hons. 2005): "Variation in breeding display behavior and evidence of laterality in male harbor seals *Phoca vitulina*"
09/1998 – 06/2000	Buxton School, Williamstown, MA, USA
	High school diploma (2000)
09/1996 – 06/1998	Santa Cruz High School, CA, USA

Teaching	Remote sensing and GIS, LMU (summer semester)
	Statistics tutoring, UW (winter and spring quarter)

Work experience	
09/2014 – 09/2017	Employee, RSS Remote Sensing Solutions GmbH, Baierbrunn, Germany
12/2011 – 09/2014	Program coordinator, Amgen Scholars Programme, Munich Center for Neurosciences, LMU Munich, Germany

	Public relations coordinator, Graduate School for Systemic Neuroscience, LMU Munich, Germany
05/2010 – 11/2011	Assistant, Amgen Scholars Programme, Munich Center for Neurosciences, LMU Munich, Germany
01 – 04/2010	Statistics consultant, School of Fisheries and Aquatic Sciences, University of Washington, Seattle, USA
02 – 06/2007	Research internship, Zoologische Staatssammlung München, Germany
12/2005 – 12/2006	Research and technical station manager, Huinay Scientific Field Station, 10th Region, Chile
06/2003 – 10/2005	Research assistant and scientific diver, Partnership for Interdisciplinary Studies of Coastal Oceans, Long Marine Lab, Santa Cruz, CA, USA
01/2002 – 10/2005	Research internship, Pinniped Cognition and Sensory Systems Lab, Long Marine Lab, Santa Cruz, CA, USA
09 – 12/2005	Consumer analyst, FishWise, Santa Cruz, CA, USA
01 – 06/2003	Research assistant, Prof. Dan Doak Lab, University of California, Santa Cruz, CA, USA
06 – 09/1998	Research assistant, Santa Cruz Institute for Particle Physics, University of California, Santa Cruz, CA, USA

Expeditions

9/2016	Citarum field campaign (Sentinels4Marine plastic waste project), 3 weeks, Indonesia.
6/2016	Po delta field campaign (Sentinels4Marine plastic waste project), 3 weeks, Italy.
8/2015	2nd Elbe field campaign (Sentinels4Marine plastic waste project), 3 days, Germany.
7/2015	1st Elbe field campaign (Sentinels4Marine plastic waste project), 4 weeks, Germany.
9/2009	NOAA survey cruise Kodiak to Dutch Harbor, 2 weeks, Alaska, USA.
3/2006	"Huinay Fiordos 3": Central Patagonian Zone (Puerto Natales to Golfo de Penas), 3 weeks, Chile.

Grants and prizes

North Pacific Research Board Student Grant, 06/2008 – 03/2010

GeoBio Center, Ludwig-Maximilians-Universität München und Freunde der Zoologische Staatssammlung München, 03 – 06/2007

Bachelor's thesis "Variation in breeding display behavior and evidence of laterality in male harbor seals *Phoca vitulina*" awarded honors, 06/2005

Meyers Research Grant Fund, 01– 06/2005

Publications

S. Lohberger, M. Stängel, E.C. Atwood, F. Siegert. (2018). Spatial evaluation of Indonesia's 2015 fire-affected area and estimated carbon emissions using Sentinel-1. Global Change Biology 24(2): 644–654, doi: 10.1111/gcb.13841.

E.C. Atwood, S. Englhart, E. Lorenz, W. Halle, W. Wiedemann, F. Siegert (2016). Detection and characterization of low temperature peat fires during the 2015 fire catastrophe in Indonesia using a new high-sensitivity fire monitoring satellite sensor (FireBird). PLOS ONE 11(8): e0159410.

S. Insley, M.M. Holt, B. Southall, E. Atwood. (2011). Vocal recognition of individuals versus relative dominance rank among breeding male northern elephant seals (*Mirounga angustirostris*). Proceedings of Meetings on Acoustics, Acoustical Society of America 12, 3aABa4.

E. Atwood, J.T. Duffy-Anderson, J.K. Horne, C. Ladd. (2010). Influence of mesoscale eddies on ichthyoplankton assemblages in the Gulf of Alaska. Fisheries Oceanography 19(6): 493–507.

P. Willenz, V. Häussermann, G. Försterra, M. Schrödl, R. Melzer, E. Atwood, C. Jorda. (2007). Finding more pieces of the Chilean puzzle. Global Marine Environment 5: 26-29.

Presentations

E.C. Atwood, J. Franke, S. Piehl, M. Bochow, F. Siegert and C. Laforsch. Contamination of aquatic ecosystems with plastic debris: Global and local monitoring using remote sensing methods. Institute seminar, CNR-ISMAR, Venice, Italy, 7 April 2016.

E.C. Atwood, J. Franke, S. Englhart, S. Piehl, M. Bochow, H. K. Imhof, F. Siegert and C. Laforsch. Belastung aquatischer Ökosysteme mit Kunststoffmüll: Möglichkeiten eines globalen und lokalen Monitorings mittels Satelliten-gestützter Methoden. 8. RESA Workshop, Bonn, Germany, 15-16 March 2016.

E.C. Atwood, J. Franke, S. Englhart, S. Piehl, M. Bochow, H. Imhof, F. Siegert, C. Laforsch. Belastung aquatischer Ökosysteme mit Kunststoffmüll: Möglichkeiten eines globalen und lokalen Monitorings mittels Satelliten-gestützter Methoden. Nationales Forum für Fernerkundung und Copernicus 2015, Berlin, Germany, 3-5 November 2015.

E.C. Atwood, J. Franke, S. Englhart, S. Piehl, M. Bochow, H. K. Imhof, F. Siegert and C. Laforsch. Contamination of Aquatic Ecosystems with Plastic Debris: Global and Local Monitoring Using Remote Sensing Methods. Workshop des DLR Raumfahrtmanagements "Nutzung der Sentinels und nationalen Erdbeobachtungs-Missionen", Bonn, Germany, 21 January 2015.

E. Atwood, J.K. Horne, J.T. Duffy-Anderson, C. Ladd. Association of larval fish abundance with mesoscale eddies in the Gulf of Alaska. Climate Change Effects on

Fish and Fisheries: Forecasting Impacts, Assessing Ecosystem Responses, and Evaluating Management Strategies, Sendai, Japan, 26-29 April 2010.

E. Atwood, J.T. Duffy-Anderson, J.K. Horne, C. Ladd. Influence of Gulf of Alaska mesoscale eddies on shelf and slope ichthyoplankton assemblages. 2010 Ocean Sciences Meeting, Portland, Oregon USA, 22-26 February 2010.

E. Atwood, J.K. Horne, J.T. Duffy-Anderson, C. Ladd. Influence of mesoscale eddies on ichthyoplankton assemblages in the Gulf of Alaska. Alaska Marine Science Symposium, Anchorage, Alaska USA, 19-23 January 2009.

E. Atwood, C.R. Kastak, R. Schusterman. Breeding behavior and evidence of laterality in male harbor seals (*Phoca vitulina*). Animal Behaviour Society 42nd Annual Meeting, Snowbird, Utah USA, 6-10 August 2005.

E. Atwood. Dynamic hierarchical relationships in male elephant seals (*Mirounga angustirostris*). UCSC Undergraduate Research Poster Symposium, Santa Cruz, California USA, June 2004.

Complementary education

4th ESA Advanced Training on Ocean Remote Sensing, French Research Institute for Exploitation of the Sea (IFREMER), Brest, France, 7-11 September 2015.

Monitoring the Oceans from Space (online course), FutureLearn, October – December 2016.

Additional qualifications

GIS software	ArcGIS, QGIS, R
Remote sensing software	ERDAS, ENVI, SNAP, eCognition, R, ATCOR, Sen2Cor, ACOLITE
Programming languages	R (very proficient), python (specifically with arcpy, proficient), C (basic), Matlab (basic), Latex (basic)
Scientific SCUBA diver	AAUS certified (2003, since then over 300 working dives), NAUI recreational certifications: basic, advanced, nitrox, rescue, dive master (2000-2003)

Munich, November 2, 2018

………………………………………….

Elizabeth C. Atwood